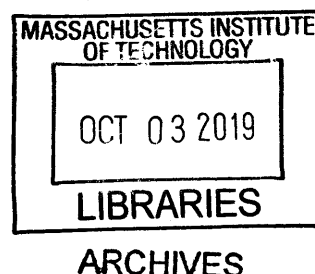


Structural investigations of class Ia ribonucleotide reductases by electron microscopy

by

Gyunghoon Kang

B.A. Chemistry and Chemical Biology
Cornell University, 2012



Submitted to the Department of Chemistry
in Partial Fulfillment of the Requirements for the Degree of

Doctor of Philosophy in Chemistry
at the
Massachusetts Institute of Technology

September 2019

© 2019 Massachusetts Institute of Technology. All rights reserved.

Signature redacted

Signature of Author _____

Department of Chemistry
August 6, 2019

Signature redacted

Certified by _____

Catherine L. Drennan
Professor of Biology and Chemistry
Howard Hughes Medical Institute Investigator and Professor
Thesis Supervisor

Signature redacted

Accepted by _____

Robert W. Field
Haslam and Dewey Professor of Chemistry
Chairman, Departmental Committee on Graduate Students

This doctoral thesis has been examined by a committee of the
Departments of Chemistry and Biology as follows:

Professor JoAnne Stubbe _____ **Signature redacted** _____

Thesis Committee Chair
Novartis Professor of Chemistry, Emeritus

Professor Catherine L. Drennan _____ **Signature redacted** _____

Thesis Supervisor
Professor of Biology and Chemistry
Howard Hughes Medical Institute Investigator and Professor

Professor Thomas U. Schwartz _____ **Signature redacted** _____

Thesis Committee Member
Boris Magasanik Professor of Biology

Structural investigations of class Ia ribonucleotide reductases
by electron microscopy

by
Gyunghoon Kang

Submitted to the Department of Chemistry on August 6th, 2019
in Partial Fulfillment of the Requirements
for the Degree of Doctor of Philosophy in Chemistry

ABSTRACT

Ribonucleotide reductase (RNR) catalyzes the reduction of nucleotides to their 2'-deoxynucleotide counterparts. The class Ia RNR from *Escherichia coli* is composed of two homodimeric subunits α_2 and β_2 that form an $\alpha_2\beta_2$ complex to perform nucleotide reduction. Chemistry is initiated by a thiyl-radical (C439•) in the active site of α_2 that is reversibly generated by a diferric-tyrosyl radical cofactor (Y122•) in β_2 by a series of proton-coupled electron transfer steps: $Y122\beta \leftrightarrow [W48\beta] \leftrightarrow Y356\beta \leftrightarrow Y731\alpha \leftrightarrow Y730\alpha \leftrightarrow C439\alpha$. A high-resolution structure of the active $\alpha_2\beta_2$ complex has long eluded the field due to the weak and transient nature of the α_2 - β_2 interaction. Previous studies revealed that perturbing radical transfer by incorporating unnatural amino acids along the transfer pathway, or by using mechanistic inhibitors that trap the radical in the active site, can extend the lifetime of the $\alpha_2\beta_2$ complex, allowing for structural studies. Here, we present our efforts to study the *E. coli* class Ia RNR $\alpha_2\beta_2$ complex, trapped using these different perturbation methods, using cryo-electron microscopy. The two $\alpha_2\beta_2$ structures presented here provide deeper insight into the structural dynamics of nucleotide reduction. We end with a brief discussion of class Ia RNR from T4 bacteriophage, which despite sharing high sequence identity to its host *E. coli* class Ia RNR, employs a very different mode of oligomeric regulation.

Thesis Supervisor: Catherine L. Drennan

Title: Professor of Biology and Chemistry

Howard Hughes Medical Institute Investigator and Professor

Acknowledgements

First and foremost, thank you Cathy, for helping me explore and grow as a scientist during my time in the lab. The environment you have created is truly special and it always helped to know that I had your support regardless of how well my science was going. Thanks to everyone in the Drennan lab, past and present, for being awesome. To Tsehai, Elizabeth, Marco, and Michael, thank you all for showing everyone that grad school can be about having fun in addition to working hard. Thanks, Yang-Ting, for always having the answers; I could always count on you. David, I'm not sure how you make everything look so easy, but it's inspirational, and also sometimes annoying. Dawson and Rohan, thanks for providing a space I could always go to for a laugh and a random Wikipedia fact. Thank you to my committee, Thomas and JoAnne for the feedback and support over the years. JoAnne, your energy and passion for science are truly inspiring and our discussions always challenge me and help me grow as a scientist.

Ed, you deserve a whole paragraph to yourself. Without the training, help, and guidance you provided, none of this work would have ever been possible. I can only aspire to pass on a fraction of what you've done for me. You are one of the most knowledgeable, patient people that I know and I cannot thank you enough for everything. From the long days at Brandeis to the data collection trips at Janelia, I always felt better knowing you were coming along. Your positivity and dedication to perfection are inspiring and I am lucky to call you my mentor.

Justin and Wade, thanks for letting me be your third wheel. Our nightly hangouts in 222 defined my first-year grad school experience and I wouldn't have had it any other way. Alex, you never fail to make me laugh. You're one of the most talented people that I know and I'm lucky to call you my friend. Wanky, Jenny, Kurt, and Mike, you all welcomed me into your friend group, and my grad school experience was that much richer because of it. Also, I can't believe how willing the four of you are to having multiple 9+ hour board gaming experiences. Thank you.

Angela. Oh, Angela. You didn't think when we moved in together as roommates that you'd be gaining a roommate for life, did you? I did. Just kidding, I didn't, but I am so grateful for how things have turned out. Thank you for being unconditionally supportive (except of my frequent desires to eat Indian buffet, but I guess you could justify that as also being supportive, of my health). Thank you for the happiness you bring into my life every day. Thank you for the thousands (tens of thousands?) of slices of pizza I can look forward to eating in our future. I couldn't have done this thing called grad school without you.

Finally, thank you to my family. Growing up surrounded by your endless love made me into the person I am today. Thank you. I love you.

Table of Contents

Chapter 1: Towards a structure of active RNR	15
A. Ribonucleotide reductases, a brief overview	16
B. <i>E. coli</i> class Ia RNR	17
C. Towards an active structure of <i>E. coli</i> class Ia RNR	18
D. Goals of this dissertation	21
E. References	23
F. Figures and Tables	27
Chapter 2: Cryo-EM structure of an active $\alpha_2\beta_2$ complex reveals conformational insight into PCET and enzymatic turnover	35
A. Summary	36
B. Introduction	37
C. Results	41
1. E52Q/F ₃ Y- β_2 and WT- α_2 with GDP and TTP produces complex that is stable enough for high-resolution structural analysis by cryo-EM	41
2. The $\alpha_2\beta_2$ complex is asymmetric	42
3. Previously structurally uncharacterized residues of the β subunit can be modeled	42
4. PCET pathway is structurally resolved	43
5. β E52 is positioned directly at the α - β interface	44
6. The two α monomers are structurally distinct	45
7. C-terminus of only one β monomer interacts with α_2 subunit in the $\alpha_2\beta_2$ complex	46
8. C-terminus of α' interacts with β'	46
D. Discussion	48
E. Materials and Methods	55
1. Protein preparation	55
2. Negative-stain grid preparation and data collection	55
3. 2D classification of negative-stain data	56
4. Cryo-EM grid optimization	56
5. Cryo-EM grid preparation used for data collection	56
6. Data collection of cryo-EM data	57
7. Frame alignment, defocus estimation, and micrograph assessment in SPHIRE	57
8. Particle selection	57
9. Frame alignment and defocus estimation in Relion 3.0	58
10. Map generation and refinement in Relion 3.0	58
11. Model building and refinement	58
F. References	60
G. Figures and Tables	66
Chapter 3: Cryo-EM structure of wildtype $\alpha_2\beta_2$ in the presence of mechanism-based inhibitor N₃UDP	93
A. Summary	94

B. Introduction	95
C. Results	97
1. Data processing using SPHIRE software suite.....	97
2. 3D classification and 3D variance analyses in SPHIRE	98
3. Data processing using Relion 3.0	99
4. Comparisons with E52Q/F ₃ Y- α 2 β 2.....	99
5. C-terminus of β is fully resolved.....	99
6. Both cone domains are ordered	100
7. C225/C462 of N ₃ UDP- α 2 β 2 α " are found in a unique conformation	101
8. C-terminus of α subunit	102
D. Discussion	103
E. Materials and Methods	107
1. Protein preparation	107
2. Grid preparation.....	107
3. Data collection	107
4. Initial frame alignment, defocus estimation, and micrograph assessment in SPHIRE	108
5. Particle selection and sub-selection	108
6. 3D map generation and post-processing in SPHIRE.....	108
7. Particle selection in Topaz.....	108
8. Frame alignment and defocus estimation in Relion 3.0.....	109
9. Map generation and refinement in Relion 3.0.....	109
10. Model building and refinement.....	109
F. Reference	110
G. Figures and Tables	113
Chapter 4: Class Ia RNR from T4 bacteriophage forms filaments composed of both α2 and β2	129
A. Summary	130
B. Introduction	131
C. Results	133
1. T4 class Ia RNR is less soluble than its <i>E. coli</i> counterpart.....	133
2. T4 enzyme forms helical filaments under "inactivating" conditions.....	133
3. Negative-stain reconstruction reveals helix composed of repeating α 2 β 2 units	133
4. Orientation between α 2 and β 2 in helical unit is rotated with respect to docking model	134
5. ATP in place of dATP does not affect filament quaternary structure	134
D. Discussion	136
E. Materials and Methods	138
1. Protein preparation	138
2. Grid preparation.....	138
3. Data imaging and collection.....	138
4. Particle selection and map generation.....	139
F. References	140
G. Figures and Tables	142

Chapter 5: Closing thoughts and future directions	151
A. Closing thoughts and future directions.....	152
B. References.....	156
Appendices	159
A. Strategies for optimizing cryo-EM samples	160
B. Negative-stain EM on human class Ia RNR with N₃CDP	166
C. Activity assays of <i>E. coli</i> class Ia RNR	171
Curriculum vitae	175

Chapter 1

Towards a structure of active RNR

1.A: Ribonucleotide Reductases, a brief overview

Ribonucleotide reductases (RNRs) are the only known enzymes in all organisms capable of reducing ribonucleotides to form their 2'-deoxyribonucleotide counterparts, a critical process in DNA biosynthesis and repair¹. Remarkably, RNRs reduce all four ribonucleotide substrates (U, C, A, G), with substrate specificity determined by cognate effectors binding to an allosteric site (dATP promotes reduction of U and C, dGTP promotes reduction A, TTP promotes reduction of G)^{2,3}. The chemistry of nucleotide reduction is initiated by a transient thiyl-radical that forms on a conserved cysteine residue in the active site⁴ (**Figure 1.1**).

There are three classes of RNR, divided based on the identity of the respective metallo-cofactors that are used to generate the transient active site thiyl-radical^{1,5} (**Figure 1.2**). Class II RNRs are oxygen-independent and utilize an adenosylcobalamin cofactor for radical generation^{6,7}. Class III RNRs require anaerobic conditions and utilize S-adenosylmethionine (SAM) and a Fe-S cluster to generate a stable glycy radical that in turn generates the active site thiyl-radical⁸. Class Ia RNRs, the focus of this dissertation, require molecular oxygen to generate a radical cofactor adjacent to a di-iron site in a separate subunit from the catalytic subunit⁹⁻¹¹. Other subclasses of class I RNRs are further divided based on the identity of the metal centers (b-d)¹²⁻¹⁴ with recent reports of a metal-independent class Ie RNR being a deviation¹⁵.

Despite the diversity in how the catalytically essential thiyl-radical is generated, the three classes of RNR share critical features. Although some RNRs reduce nucleoside diphosphates and others triphosphates, all RNRs share the same cognate substrate-effector pairings that determine substrate specificity^{3,5}. Additionally, all RNR active sites are composed of a ten-stranded β/α barrel, which is composed of two antiparallel β sheets that each contain five parallel β strands. A finger loop that contains the cysteine that forms the thiyl-radical connects the two β sheets and inserts itself into the barrel^{6,8,16}.

Following the conserved active site architectures, the mechanism of nucleotide reduction across most RNRs is also conserved^{17,18}. Briefly, the thiyl-radical (C439 in *Escherichia coli*) abstracts a hydrogen from the 3'-carbon of the nucleotide substrate to form a 3'-nucleotide radical^{4,19}. A rearrangement results in the release of the 2'-hydroxyl group as water and the formation of a 3'-keto-2'-deoxynucleotide radical-species intermediate. The radical intermediate is then reduced in two single-electron steps that results in a disulfide between two active cysteines (C225 and C462 in *E. coli*) and a 3'-deoxynucleotide radical. Abstraction of the hydrogen from C439 reforms the active site thiyl-radical and results in deoxynucleotide product (**Figure 1.3**).

1.B: *E. coli* class Ia RNR

The prototype for studying the mechanism and regulation of RNR has been the class Ia RNR from *E. coli*, composed of two homodimeric subunits, referred to as $\alpha 2$ and $\beta 2$ ²⁰.

$\alpha 2$ is the catalytic subunit and contains three nucleotide binding sites¹⁶. Substrate (specifically nucleoside diphosphates) reduction occurs in the active site. The identity of which nucleotide gets reduced is determined by deoxynucleoside triphosphate binding to the second nucleotide binding site, the specificity site, located ~ 15 Å from the active site, according to the pairing rules discussed above². Previous structures of *E. coli* class Ia RNR from our lab showed how the binding of specificity effector results in the reorientation of a loop (loop 2, residues 292-301) to form a favorable binding pocket for its cognate substrate in the active site²¹. The third nucleotide binding site in the $\alpha 2$ subunit is the activity site. The activity site, also referred to as the “cone-domain,” is a four-helix bundle found at the N-terminus of $\alpha 2$ ²². dATP binding to this site results in the formation of an $\alpha 4\beta 4$ complex and inhibition of enzymatic activity²³. ATP can displace dATP at this site to restore activity^{24,25}. The C-terminus of $\alpha 2$ is flexible and contains two redox-active cysteines (C754 and C759) that reduces the disulfide formed in the active site as a result of nucleotide reduction²⁶ (**Figure 1.4**). The ultimate source of reducing

equivalents for *E. coli* class Ia RNR come from NADPH via thioredoxin²⁷ or glutaredoxin^{28,29}.

The $\beta 2$ subunit houses the diferric tyrosyl-radical cofactor (Y122•) that generates the transient thiyl-radical in the active site of $\alpha 2$ ¹⁰ (**Figure 1.4**). It was proposed that the oxidation of C439 in $\alpha 2$ by Y122• in $\beta 2$ occurs via a series of proton-coupled electron transfer (PCET) steps comprising aromatic residues of both subunits: Y122 β \leftrightarrow [W48 β] \leftrightarrow Y356 β \leftrightarrow Y731 α \leftrightarrow Y730 α \leftrightarrow C439 α ³⁰⁻³⁴ (**Figure 1.5**). A recent study suggests that waters may play an important role in PCET at the interface and may act as a proton acceptor/donor³⁵. Following turnover, the radical is returned to Y122 β , where it can perform further rounds of catalysis³⁶. Early site-directed mutagenesis studies showed that each of these residues are critical for enzymatic activity³⁷⁻³⁹, and later the use of unnatural amino acids, NH₂-Y, NO₂-Y and F_n-Ys, site-specifically incorporated in place of pathway Ys have led to the direct detection of the formation of radical at their respective positions^{31,33,36,40}. Although conserved and required for catalytic activity, radical at the W48 position has not been detected and its direct involvement in PCET remains an open question.

1.C: Towards an active structure of *E. coli* class Ia RNR

E. coli class Ia RNR was first isolated in the 1960s²⁰, and despite decades of biochemical and structural efforts, obtaining a structure of the active state that includes both the $\alpha 2$ and $\beta 2$ subunits has remained elusive. Among the reasons that have resulted in this challenging endeavor is that the interaction between the $\alpha 2$ and $\beta 2$ subunits is weak, with a measured K_d of roughly 0.2 μM ³⁹. Additionally, active RNR can exist in a dynamic state of equilibrium with a higher-order oligomeric $\alpha 4\beta 4$ inhibited state as well as the free subunits²⁴, a phenomenon not particularly amenable to structural studies, which benefit from homogeneous populations.

Early seminal sedimentation experiments with *E. coli* class Ia RNR lead to the proposal that active RNR is an $\alpha_2\beta_2$ species^{25,41}. Nearly two decades later, the first crystal structures of β_2 ¹⁰, and shortly after α_2 ¹⁶, were solved. Unfortunately, the C-terminal ~25 and ~35 residues of α_2 and β_2 , respectively, were disordered in the crystal structures. However, the structure of α_2 was solved in the presence of a 20-residue peptide that shared the sequence with the C-terminus of β_2 , which revealed it to be bound within a groove formed by several α -helices in α_2 ¹⁶. Further biochemical experiments showed that the C-terminus of β_2 is critical for α_2 - β_2 interaction³⁹. Nonetheless, the structures revealed that the overall shapes of α_2 and β_2 were complementary in nature, from which a two-fold symmetric $\alpha_2\beta_2$ “docking model” was proposed¹⁶ (**Figure 1.6**). The docking model placed C439, the site of the transient active site radical, approximately 35 Å from the site of Y122• in β_2 , a distance for biological long-range electron transfer that was unprecedented at the time that it was proposed.

A key short-coming of the docking model was the lack of structural information at the α_2 - β_2 interface. Notably, the C-terminus of the β_2 subunit, which contains Y356, a critical residue on the PCET pathway that was thought to bridge the radical translocation across the subunit-subunit interface^{30,39}, was unresolved in the modeled crystal structure. Y356 was also structurally absent along the C-terminal β_2 peptide that was co-crystallized with α_2 . Between the last visible residue in the crystal structure of β_2 and the β_2 C-terminal residues visible along α_2 , there remained approximately 20 residues whose structure and location were unaccounted for by the docking model, the result being a large cavity at the α_2 - β_2 interface (**Figure 1.7**). However, radical transfer over such a long distance involving several residues would require tight coordination and protection of the radical species, an expectation that could not be reconciled with the proposed docking model.

Nonetheless, spectroscopic and biochemical experiments over the years have corroborated the overall $\alpha_2\beta_2$ structure proposed by the docking model. Notably, pulsed electron-electron double resonance (PELDOR) experiments site-specifically

incorporating 3-aminotyrosine (NH₂-Y) and 3-hydroxytyrosine (DOPA) radical traps at various positions along the radical transfer pathway, allowed for distance measurements to be made between key residues in $\alpha 2$ and $\beta 2$ that largely agreed with the distances predicted by the docking model⁴². The phenomenon that allowed for the PELDOR experiments is that *E. coli* class Ia RNR exhibits half-sites reactivity^{32,36,43} – although there are two active sites within the $\alpha 2$ subunit, nucleotide reduction between one β/α must occur prior to it happening in the second pair. Therefore, the measured distances were between the radical trapped along the PCET pathway of one β/α pair and Y122• of the opposite β . However, half-sites reactivity could not be structurally explained by the docking model. In a symmetric $\alpha 2\beta 2$, there would presumably exist two equal PCET pathways and the docking model could not explain RNRs propensity towards asymmetric nucleotide reduction.

In addition to biochemical studies, low-resolution structural evidence continued to support the validity of the docking model. Small-angle X-ray scattering (SAXS) experiments revealed that under active conditions, *E. coli* RNR is indeed a tight, globular species, with the docking model fitting well into the proposed low-resolution shape reconstruction²⁴ (**Figure 1.8**).

Studies of NH₂Y-substituted $\alpha 2$ (residues 730, 731) and $\beta 2$ (residue 356) lead to the striking observation that the trapped NH₂Y• is incredibly stable, persisting on the minute timescale⁴⁴. It was thought at the time that the stability of this radical may be the consequence of the formation of a tighter, longer-lived complex, as these residues are at least partially solvent-exposed in their free-subunit structures¹⁶. Indeed, it was found that the K_d for the NH₂Y730- $\alpha 2$ /WT- $\beta 2$ was 7 nM, compared to the K_d of 0.2 μ M measured for the WT- $\alpha 2$ /WT- $\beta 2$ interaction, and the dissociation rate constant was slowed by approximately 10⁴⁴⁵. Further, negative-stain electron microscopy (EM) experiments revealed that formation of the NH₂Y• manifests structurally as a kinetically stable $\alpha 2\beta 2$ complex, which lead to a 32-Å resolution reconstruction. Docking of crystal structures of the individual $\alpha 2$ and $\beta 2$ subunits into the EM density recapitulated a

structure resembling the docking model⁴⁵ (**Figure 1.8**). Despite its relatively low resolution, the EM study led to the realization that the strategy of trapping pathway radicals to generate transiently stable $\alpha_2\beta_2$ complexes could be a promising avenue by which to obtain a higher-resolution structure of the active complex.

Although these transient $\alpha_2\beta_2$ complexes were not amenable to crystallographic studies that typically require timescales on the order of days to achieve crystallization, our improved biochemical understanding of active RNR coincided with the timely rapid technological advancements occurring in a different structural biology technique, cryo-electron microscopy (cryo-EM). Although cryo-EM had been used to study biological samples for decades, a few recent technological breakthroughs are credited for ushering in this current “resolution revolution,” which has allowed for structures of smaller, more heterogeneous biological specimens to be solved⁴⁶. Firstly, the development of direct-electron detectors allowed for micrographs to be collected at higher signal-to-noise ratios compared to the previously widely used charge-coupled device (CCD) cameras⁴⁷. Advancements also came on the software side with the ability to perform beam-induced motion correction of movie frames, further improving signal-to-noise, and the development of algorithms based on maximum-likelihood procedures, which allowed for unsupervised 3D classification to deal with inherent heterogeneity issues in biological samples⁴⁸⁻⁵².

1.D: Goals of this dissertation

Long considered the “holy grail” in the field, a combination of knowledge gained via biochemical studies and technological advancements in cryo-EM have allowed us to obtain for the first time, a structure of the active RNR $\alpha_2\beta_2$ complex. We discuss two $\alpha_2\beta_2$ complexes, trapped using different methods of perturbing the native radical transfer pathway.

The first utilizes a doubly-substituted construct of $\beta 2$ wherein a highly-conserved interface residue, E52, was mutated to Q, and the tyrosyl-radical cofactor Y122• was site-specifically replaced with a (2,3,5)-trifluorotyrosine radical (F₃Y122•), making the radical-cofactor a “hotter” oxidant that results in a transiently stable Y356•^{36,53,54}. This complex was solved in the presence of wildtype- $\alpha 2$ and native substrate and effector GDP and TTP, respectively. The second $\alpha 2\beta 2$ complex was solved with wildtype enzyme in the presence of effector ATP and stoichiometric substrate inhibitor N₃UDP, which generates a unique nitrogen-centered radical, N• in the active site⁵⁵ that prevents re-oxidation of Y122.

Together, these structures reveal unprecedented insight into the dynamics and regulation of RNR in its active state. We follow with a brief discussion of class Ia RNR from T4 bacteriophage, for which *E. coli* is its native host. The two RNRs share very high sequence similarity yet appear to employ drastically different modes of oligomeric regulation. We end with an eye to the future and discuss open questions and ways to approach them, given our improved understanding of RNR function.

1.E References

- 1 Nordlund, P. & Reichard, P. Ribonucleotide reductases. *Annu Rev Biochem* **75**, 681-706, doi:10.1146/annurev.biochem.75.103004.142443 (2006).
- 2 Brown, N. C. & Reichard, P. Role of effector binding in allosteric control of ribonucleoside diphosphate reductase. *J Mol Biol* **46**, 39-55 (1969).
- 3 Reichard, P. Ribonucleotide reductases: substrate specificity by allostery. *Biochem Biophys Res Commun* **396**, 19-23, doi:10.1016/j.bbrc.2010.02.108 (2010).
- 4 Licht, S., Gerfen, G. J. & Stubbe, J. Thiyl radicals in ribonucleotide reductases. *Science* **271**, 477-481, doi:10.1126/science.271.5248.477 (1996).
- 5 Hofer, A., Crona, M., Logan, D. T. & Sjöberg, B. M. DNA building blocks: keeping control of manufacture. *Crit Rev Biochem Mol Biol* **47**, 50-63, doi:10.3109/10409238.2011.630372 (2012).
- 6 Sintchak, M. D., Arjara, G., Kellogg, B. A., Stubbe, J. & Drennan, C. L. The crystal structure of class II ribonucleotide reductase reveals how an allosterically regulated monomer mimics a dimer. *Nat Struct Biol* **9**, 293-300, doi:10.1038/nsb774 (2002).
- 7 Goulian, M. & Beck, W. S. Purification and properties of cobamide-dependent ribonucleotide reductase from *Lactobacillus leichmannii*. *J Biol Chem* **241**, 4233-4242 (1966).
- 8 Logan, D. T., Andersson, J., Sjöberg, B. M. & Nordlund, P. A glycy radical site in the crystal structure of a class III ribonucleotide reductase. *Science* **283**, 1499-1504, doi:10.1126/science.283.5407.1499 (1999).
- 9 Bollinger, J. M., Jr. *et al.* Mechanism of assembly of the tyrosyl radical-dinuclear iron cluster cofactor of ribonucleotide reductase. *Science* **253**, 292-298, doi:10.1126/science.1650033 (1991).
- 10 Nordlund, P., Sjöberg, B. M. & Eklund, H. Three-dimensional structure of the free radical protein of ribonucleotide reductase. *Nature* **345**, 593-598, doi:10.1038/345593a0 (1990).
- 11 Atkin, C. L., Thelander, L., Reichard, P. & Lang, G. Iron and free radical in ribonucleotide reductase. Exchange of iron and Mossbauer spectroscopy of the protein B2 subunit of the *Escherichia coli* enzyme. *J Biol Chem* **248**, 7464-7472 (1973).
- 12 Cotruvo, J. A., Jr., Stich, T. A., Britt, R. D. & Stubbe, J. Mechanism of assembly of the dimanganese-tyrosyl radical cofactor of class Ib ribonucleotide reductase: enzymatic generation of superoxide is required for tyrosine oxidation via a Mn(III)Mn(IV) intermediate. *J Am Chem Soc* **135**, 4027-4039, doi:10.1021/ja312457t (2013).
- 13 Rose, H. R. *et al.* Structural Basis for Superoxide Activation of *Flavobacterium johnsoniae* Class I Ribonucleotide Reductase and for Radical Initiation by Its Dimanganese Cofactor. *Biochemistry* **57**, 2679-2693, doi:10.1021/acs.biochem.8b00247 (2018).
- 14 Dassama, L. M., Boal, A. K., Krebs, C., Rosenzweig, A. C. & Bollinger, J. M., Jr. Evidence that the beta subunit of *Chlamydia trachomatis* ribonucleotide

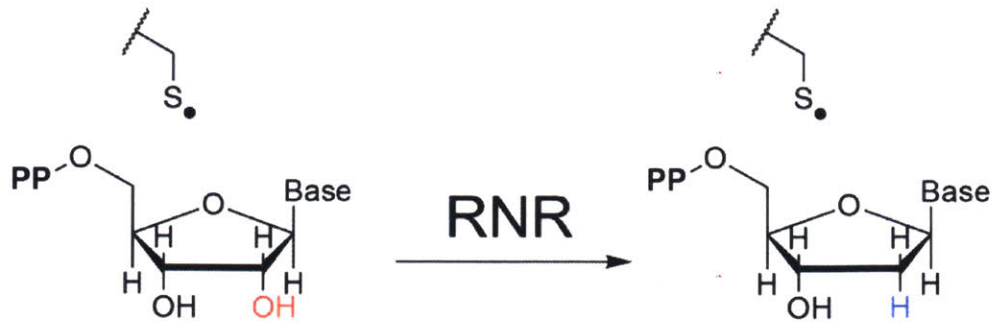
- reductase is active with the manganese ion of its manganese(IV)/iron(III) cofactor in site 1. *J Am Chem Soc* **134**, 2520-2523, doi:10.1021/ja211314p (2012).
- 15 Blaesi, E. J. *et al.* Metal-free class Ia ribonucleotide reductase from pathogens initiates catalysis with a tyrosine-derived dihydroxyphenylalanine radical. *Proc Natl Acad Sci U S A* **115**, 10022-10027, doi:10.1073/pnas.1811993115 (2018).
- 16 Uhlin, U. & Eklund, H. Structure of ribonucleotide reductase protein R1. *Nature* **370**, 533-539, doi:10.1038/370533a0 (1994).
- 17 Licht SS, J. S., J. Mechanistic Investigations of Ribonucleotide Reductases. *Pergamon*, 163-203 (1999).
- 18 Stubbe, J. & van Der Donk, W. A. Protein Radicals in Enzyme Catalysis. *Chem Rev* **98**, 705-762 (1998).
- 19 Stubbe, J. & Ackles, D. On the mechanism of ribonucleoside diphosphate reductase from *Escherichia coli*. Evidence for 3'-C-H bond cleavage. *J Biol Chem* **255**, 8027-8030 (1980).
- 20 Brown, N. C., Canellakis, Z. N., Lundin, B., Reichard, P. & Thelander, L. Ribonucleoside diphosphate reductase. Purification of the two subunits, proteins B1 and B2. *Eur J Biochem* **9**, 561-573, doi:10.1111/j.1432-1033.1969.tb00646.x (1969).
- 21 Zimanyi, C. M., Chen, P. Y., Kang, G., Funk, M. A. & Drennan, C. L. Molecular basis for allosteric specificity regulation in class Ia ribonucleotide reductase from *Escherichia coli*. *Elife* **5**, e07141, doi:10.7554/eLife.07141 (2016).
- 22 Aravind, L., Wolf, Y. I. & Koonin, E. V. The ATP-cone: an evolutionarily mobile, ATP-binding regulatory domain. *J Mol Microbiol Biotechnol* **2**, 191-194 (2000).
- 23 Zimanyi, C. M. *et al.* Tangled up in knots: structures of inactivated forms of *E. coli* class Ia ribonucleotide reductase. *Structure* **20**, 1374-1383, doi:10.1016/j.str.2012.05.009 (2012).
- 24 Ando, N. *et al.* Structural interconversions modulate activity of *Escherichia coli* ribonucleotide reductase. *Proc Natl Acad Sci U S A* **108**, 21046-21051, doi:10.1073/pnas.1112715108 (2011).
- 25 Brown, N. C. & Reichard, P. Ribonucleoside diphosphate reductase. Formation of active and inactive complexes of proteins B1 and B2. *J Mol Biol* **46**, 25-38 (1969).
- 26 Aberg, A. *et al.* Evidence for two different classes of redox-active cysteines in ribonucleotide reductase of *Escherichia coli*. *J Biol Chem* **264**, 12249-12252 (1989).
- 27 Mao, S. S. *et al.* A model for the role of multiple cysteine residues involved in ribonucleotide reduction: amazing and still confusing. *Biochemistry* **31**, 9733-9743, doi:10.1021/bi00155a029 (1992).
- 28 Holmgren, A. Glutathione-dependent synthesis of deoxyribonucleotides. Purification and characterization of glutaredoxin from *Escherichia coli*. *J Biol Chem* **254**, 3664-3671 (1979).
- 29 Holmgren, A. Glutathione-dependent synthesis of deoxyribonucleotides. Characterization of the enzymatic mechanism of *Escherichia coli* glutaredoxin. *J Biol Chem* **254**, 3672-3678 (1979).

- 30 Stubbe, J., Nocera, D. G., Yee, C. S. & Chang, M. C. Radical initiation in the class I ribonucleotide reductase: long-range proton-coupled electron transfer? *Chem Rev* **103**, 2167-2201, doi:10.1021/cr020421u (2003).
- 31 Seyedsayamdost, M. R., Xie, J., Chan, C. T., Schultz, P. G. & Stubbe, J. Site-specific insertion of 3-aminotyrosine into subunit alpha2 of E. coli ribonucleotide reductase: direct evidence for involvement of Y730 and Y731 in radical propagation. *J Am Chem Soc* **129**, 15060-15071, doi:10.1021/ja076043y (2007).
- 32 Seyedsayamdost, M. R. & Stubbe, J. Site-specific replacement of Y356 with 3,4-dihydroxyphenylalanine in the beta2 subunit of E. coli ribonucleotide reductase. *J Am Chem Soc* **128**, 2522-2523, doi:10.1021/ja057776q (2006).
- 33 Yokoyama, K., Smith, A. A., Corzilius, B., Griffin, R. G. & Stubbe, J. Equilibration of tyrosyl radicals (Y356*, Y731*, Y730*) in the radical propagation pathway of the Escherichia coli class Ia ribonucleotide reductase. *J Am Chem Soc* **133**, 18420-18432, doi:10.1021/ja207455k (2011).
- 34 Yokoyama, K., Uhlin, U. & Stubbe, J. Site-specific incorporation of 3-nitrotyrosine as a probe of pKa perturbation of redox-active tyrosines in ribonucleotide reductase. *J Am Chem Soc* **132**, 8385-8397, doi:10.1021/ja101097p (2010).
- 35 Nick, T. U., Ravichandran, K. R., Stubbe, J., Kasanmascheff, M. & Bennati, M. Spectroscopic Evidence for a H Bond Network at Y356 Located at the Subunit Interface of Active E. coli Ribonucleotide Reductase. *Biochemistry* **56**, 3647-3656, doi:10.1021/acs.biochem.7b00462 (2017).
- 36 Ravichandran, K. R., Minnihhan, E. C., Wei, Y., Nocera, D. G. & Stubbe, J. Reverse Electron Transfer Completes the Catalytic Cycle in a 2,3,5-Trifluorotyrosine-Substituted Ribonucleotide Reductase. *J Am Chem Soc* **137**, 14387-14395, doi:10.1021/jacs.5b09189 (2015).
- 37 Ekberg, M., Sahlin, M., Eriksson, M. & Sjoberg, B. M. Two conserved tyrosine residues in protein R1 participate in an intermolecular electron transfer in ribonucleotide reductase. *J Biol Chem* **271**, 20655-20659, doi:10.1074/jbc.271.34.20655 (1996).
- 38 Rova, U. *et al.* Evidence by site-directed mutagenesis supports long-range electron transfer in mouse ribonucleotide reductase. *Biochemistry* **34**, 4267-4275, doi:10.1021/bi00013a016 (1995).
- 39 Climent, I., Sjoberg, B. M. & Huang, C. Y. Site-directed mutagenesis and deletion of the carboxyl terminus of Escherichia coli ribonucleotide reductase protein R2. Effects on catalytic activity and subunit interaction. *Biochemistry* **31**, 4801-4807, doi:10.1021/bi00135a009 (1992).
- 40 Minnihhan, E. C., Seyedsayamdost, M. R., Uhlin, U. & Stubbe, J. Kinetics of radical intermediate formation and deoxynucleotide production in 3-aminotyrosine-substituted Escherichia coli ribonucleotide reductases. *J Am Chem Soc* **133**, 9430-9440, doi:10.1021/ja201640n (2011).
- 41 Thelander, L. Physicochemical characterization of ribonucleoside diphosphate reductase from Escherichia coli. *J Biol Chem* **248**, 4591-4601 (1973).
- 42 Seyedsayamdost, M. R., Chan, C. T., Mugnaini, V., Stubbe, J. & Bennati, M. PELDOR spectroscopy with DOPA-beta2 and NH2Y-alpha2s: distance measurements between residues involved in the radical propagation pathway of

- E. coli ribonucleotide reductase. *J Am Chem Soc* **129**, 15748-15749, doi:10.1021/ja076459b (2007).
- 43 Salowe, S. P., Ator, M. A. & Stubbe, J. Products of the inactivation of ribonucleoside diphosphate reductase from Escherichia coli with 2'-azido-2'-deoxyuridine 5'-diphosphate. *Biochemistry* **26**, 3408-3416, doi:10.1021/bi00386a024 (1987).
- 44 Seyedsayamdost, M. *Investigations of the mechanism of radical propagation in E. coli ribonucleotide reductase by site-specific incorporation of unnatural amino acids.*, Massachusetts Institute of Technology, (2007).
- 45 Minnihan, E. C. *et al.* Generation of a stable, aminotyrosyl radical-induced alpha2beta2 complex of Escherichia coli class Ia ribonucleotide reductase. *Proc Natl Acad Sci U S A* **110**, 3835-3840, doi:10.1073/pnas.1220691110 (2013).
- 46 Bai, X. C., McMullan, G. & Scheres, S. H. How cryo-EM is revolutionizing structural biology. *Trends Biochem Sci* **40**, 49-57, doi:10.1016/j.tibs.2014.10.005 (2015).
- 47 Wu, S., Armache, J. P. & Cheng, Y. Single-particle cryo-EM data acquisition by using direct electron detection camera. *Microscopy (Oxf)* **65**, 35-41, doi:10.1093/jmicro/dfv355 (2016).
- 48 Sigworth, F. J. A maximum-likelihood approach to single-particle image refinement. *J Struct Biol* **122**, 328-339, doi:10.1006/jsbi.1998.4014 (1998).
- 49 Scheres, S. H. RELION: implementation of a Bayesian approach to cryo-EM structure determination. *J Struct Biol* **180**, 519-530, doi:10.1016/j.jsb.2012.09.006 (2012).
- 50 Scheres, S. H. *et al.* Disentangling conformational states of macromolecules in 3D-EM through likelihood optimization. *Nat Methods* **4**, 27-29, doi:10.1038/nmeth992 (2007).
- 51 Elad, N., Clare, D. K., Salbil, H. R. & Orlova, E. V. Detection and separation of heterogeneity in molecular complexes by statistical analysis of their two-dimensional projections. *J Struct Biol* **162**, 108-120, doi:10.1016/j.jsb.2007.11.007 (2008).
- 52 Lyumkis, D., Brilot, A. F., Theobald, D. L. & Grigorieff, N. Likelihood-based classification of cryo-EM images using FREALIGN. *J Struct Biol* **183**, 377-388, doi:10.1016/j.jsb.2013.07.005 (2013).
- 53 Lin, Q. *et al.* Glutamate 52-beta at the alpha/beta subunit interface of Escherichia coli class Ia ribonucleotide reductase is essential for conformational gating of radical transfer. *J Biol Chem* **292**, 9229-9239, doi:10.1074/jbc.M117.783092 (2017).
- 54 Oyala, P. H. *et al.* Biophysical Characterization of Fluorotyrosine Probes Site-Specifically Incorporated into Enzymes: E. coli Ribonucleotide Reductase As an Example. *J Am Chem Soc* **138**, 7951-7964, doi:10.1021/jacs.6b03605 (2016).
- 55 Fritscher, J. *et al.* Structure of the nitrogen-centered radical formed during inactivation of E. coli ribonucleotide reductase by 2'-azido-2'-deoxyuridine-5'-diphosphate: trapping of the 3'-ketonucleotide. *J Am Chem Soc* **127**, 7729-7738, doi:10.1021/ja043111x (2005).

1.F Figures and Tables

A



B

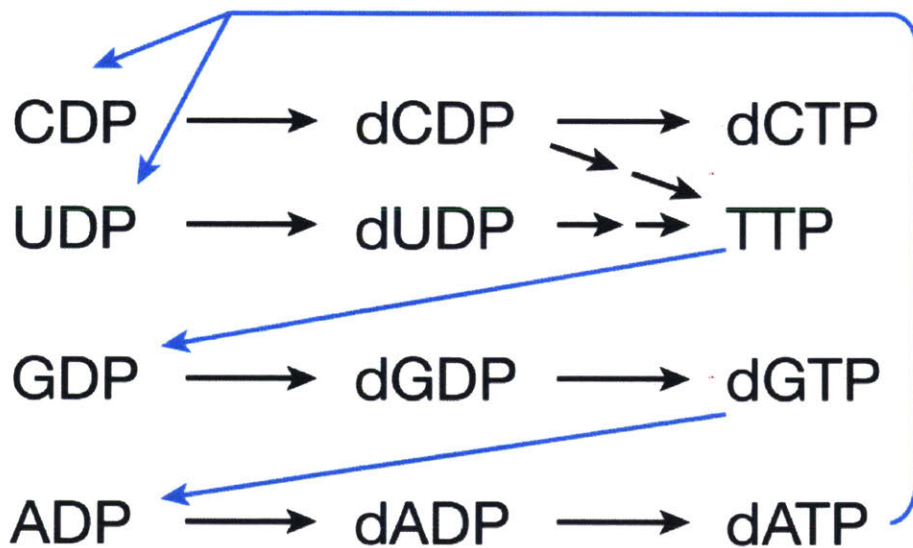


Figure 1.1: RNR catalyzes the reduction of all four ribonucleotides. A) RNRs catalyze the reduction of ribonucleotides at their 2'-C to generate their deoxynucleotide counterparts. The reaction is initiated by a transient thiyl-radical generated in the active site. B) Specificity regulation in RNRs is conserved. Certain RNRs reduce nucleoside diphosphates (NDPs) whereas others the triphosphates (NTPs). Generalized NDP regulation scheme is shown.

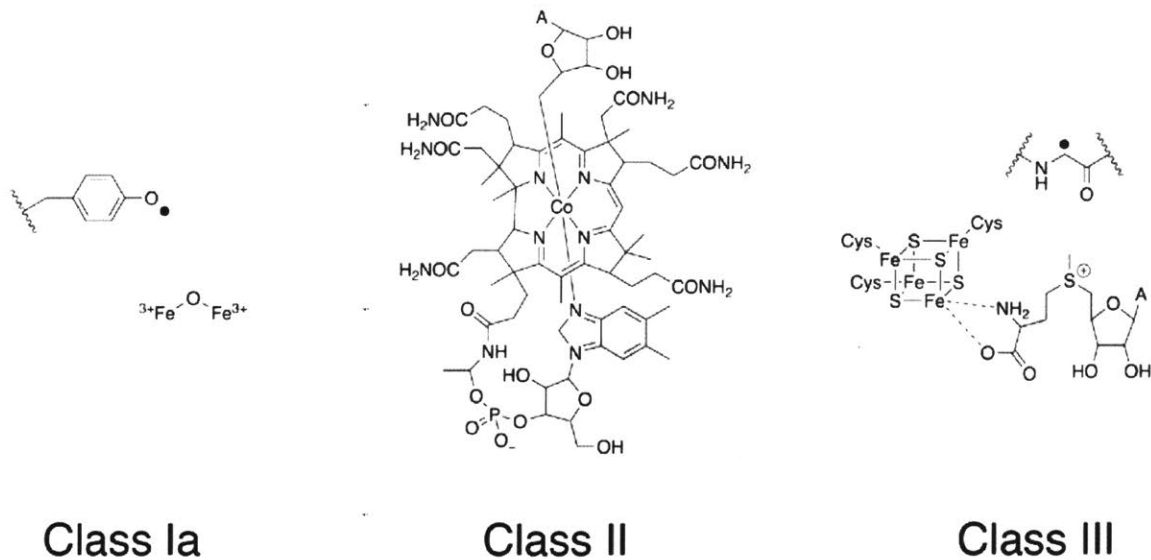


Figure 1.2: The metallo-cofactors of RNR. The diiron tyrosyl-radical cofactor of the class Ia RNR is shown as a representative member of the class I RNRs. Class II RNRs utilize an adenosylcobalamin cofactor and class III RNRs generate a stable glycy radical cofactor via a 4Fe-4S cluster and S-adenosylmethionine.

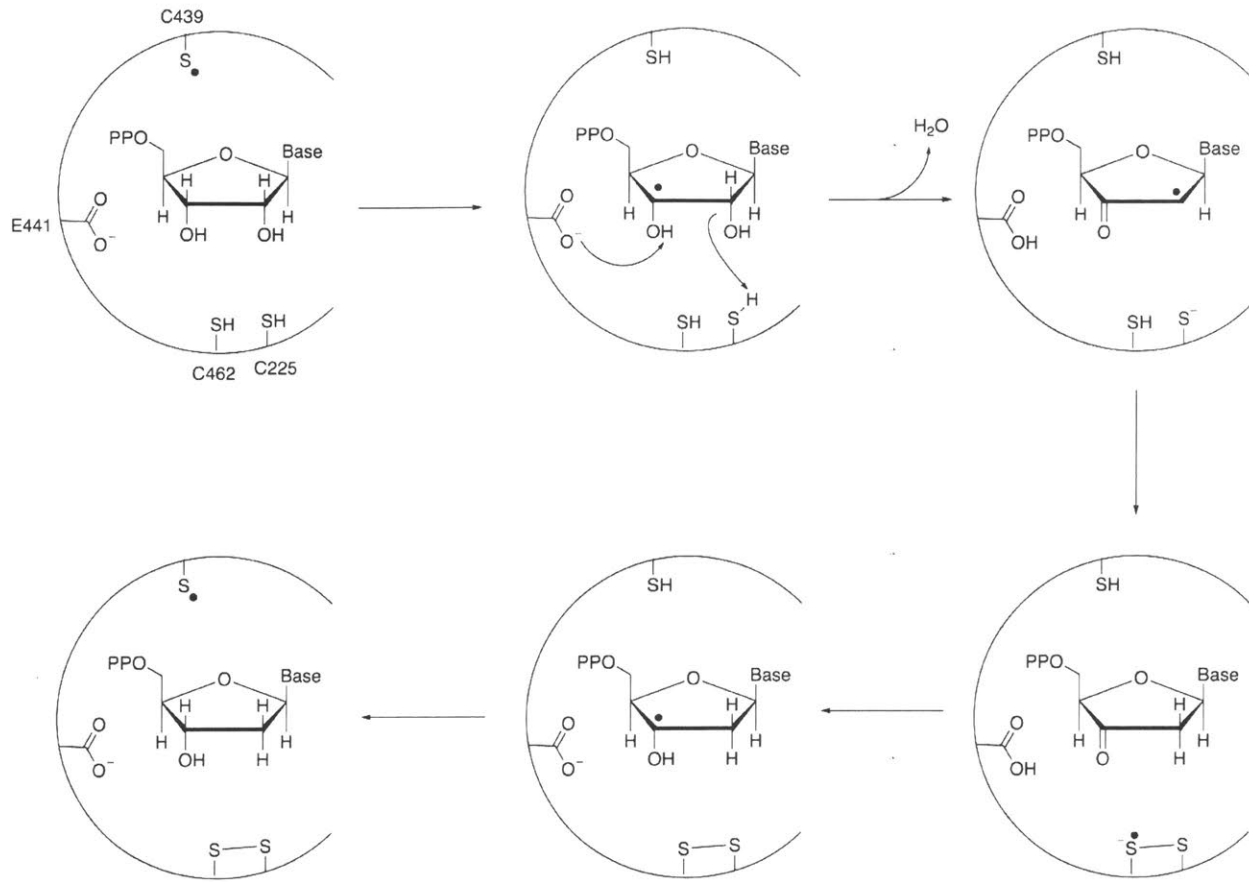


Figure 1.3: Nucleotide reduction mechanism conserved in most RNRs. The active-site numberings from *E. coli* class Ia RNR are shown.

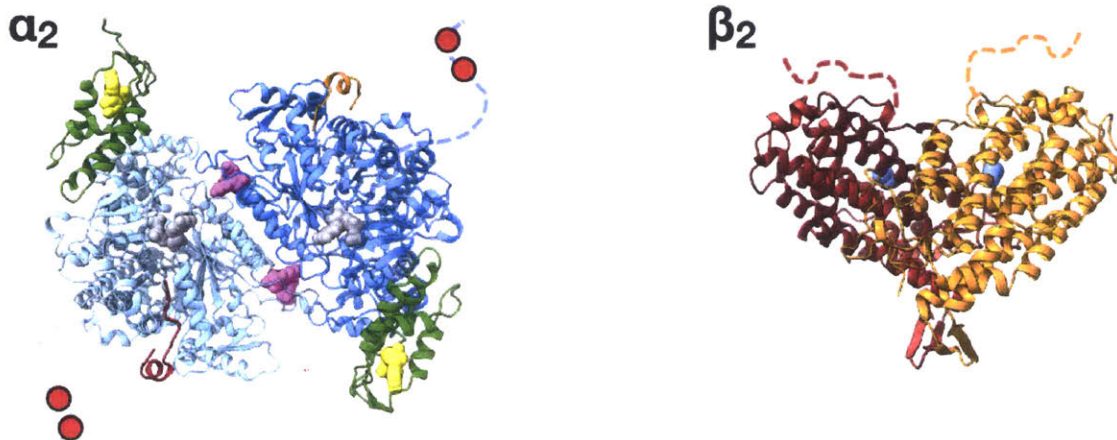


Figure 1.4: The subunits of *E. coli* class Ia RNR are composed of two homodimeric subunits. Left: α_2 , shown in the blue/cyan, is the catalytic subunit. Substrate (grey spheres) reduction occurs in the active site, and dNTP (magenta spheres) binding to the allosteric specificity site confers substrate specificity. dATP or ATP (yellow spheres) can bind to the N-terminal cone-domain, or activity site (shown in green), to inactivate or reactivate the enzyme, respectively. C754 and C759, shown in red balls, are a redox active pair of cysteines found at the structurally flexible C-terminus that re-reduce the disulfide that forms in the active site as a result of turnover. Right: β_2 , shown in orange/red, houses the diiron tyrosyl-radical cofactor (blue spheres). The C-terminus of β_2 in its free-subunit state is also structurally disordered. PDB: 5CNV for both subunits.

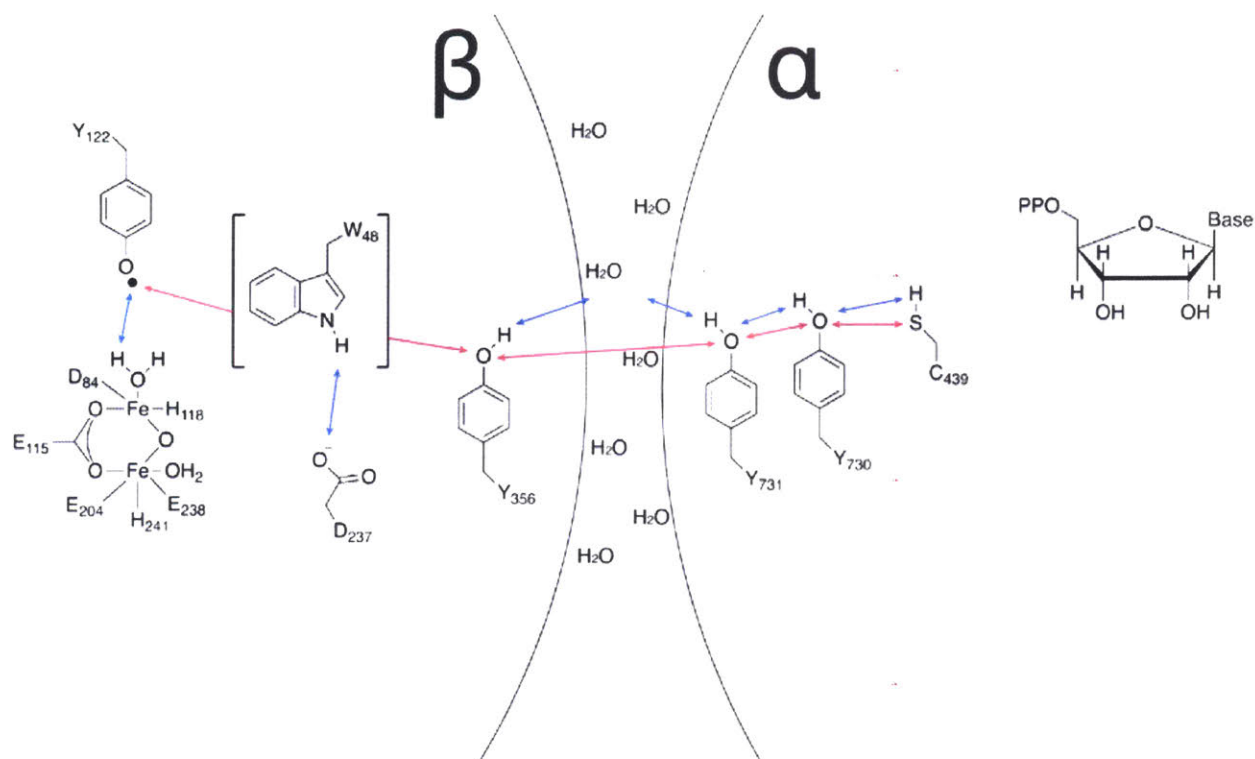


Figure 1.5: C439 α is oxidized by Y122 β via a proposed proton-coupled electron transfer pathway. Electron transfer steps are shown in red arrows and proton transfer steps in blue arrows. PCET occurs by an orthogonal mechanism in β and colinear in α . The direct involvement of W48 in PCET remains an open question.

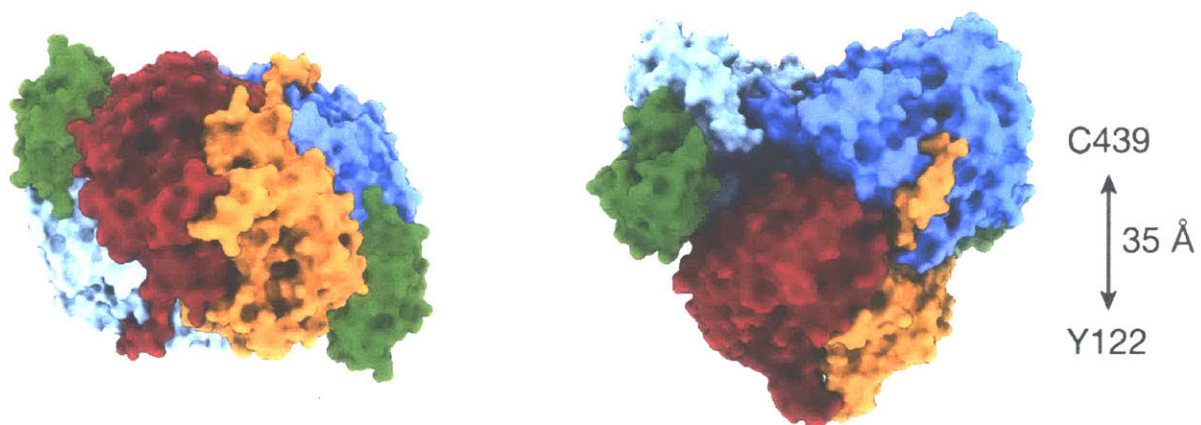


Figure 1.6: The docking model of *E. coli* class Ia RNR. Left: bottom view, Right: front view. When the crystal structures of α_2 and β_2 were solved, the tight, symmetric docking model, shown here, was proposed based on shape complementarity. Based on the model, the proposed distance of C439 α oxidation by Y122 β was ~ 35 Å. α_2 and β_2 shown in blue/cyan and orange/red, respectively. The cone domains of α_2 are shown in green.

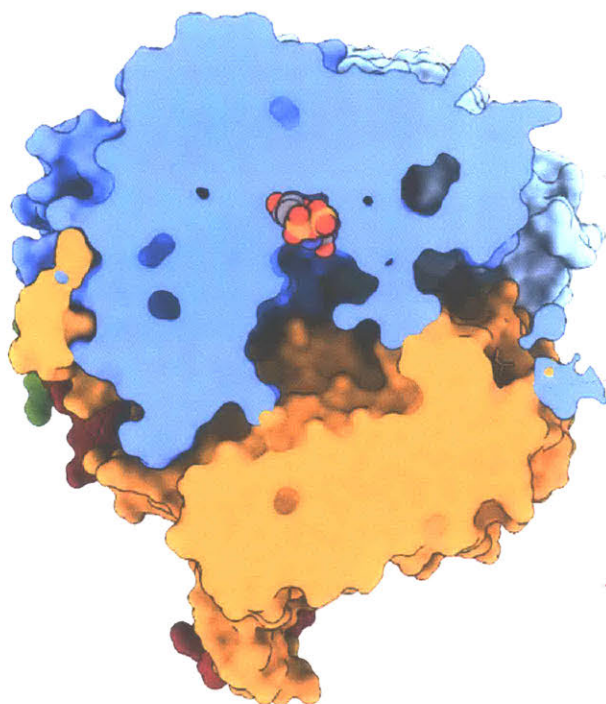
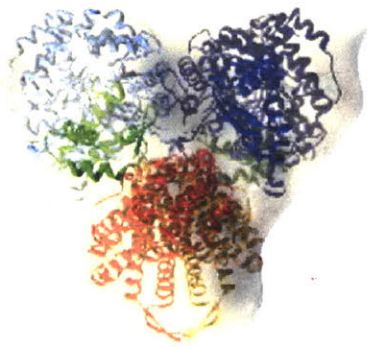
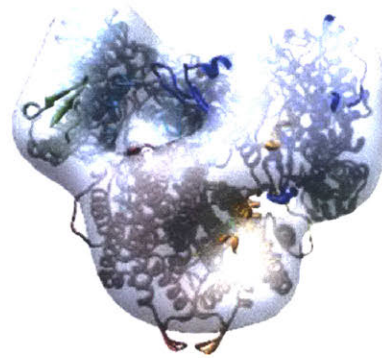


Figure 1.7: The docking model of $\alpha 2\beta 2$ lacks significant structural information. The original docking model was missing structural information for residues 341-359 of $\beta 2$. As such, there remained a large cavity under the active site and substrate, an open environment that is not quite suited for radical-mediated chemistry.



WT-α2β2



**NH₂Y730-α2
WT-β2**

Figure 1.8: Low-resolution structures of *E. coli* class Ia $\alpha_2\beta_2$ complex. Left: 50-Å resolution SAXS reconstruction (transparent yellow) generated using WT- $\alpha_2\beta_2$ with docking model fit into the density. Right: 32-Å resolution negative-stain EM reconstruction generated using WT- β_2 and NH₂Y730- α_2 with docking model fit into the density.

Chapter 2

Cryo-EM structure of an active $\alpha_2\beta_2$ complex reveals conformational insight into PCET and enzymatic turnover

We thank Qinghui Lin for generating and providing the E52Q/(2,3,5)trifluorotyrosine122(F₃Y122)- β_2 construct that was critical in the completion of this project. We thank Dr. Alex Taguchi who helped identify initial sample preparation conditions to pursue and optimize sample preparation conditions for cryo-EM. Dr. Chang Cui and Albert Kim performed follow-up experiments in the presence of substrate/effector pair GDP/TTP. Tristan Bepler developed the particle picking software that was used and was very helpful in troubleshooting and debugging issues that arose. We thank Dr. Ed Brignole for his advice in data processing. The data discussed herein were collected at the Cryo-EM Facility at UMass Medical School Worcester with the help of Dr. Kangkang Song.

2.A Summary

Ribonucleotide reductases (RNR) are the only known enzymes capable of generating 2'-deoxynucleotides *de novo* and are thus critical in the maintenance and regulation of DNA biosynthesis and repair. All RNRs are capable of reducing all four ribonucleotides (U,C,A,G), with substrate specificity determined by cognate pairing with deoxynucleotides. Class Ia RNR, of which *Escherichia coli* is the prototype, is composed of two homodimeric subunits, α_2 where substrate reduction occurs, and β_2 , which utilizes a di-iron site to generate a tyrosyl-radical cofactor that goes on to initiate chemistry in α_2 . In the active $\alpha_2\beta_2$ state, the radical transfer from β_2 to α_2 has been proposed to occur via a highly unusual long-range proton-coupled electron transfer involving several amino acid side chains, but in the absence of an atomic-resolution structure of the active complex, the full pathway has remained structurally elusive. Here, we report the near-atomic resolution structure of the active $\alpha_2\beta_2$ complex of *E. coli* class Ia RNR with the aforementioned radical transfer pathway fully resolved, the first high-resolution structure of any active RNR. Our structure, which is an asymmetric complex with the interface occurring primarily between β_2 and one α monomer, explains why only one competent pathway can form at a given time. The structure also provides deep insights into the complex conformational dynamics that must occur on route to the enzyme performing this remarkable biologically essential chemistry.

2.B Introduction

Ribonucleotide reductase (RNR) is the sole enzyme in all organisms capable of *de novo* generation of 2'-deoxynucleotides, utilizing allosteric modes of specificity regulation to be able to reduce all four nucleotide substrates (U,C,A,G) (**Figure 2.1**)¹⁻³. Thus, RNR plays a major role in maintaining the nucleotide pool balance necessary for proper DNA biosynthesis and repair⁴. RNRs are divided into three classes based on the identity of the cofactor used to generate the active site thiyl radical required to initiate chemistry⁴. Class Ia RNR from *Escherichia coli*, the prototypic RNR and the focus of this study, utilizes a diferric-tyrosyl radical cofactor (Y122•) in the small subunit (β 2) to transiently generate a cysteine thiyl radical (C439•) in the large subunit (α 2) for catalysis (**Figure 2.2**)⁴⁻⁶. The radical transfer from Y122 β to C439 α is proposed to occur via a series of proton-coupled electron transfer (PCET) steps across several conserved aromatic residues: Y122 β \leftrightarrow W48 β \leftrightarrow Y356 β \leftrightarrow Y731 α \leftrightarrow Y730 α \leftrightarrow C439 α ⁷⁻¹⁰. Following turnover, the radical returns to its resting state on Y122 β ¹¹. Despite its critical role in radical transfer, Y356 β has never been structurally visualized.

The reducing equivalents for nucleotide reduction come from a pair of redox active cysteines in the active site, C225 and C462, that get oxidized concomitant with product formation (**Figure 2.3**)^{12,13}. Before additional rounds of turnover can occur, the disulfide in the active site is re-reduced by a second pair of cysteines, C754 and C759, found at the C-terminus of α ¹². The resulting disulfide is reduced by thioredoxin/thioredoxin reductase with NADPH as the ultimate source of electrons¹². In the absence of thioredoxin, glutaredoxin can be used to reduce the disulfide^{14,15}. The importance of the C-terminus of β 2 also cannot be understated. In addition to positioning Y356 at the α 2- β 2 interface for PCET, the C-terminus of β is critical for subunit interaction with α 2¹⁶.

Despite the essential role of both subunits' C-termini, the last ~35 residues of β (of 375) and last ~25 residues of α (of 761) have always been disordered in crystal structures of the respective subunits^{17,18}. Co-crystal structures of α 2 with a peptide-mimic of the β C-

terminus showed that the last ~15 residues of β sit within a groove formed by two helices in α (formed by residues 340-350, 710-726) (**Figure 2.2**), providing partial structural evidence of how the two subunits may interact¹⁸. However, this structural snapshot still left ~20 residues of β , including the position of Y356, structurally unresolved.

Like many RNRs, *E. coli* class Ia RNR exists in a dynamic state of oligomeric equilibrium¹⁹ (**Figure 2.2**). Overall enzymatic activity is regulated by an N-terminal four-helix bundle referred to as the cone-domain, comprising the first ~100 residues of α ^{18,20}. dATP binding to this site causes a dramatic shift in quaternary structure to form an inactive $\alpha_4\beta_4$ state that precludes radical transfer between the two subunits²¹. In the crystal structure of $\alpha_4\beta_4$, the C-terminal 13 residues of β were ordered and observed along the same groove within α described above, suggesting these contacts are preserved between different oligomeric states of the enzyme²². ATP can displace dATP at the cone-domain to restore activity by shifting the equilibrium towards an active $\alpha_2\beta_2$ complex^{19,23}.

In the absence of an atomic model for the $\alpha_2\beta_2$ complex, a tight, symmetric $\alpha_2\beta_2$ “docking model” was proposed based on shape complementarity and by aligning two-fold symmetry axes of the crystal structures of the individual α_2 and β_2 subunits¹⁸ (**Figure 2.2**). Since then, low-resolution structural evidence from small angle X-ray scattering (SAXS)¹⁹ and negative-stain electron microscopy (EM)⁹ experiments have supported a compact $\alpha_2\beta_2$ complex as the active state. In addition, pulsed electron-electron double resonance (PELDOR) spectroscopy experiments allowed for the measurement of distances between key residues along the PCET pathway that substantiated those estimated using the docking model²⁴. Strikingly, the measured distances of 38.1 ± 1.2 and 38.7 ± 1.8 Å, corresponding to the diagonal distances (i.e. between the two pathways) between Y122-Y731 and Y122-Y730, respectively, matched closely with the same distances estimated using the docking model, which were 38.5 ± 1.3 and 40.1 ± 1.3 Å, respectively.

The key phenomenon that allowed for the PELDOR experiments to be so informative was that *E. coli* class Ia RNR exhibits half-sites reactivity in that radical transfer occurs within only one of the two possible pathways^{11,24-26}. It has repeatedly been shown for example, that only 0.5 equivalents of some substrate analog inhibitors are required to abolish all enzymatic activity²⁷⁻³⁰. However, the biochemical observations of half-sites reactivity have led to questions regarding the structurally symmetric docking-model. How does inhibiting one of the two active sites in $\alpha 2$ lead to complete inhibition? And how does the enzyme prevent both radical transfer pathways from firing simultaneously?

Towards answering these open questions and others, it has long been a goal to obtain a high-resolution structure of the active $\alpha 2\beta 2$ complex³¹. However, the weak and transient nature of the $\alpha 2$ - $\beta 2$ interaction in the active state has complicated such efforts. Under active conditions, the K_d of the $\alpha 2\beta 2$ complex is approximately 0.2 μM ¹⁶. The affinity further decreases in the absence of substrate and/or effector³². In addition, the complex appears tightest during active radical transfer and subsequent substrate turnover, a relatively fast process⁹.

To this point, several studies have shown that perturbing radical transfer along the PCET pathway tends to lead to longer-lived $\alpha 2\beta 2$ complexes^{9,33}. Strategies have included substituting radical-pathway residues with unnatural analogs with highly perturbed reduction potentials^{8,9,34-37} and using substrate analogs such as N_3NDPs that cannot undergo proper turnover in the active site^{26,30,38,39}.

Here, we describe a near atomic-resolution structure of *E. coli* class Ia RNR in its active $\alpha 2\beta 2$ state, with WT- $\alpha 2$ and a doubly-substituted E52Q/(2,3,5)trifluorotyrosine122(F₃Y122)- $\beta 2$ in the presence of substrate GDP and specificity effector TTP, using cryo-EM. In a previous study, the E52Q mutation was initially pursued based on bioinformatics studies that suggested the residue was located at the $\alpha 2$ - $\beta 2$ interface and may affect complex affinity. F₃Y122 in the E52Q background resulted in trapped pathway radical (Y356•) concomitant with stoichiometric product

formation. Notably, this double-mutant construct lead to an incredibly kinetically stable $\alpha_2\beta_2$ complex ($K_d < 0.4$ nM vs 0.2 μ M for wildtype), allowing us to obtain the structure by cryo-EM^{16,33}. This is the first high-resolution structure of any active RNR, and stands to answer many outstanding questions in the field as well as to open new, exciting avenues through which we can study this incredibly complex enzyme.

2.C Results

E52Q/F₃Y-β₂ and WT-α₂ with GDP and TTP produces a complex that is stable enough for high resolution structural analysis by cryo-EM

Building on a previous study³³, we were able to identify conditions that generated an α₂β₂ complex that was stable enough for cryo-EM analysis. We used a β₂ variant wherein E52, a highly conserved residue thought to be located at the α₂-β₂ interface in the active state, was conservatively mutated to Q. This RNR variant showed complete inactivation of the enzyme³³. Intriguingly, this construct bound similarly to α₂ as wildtype-β₂ in dissociation studies. An additional substitution replacing the stable Y122• in β with an unnatural amino acid analog 2,3,5-trifluorotyrosine radical (F₃Y122•) in the E52Q background resulted in an enzyme capable of pathway-radical formation (observable Y356• in β) and a rapid generation of 0.5 equivalents of product dCDP and 0.5 equivalents of Y356• per F₃Y122•^{11,33,37}, consistent again with previous studies suggesting half-sites reactivity in RNR. We see comparable results of activity with the GDP/TTP substrate/effector pair, with a rapid burst where 0.5 equivalents of product dGDP and Y356•, per F₃Y122• is generated within the first 50-60 seconds. The observation of stoichiometric Y356• formation concomitant with dGDP formation suggests the radical is formed during reverse RT. Approximately 25% of total radical is lost during this fast phase. This fast phase is followed by a second phase where dGDP production is observed at 0.03 s⁻¹, compared to the steady state rate for the wildtype enzyme of 5-10 s⁻¹ ⁴⁰ (**Figure 2.4**). Excitingly, this double-mutant construct lead to the formation of an α₂β₂ complex that was isolable in pull-down assays up to 2 hours, a time frame well within the range amenable to structural studies.

To examine the time dependence of complex stability, negative-stain experiments were carried out in which particles were fixed and grids were prepared 15 minutes and 2 hours after initiating the reaction by addition of E52Q/F₃Y-β₂ to WT-α₂ (2:1 β₂:α₂ to maximize the reaction as there is 0.9 E52Q/F₃Y122• per β₂) in the presence of

GDP/TTP (**Figure 2.5A**). Quantification of the 2D class averages revealed that ~90% of particles were $\alpha_2\beta_2$ at the 15 minute time point but this drops to approximately ~75% at the 2 hour time point. Quantification was performed by sorting 2D class averages, where classes were identified as either $\alpha_2\beta_2$ or α_2 , which are readily distinguishable. β_2 was not readily visible given its smaller size (**Figure 2.5B**).

Using this construct, we present the first structure of any active RNR, an $\alpha_2\beta_2$ complex of *E. coli* class Ia RNR, to 3.6-Å resolution solved using cryo-electron microscopy (EM) (**Figure 2.6**). The local resolution ranges from approximately 3.3-Å resolution within the core of the protein complex to 5.5-Å or greater, such as disordered regions at the N-terminus of one of the α monomers (**Figure 2.7**). In regions of highest resolution, we observe clear cryo-EM density for structural features such as side-chains which lead to further confidence in our model (**Figure 2.8**).

The $\alpha_2\beta_2$ complex is asymmetric

Initially, crystal structures of the α_2 and β_2 subunits taken from the 3.2-Å resolution structure of $\alpha_4\beta_4$ solved in the presence of GDP/TTP²² (PDB 5CNV) were rigid-body docked into our cryo-EM density as a starting point for model building and refinement. Contrary to the two-fold symmetric complex of the docking-model with each β interacting with a different α (**Figure 2.2**), the trapped $\alpha_2\beta_2$ RNR appears structurally asymmetric, with both β subunits clearly positioned toward one α monomer (hereto referred to as α') and minimal interaction with the other α monomer (hereto referred to as α'') (**Figure 2.6**).

Previously structurally uncharacterized residues of the β subunit can be modeled

Our cryo-EM maps contain density for all residues of β_2 that were previously visualized by crystallography, i.e. the first 341 residues, as well as the last 13 residues (363-375). The position of these C-terminal residues (363-375) is consistent with that observed in

previous crystal structures of $\alpha 2$ solved in the presence of a peptide-mimic of the β C-terminal tail as well as in the structure of the $\alpha 4\beta 4$ inhibited complex^{18,22} (**Figure 2.9A**). Excitingly, we also observe very clear cryo-EM density along the $\alpha 2$ - $\beta 2$ interface that is not accounted for after docking in the crystal structures of $\alpha 2$ and $\beta 2$. This density extends from residue 341 of one β monomer (hereto referred to as β') and is continuous across the remaining residues of β' (through 375) (**Figure 2.9A**).

Guided by observable side chain density, we modeled all missing residues of β' (**Figure 2.9B**). We see that β' makes extensive interactions with α' along this previously structurally uncharacterized region involving side-chains as well as backbone amide and carboxyl moieties (**Figure 2.10**). Whereas the docking model resulted in a large cavity around the active site, remarkably, we see that β' packs in very tightly against the active site of α' , with the side chain of Q349 of β' coming within 4-5 Å of the substrate GDP (**Figure 2.9A, Figure 2.11**). P348, positioned near Y731 of α' , facilitates a sharp turn allowing for proper positioning of Y356 of β' near Y731 (**Figure 2.9A**).

The other β monomer (hereto referred to as β'') is only resolved up to residue 341 (of 375). The major difference between the $\beta 2$ structure here and previous $\beta 2$ structures is the ordering of the C-terminal tail of β' . The first 340 residues of our $\beta 2$ structure aligns well with a previous 2.05-Å resolution crystal structure of $\beta 2$ (PDB: 5CI4) with a root-mean-square deviation (RMSD) of 0.82 Å over 340 C α atoms.

PCET pathway is structurally resolved

We now have for the first time, a structural view of the entire β subunit in the active state, which allows us to model the position of Y356 in β relative to the other key residues along the PCET pathway (**Figure 2.12**). In our model, the hydroxyl of Y356 is positioned 21.5 Å away from the hydroxyl of F₃Y122 in β' , 12.1 Å from the indole ring C4 of W48 in β' , and 7.8 Å away from the hydroxyl of Y731 in α' . The total distance from the hydroxyl group of F₃Y122 in β' to the thiol group of C439 in α' is 32.6 Å.

β E52, the residue whose substitution leads to a dramatic increase in complex stability, is positioned directly at the α - β interface

We find that E52 (Q52 in this study) is positioned at the α - β interface where it is contacting N322 on loop 3 of α' (**Figure 2.13**). The amino group of the Q52 side chain is positioned 7.0 Å from the side chain hydroxyl of PCET residue Y356 and 5.2 Å from the C4 position of the indole ring of W48 in β' . Previous crystal structures of β 2 have found that E52 exists in a number of conformational states, ranging from an “out” position where the side chain is found pointing away from the diiron cluster, to an “in” position where the side chain points towards the cluster^{37,41,42}. In the “in” position, E52 is found to be involved in an extensive hydrogen-bonding network, through several water molecules and R326 in β , that extends all the way to the diiron cluster. Although the resolution of the current structure does not allow for visualization of waters, superposition of a high resolution structure of β 2 onto this structure, shows that Q52 is in the “in” position and that this side chain position could serve as a bridge between α and the previously described hydrogen-bond network that extends to the diiron site³⁷ (**Figures 2.13B,C and 2.14**).

In general, the interface between α and β is polar, consistent with the proposal that water molecules may play an important role in the PCET process at the interface⁴³. The first polar region is the one discussed above that involves Q52, R326, and Y356 of β' (**Figure 2.13C**, yellow). The second is on the other side of Y356, and includes the guanidinium group of R411- α' , a residue shown to affect the conformational flexibility of Y731- α' ⁴⁴, positioned 4-5 Å from Y356- β' , E352- β' , and Y731- α' (**Figure 2.13C**, pink). Notably, 4-5 Å distances between polar side chains are indicative of through water interactions. Lastly, Q52 is also positioned adjacent to loop 3 (residues 320-335) of both α' and α'' . Residues from the two loop 3s (E326, R331, H332 of α' and E326 of α'') and E51 from β' contribute to forming a polar channel that leads from Q52 to bulk solvent (**Figure 2.13C**, green).

The two α monomers are structurally distinct

In our structure, we observe two distinct states within the $\alpha 2$ subunit. The active site of α' has clear density for a nucleoside diphosphate (modeled here as substrate GDP), and no observable density indicative of a disulfide between C225 and C462, the two redox-active cysteines that become oxidized concomitant with turnover (**Figure 2.15A**, **Figure 2.3**). α'' has no observable density in the active site that could accommodate substrate/product, and the C225/C462 pair has corresponding cryo-EM density suggestive of a disulfide, and thus chemistry having occurred (**Figure 2.15B**). The oxidation of the C225/C462 cysteine pair is accompanied by a ~ 3 Å shift of $C\alpha$ of both C225 and C462 towards the loop containing C439 and E441, termed the Cys loop (**Figure 2.15C**). This movement mirrors that observed when comparing previous $\alpha 2$ crystal structures that either have the active site cysteines reduced²² (PDB 5CNV) or oxidized⁴⁵ (PDB 2R1R) (**Figure 2.15D**). The similarities go beyond the movement of just the two active site cysteines, suggesting there are larger order movements in the α backbone concomitant or subsequent to turnover. The RMSD over 720 $C\alpha$ atoms (residues 10-730) between α' and the reduced crystal structure of $\alpha 2$ is 0.90 Å. Likewise, the RMSD over 622 $C\alpha$ atoms (cone-domain and loop 2, discussed below, were omitted from alignment) between α'' and the oxidized $\alpha 2$ crystal structure is 1.04 Å. In contrast, the RMSD over 622 $C\alpha$ atoms between α' and α'' is 1.61 Å.

In addition, loop 2 (residues 292-301), which plays a critical role in communication between the specificity-site and the active site²², is fully ordered in substrate-bound α' , whereas it is largely disordered in α'' (**Figure 2.16**). Further, density for TTP in the specificity site corresponding to α' is better resolved than that bound in α'' . The contacts seen in α' loop 2 mirror those observed in loop 2 in the crystal structure of $\alpha 4\beta 4$ with GDP/TTP bound, consistent with our previous proposal that $\alpha 4\beta 4$'s inactivity is only a result of β being held at arm's length from α , and not due to improper substrate or specificity effectors binding²².

Our sample did not contain either of the activity effectors dATP or ATP, which bind at the N-terminal four-helix cone-domain (first ~100 residues) of the α subunit. We observe little to no density for the cone-domain associated with α'' . However, despite no evidence of bound nucleotide, the four cone-domain helices of α' appear largely ordered, possibly being structurally buttressed by regions of β' that are in close proximity (**Figure 2.17**).

C-terminus of only one β monomer interacts with the $\alpha 2$ subunit in the $\alpha 2\beta 2$ complex

In previous crystal structures of $\alpha 2$, the C-terminus of the $\beta 2$ subunit, added as a peptide, was observed along both α monomers, primarily interacting with two helices formed by residues 340-350, 710-726^{18,45}. This interaction was also observed in the crystal structures of the $\alpha 4\beta 4$ complex²². However, in the $\alpha 2\beta 2$ structure discussed here, we only observe the C-terminus of β (specifically β') along α' , whereas no density is observed in the equivalent region in α'' (**Figure 2.18**). In the crystal structure of the $\alpha 4\beta 4$ complex, the distance separating one of the last visible residues in $\beta 2$ (S341) and Q712 in α , a residue located on one of the helices that interacts with the β C-terminus, is ~52 Å (**Figure 2.19A**), indicating the C-terminus of β is able to span this distance to interact with α . In comparison, in our structure of $\alpha 2\beta 2$, the distance between S341 in β'' and Q712 in α'' is ~53 Å (**Figure 2.19B**). Given the similar distance, the observation that the C-terminus of β'' is absent along α'' may suggest that the overall structural movements that α undergoes concomitant with turnover also results in the dissociation of the β C-terminus.

C-terminus of α' interacts with β'

The crystal structure of $\alpha 2$ that was used as a starting model was structurally resolved up to residue 736 (out of 761). In α' , we observe cryo-EM density beyond residue 736 that has allowed us to model in 6 additional residues (737-742), and they appear to be leading away from the α' - $\beta 2$ interface (**Figure 2.20A**).

Interestingly, this region of α' makes additional contacts with β' . The side chain of R734 in α' forms a charge-charge interaction with the side chain of D342 in β' . Additionally, the hydroxyl groups of Y307 and Y310 in β' are within H-bonding distance of the side chain and carboxyl group of Q742 in α' , respectively (**Figure 2.20B**).

2.D Discussion

The crystal structures of the individual $\alpha 2$ and $\beta 2$ subunits from *E. coli* class Ia RNR were first solved almost three decades ago^{17,18}. Since then, additional structures of the free subunits as well as of inhibited oligomeric forms from a variety of organisms have been solved, leading to a deeper understanding of RNR activity and regulation^{21,22,45-47}. However, despite continuous efforts, an atomic-resolution structure of RNR in its active $\alpha 2\beta 2$ state has long remained elusive due to the weak and transient interaction between the subunits. As a working model, a two-fold symmetric “docking model” was proposed as the structure of the active form of the enzyme based on shape complementarity of the $\alpha 2$ and $\beta 2$ crystal structures. However, this symmetric model could not readily explain observations of half-sites reactivity in *E. coli* class Ia RNR. This half-sites reactivity is not observable under standard assay conditions^{40,48} with wildtype enzyme due to the rate-limiting conformational gating that precedes radical transfer and nucleotide reduction⁴⁰. However, studies with the mechanism-based inhibitors 2'-azido-2'-deoxynucleotides (N₃NDPs) have shown half-sites reactivity with the wildtype enzyme, where 0.5 equivalents of a unique nitrogen-centered radical (N•) is formed in the active site concomitant with the stoichiometric disappearance of Y122• in $\beta 2$ ^{28,38,49}. Spectroscopic and biochemical studies using unnatural amino acids site-specifically incorporated in place of PCET residues have also supported the half-sites reactivity model^{11,24}.

The near-atomic resolution structure of the E52Q/F₃Y- $\alpha 2\beta 2$ complex presented here represents the first high-resolution structure of any RNR in its active state. Biochemical studies of E52Q/F₃Y- $\beta 2$ and WT- $\alpha 2$ showed the reaction proceeds through an initial fast phase where approximately 0.5 equivalents of dGDP per F₃Y122• is formed concomitant with the appearance of pathway radical Y356•, again consistent with half-sites reactivity, within 50-60 seconds of initiating the reaction (**Figure 2.4**). Informed by these data, the reaction was allowed to incubate at ambient temperature for 1 minute before the cryo-EM grids were plunged. This construct's ability to form product and

pathway radical in a kinetically competent manner furthered our confidence that what we present is indeed an active $\alpha_2\beta_2$ complex. In support of prior evidence for half-sites reactivity, our structure shows that the $\alpha_2\beta_2$ complex is clearly asymmetric, with the α_2 - β_2 interface formed primarily between α' and β_2 . This asymmetry functions as a physical barrier that precludes the simultaneous formation of two radical translocation pathways.

The highest-resolution region of our model is found within the core of the complex, including at the α' - β_2 interface, suggesting that the state we have trapped is relatively rigid and homogeneous. Most importantly, the resolution of the cryo-EM density in this region allowed us to model all previously structurally uncharacterized residues of one β monomer (β') including Y356, which lead to the first structural visualization of the entire PCET pathway. In our structure, Y731 and Y730 in α' are stacked, observed in some previous structures of α_2 ^{18,22,45}, and suggested to be the case in the active $\alpha_2\beta_2$ complex via spectroscopic studies⁵⁰. Further, the distances we observe between key residues of the pathway agree closely with those previously measured spectroscopically using PELDOR²⁴. Interestingly, the overall distance from Y122 to C439 of ~35 Å predicted by the docking model is fairly close to our structurally observed distance of 32-33 Å.

We next looked to see if our structure could lend insight to the role of E52 (Q52 in this study). As noted previously, the regions surrounding E/Q52 are very polar (**Figure 2.13C**) and we suspect could accommodate waters, although the resolution of our model does not allow us to visualize them. This polar environment is consistent with prior spectroscopic studies that hypothesized the existence of a water-mediated H-bonding network at the α_2 - β_2 interface that could play an active role in PCET⁴³. Our structure shows that E52 is located directly at the subunit interface and we speculate that its protonation during the course of PCET, possibly indirectly through water, may affect the affinity between α_2 and β_2 during radical transfer (RT). The substitution of Q

for E may mimic this protonated state of E52, contributing to the higher affinity between $\alpha 2$ and $\beta 2$ observed in the complex studied here.

With the structural visualization of the RT pathway, we can start to think about the process by which this pathway is assembled and disassembled through β 's interaction with α . This process must be highly regulated to prevent both radical damage to the enzyme and an imbalance in the ratio of RNR's four deoxyribonucleotide products. Only when the correct ribonucleotide substrate is bound in the RNR active site should RT be initiated. Previous studies had shown that the binding of a cognate substrate/allosteric effector pair to α (i.e. CDP/dATP, UDP/dATP, GDP/TTP, ADP/dGTP) enhances the $\alpha 2$ - $\beta 2$ interaction^{32,36}, providing a means to ensure that β is only positioned for RT when α is in a catalytically-ready state. However, the molecular basis for this enhanced affinity has been an open question.

Our lab showed previously how the binding of allosteric specificity effectors dATP, TTP, and dGTP alter loop 2 of *E. coli* class Ia RNR to specifically recognize their cognate substrates, properly positioning their substrates into the active site and readying them for catalysis. The same recognition mode for GDP/TPP is observed in this cryo-EM RNR structure as was described earlier²² (**Figure 2.16**), but importantly, we can now see these observed active site rearrangements in the context of β binding. Remarkably, we find that it is the proper positioning of substrate by loop 2 residues that actually creates a favorable binding pocket for β' as it makes its sharp turn in the active site (**Figure 2.21**). As such, this proper binding pocket for β' only exists when substrate is bound in the manner specified by its effector through loop 2, limiting the possibility of uncoupled RT that could damage the enzyme or that non-cognate substrate will be converted to product.

We have always expected that there must exist a molecular signal to communicate that a cognate substrate/effector pair was bound to α , but are surprised to find that the signal is substrate itself. β' reaches directly into the active site and 'reads out' the

presence of an appropriately-bound substrate/effector pair. β' might sample this location in the absence of substrate but would not be expected to remain for a significant time period, which may explain its decreased affinity in the absence of substrate/effector. Additionally, with substrate bound and β' engaged, this β' loop conformation is further stabilized by α' residues 642-655, which form a β -hairpin. Previously, it was shown that this β -hairpin shifts inward in the presence of substrate^{22,45} (**Figure 2.22**). Further, we observe in our structure that in the presence of β' , the β -sheet of this hairpin extends to include residues 343-346 of β' , securing β' in position for RT (**Figure 2.21**). Interestingly, this β -hairpin is the same one that shifts-in to stabilize adenosylcobalamin binding to class II RNR⁵¹. Its conservation in class I RNRs was thought to be a vestige, but now it appears to play an analogous role but with a different radical-cofactor. Notably, with β' bound in this manner, the active site of RNR is completely sealed, with this conformation being coupled to the formation of a competent RT pathway (**Figures 2.11, 2.12, 2.21**).

This structure of an active $\alpha_2\beta_2$ also answers the question of why β must undergo such a dramatic conformational shift from one α to the other in between rounds of turnover. These structural data show us that departure of β and subsequent opening of the active site must precede or occur simultaneously with product release, since product is trapped in the active site when β is bound such that the RT pathway is intact. Notably, the structure of α'' is quite different from that of α' and their key differences provide evidence for how product release and departure of β from the active site may be facilitated by the process of turnover. Whereas α' appears to be a pre-turnover state, α'' appears to be a post-turnover state, evidenced by the observation of a disulfide between C225 and C462, the redox-active pair of cysteines that provide the reducing equivalents for nucleotide reduction. The formation of this disulfide is associated with a conformational shift of C225/462 and their respective β -strands up and towards the nucleotide binding pocket that we believe facilitates product release. Further, loop 2, despite effector TTP being bound, as well as the β -hairpin loop spanning residues 642-

655 that contacts β as described above, are both disordered in α'' , indicative of the flexibility required for β release.

In light of our new structural understanding of how β comes into such close proximity to the active site, in conjunction with biochemical observations of product release, it makes structural sense that β_2 was found interacting with the α monomer where chemistry had not occurred (α'). We believe β_2 initially interacted with α'' (with a competent PCET pathway presumably between β'' and α'') where one round of turnover occurred, and the subsequent release of deoxynucleotide product served as a physical impetus for β_2 to shift towards α' , the state observed in our structure (**Figure 2.23**).

What's puzzling however, is the fate of the radicals. The initial burst phase where we observe ~ 0.5 equivalents of dGDP formation is accompanied by a $\sim 25\%$ loss of total radical and a $\sim 75\%$ loss of $F_3Y122\bullet$ (**Figure 2.4**). We are interpreting this burst phase as the turnover that occurred between β'' and α'' . Since re-oxidation of F_3Y122 is slow relative to $Y122$ during back-electron transfer, the radical is stalled on $Y356\text{-}\beta''$ after turnover, which was shown previously^{11,33}. If β_2 migrated to α' prior to re-oxidation of F_3Y122 , we would expect to observe closer to a 50% loss of total radical, as the C-terminus of β'' , where $Y356$ is located, is completely disordered in our structure and we would thus believe the radical would be quenched. Further, the observation that 75% of $F_3Y122\bullet$ is lost during the burst phase suggests more than just “half-sites” firing. Unfortunately, the snapshot that our structure provides cannot fully explain the observed radical contents relative to the amount of product formation, which suggests single-turnover in the burst phase.

Following these questions, we need to address the apparent homogeneity in our particle set that went towards generating our final reconstruction. Although the reaction was incubated for 1 minute before freezing the grids (based on the burst phase where 0.5 equivalents of dGDP/ $Y356\bullet$ are observed), in reality the grids used for data collection were likely frozen between 1.5-3 minutes after reaction initiation based on the time it

takes to run through one plunge cycle on the Vitrobot plunger. In this time frame, we observe continued loss of total radical and very slow additional turnover at 0.03 s^{-1} (**Figure 2.4**), and thus we were somewhat perplexed, albeit pleasantly, by the apparent rigidity of our structure, especially at the $\alpha 2$ - $\beta 2$ interface. Closer inspection of the selection process that went into cleaning up the particle set after 2D classification may partially explain this homogeneity. A representative subsample of the 2D classes shows that there is a range in the quality of the generated 2D classes, from classes where secondary structural features such as α -helices can be resolved, to classes that are much less well defined (**Figure 2.24**). Based on human judgement, only the particles that corresponded to the 68 most well defined 2D classes, which consisted of $\sim 80,000$ particles, were included in subsequent processing. We suspect 2D classes of lesser quality correspond to particles of higher heterogeneity that were parsed out at this stage.

A structural question that remains unanswered regards the role of E350 β . Early studies identified its importance in catalysis⁵² and more recent studies proposed its role in gating the conformational changes that initiate radical transfer from $\beta 2$ ⁵³. Our structure proposes two potential interactions to E350 β from K154 α and S647 α (**Figure 2.10**). Notably, S647 α is located on the hairpin loop proposed to form an extended β -sheet with the newly-modeled C-terminus of β , and K154 α is located on an α -helix adjacent to this hairpin loop. However, perhaps limited by resolution, we are unable at this time to propose a structural model for how E350 β may affect conformational gating that results in initiating radical transfer.

In conclusion, the structure of the $\alpha 2\beta 2$ active complex presented here is the culmination of decades of biochemical and structural studies and provides exciting new structural insight regarding PCET and nucleotide reduction in class Ia RNR. The structure also provides new molecular detail regarding interactions at the $\alpha 2$ - $\beta 2$ interface that has implications for studying novel drug targets within the enzyme family. Lastly, we hope that this structure can serve as a launching point towards answering

other long sought-after questions, not just of the underlying chemistry, but also of the conformational dynamics that we know play such a key role in RNR regulation and activity.

2.E Materials and Methods

Protein preparation

$\alpha 2$ and E52Q/F₃Y- $\beta 2$ were prepared as described, respectively³³, and were provided by Qinghui Lin and Dr. Alex Taguchi of the Stubbe lab. The concentrations of $\alpha 2$ and E52Q/F₃Y- $\beta 2$ were determined using their respective extinction coefficients (A₂₈₀) of 189 and 131 mM⁻¹cm⁻¹, respectively. All concentrations are for the respective dimers. $\alpha 2$ had a specific activity for the GDP/TTP pair of ~1500 nmol/min/mg as determined by a coupled spectrophotometric assay⁴⁰. E52Q/F₃Y- $\beta 2$ is active under single-turnover conditions and has a radical content of 0.9 radical/dimer³³.

Negative-stain grid preparation and data collection

A reaction mixture was prepared with 5 μ M $\alpha 2$, 10 μ M E52Q-(2,3,5)F₃Y- $\beta 2$, 1 mM GDP, and 0.2 mM TTP in assay buffer (50 mM HEPES, pH 7.6, 15 mM MgSO₄, and 1 mM EDTA) where $\beta 2$ was added last to initiate the reaction. The mixture was incubated 3 min at 25°C and then diluted 130-fold in assay buffer containing 1 mM GDP and 0.2 mM TTP giving final protein concentrations of 40 nM $\alpha 2$ and 80 nM E52Q-(2,3,5)F₃Y- $\beta 2$. The solution was applied to a 300 mesh continuous carbon grid (EMS) and stained three times with a 1% uranyl acetate solution. The total time between reaction initiation and application onto the grid was approximately 15 minutes and 2 hours. All images were collected at the W.M. Keck Institute for Cellular Visualization at Brandeis University. The grids were imaged at 200 kV on a Tecnai F20 electron microscope (FEI) equipped with an UltraScan 4000 CCD camera (Gatan) using SerialEM⁵⁴ at a magnification of 62,000x with a pixel size of 1.79 Å at the specimen level. 146 micrographs of the 15 minute time-point and 137 micrographs of the 2 hr time-point were recorded.

2D classification of negative-stain data

All processing of negative-stain data was performed using Relion 1.4⁵⁵. 200 particles were identified manually and 2D classification was performed to generate 4 templates that were then used for automatic particle picking on each dataset. The total particle set identified by automated particle-picking was subjected to an additional round a 2D classification, after which classes that could not be identified as either $\alpha 2$ or $\alpha 2\beta 2$ were discarded. The percentage of $\alpha 2\beta 2$ was determined from the subset of particles that were identified as either $\alpha 2$ or $\alpha 2\beta 2$, which were identifiable by eye after classification.

Cryo-EM grid optimization

In our case, moving from negative-stain to cryo-EM resulted in severe aggregation of protein on the grid. Our initial hypothesis was that the harsh environment at the air-water interface was causing the aggregation. We screened conditions with Triton X-100 and dodecylmaltoside, two commonly used surfactants^{56,57}, at concentrations below their respective critical micelle concentrations, which did not improve grid quality. We next screened a range of salts including NaCl, KCl, and NaAcetate from 25-250 mM. The presence of NaAcetate appeared to make the most difference in alleviating aggregation and 25 mM was added to the final condition. A recent publication discusses the broader aspects of cryo-EM sample optimization⁵⁸. General strategies and lessons learned from experience are detailed in **Appendix A**.

Cryo-EM grid preparation used for data collection

Grids were prepared on Quantifoil 1.2-1.3 Cu 300 mesh holey-carbon grids and plunged on a Thermo Fisher Scientific Vitrobot (Mk IV) cryo-plunger. The final protein solution contained 0.8 μM $\alpha 2$, 1.6 μM $\beta 2$, 0.2 mM TTP, 1 mM GDP, 50 mM HEPES, 15 mM MgSO_4 , 1 mM EDTA, 25 mM NaAcetate, pH 7.6. $\alpha 2$ was incubated with nucleotides for 1 minute at RT before reaction initiation with $\beta 2$. The purpose of the NaAcetate was to prevent excessive aggregation. The final solution was incubated for an additional 1 min

before plunging. Grids were glow-discharged at -15 mA for 1 minute before protein solution was applied. 3.2 uL sample was applied to the grids that were blotted for 4.5-5 seconds (Whatman filter paper #1) before plunging into liquid ethane and transferring to storage grids. The temperature and humidity inside the Vitrobot chamber were set to 10°C and 90%, respectively.

Data collection of cryo-EM data

Data were collected at the Cryo-EM Core Facility at the University of Massachusetts Medical School at Worcester on a Thermo Fisher Titan Krios 300 kV electron microscope equipped with a Gatan GIF K2 camera across two collections. Both collections had identical collection parameters. Parameters were as follows: 1.05 Å/pix (collected at super-resolution of 0.529 Å/pix), 30 frames, 1.57 e⁻/Å²/frame dose, defocus range 1.3-2.8 um. The two data sets contained 3926 and 2312 movies, respectively. These parameters are summarized in **Table II.1**.

Frame alignment, defocus estimation, and micrograph assessment in SPHIRE

Individual frames of each dose-fractionated exposure were aligned and summed using motion_corr2⁵⁹, and the defocus of the summed frames were estimated using CTER⁶⁰. The outputs of the motion_corr2 and CTER were used to perform CTF and drift assessments within the SPHIRE software suite⁶¹. The overall average drift after discarding outliers was 5.92 Å total, and the defocus cut-off was set to 3.58 um. Based on these criteria, the two data sets containing 3926 and 2312 movies were truncated to 2946 and 2116 movies, respectively, for a total of 5062 micrographs used for selection moving forward.

Particle selection

An initial set of ~2000 particles were manually picked from a subset of aligned movies. These model particles were then used to train a neural-net automated particle picker

Topaz⁶², which was then used to automatically pick particles from the entire data set using a threshold of -2 for the cut-off for positive signal, which resulted in 200220 initial particle hits.

Frame alignment and defocus estimation in Relion 3.0

Frame alignment was rerun using Relion's implementation of motion_corr2 within the Relion 3.0 software suite⁶³. CTF estimation was also rerun using the output from Relion's motion_corr2 using ctffind4⁶⁴.

Map generation and refinement in Relion 3.0

The coordinate set of 200220 particles from Topaz was used to re-extract particles and perform initial 2D classification of 1000 classes. From these, 68 total classes, comprising 80386 particles were chosen for further analysis. These 68 classes were used to generate the initial reference-free 3D model followed by high-resolution 3D refinement using the entire particle set. CTF refinement was performed using CTF parameter fitting and per-particle defocus fitting. Particle polishing was performed using the Bayesian method of particle motion estimation. The refined particle set was used to rerun high-resolution 3D refinement to generate the final map. The final resolution at FSC=0.143 was 3.6 Å and local resolution was estimated using the ResMap (1.1.4)⁶⁵ executable within the Relion 3.0 GUI.

Model building and refinement

Coordinates from the crystal structure of inhibited class Ia RNR from *E. coli* (PDB 5CNV) were docked into the EM reconstruction using UCSF ChimeraX and used as the starting model^{22,66}. Iterative rounds of model building and refinement were done using COOT⁶⁷ and Phenix Real Space Refine⁶⁸, respectively. For real space refinement, resolution was set to 3.2 Å, and electron scattering table was selected. Model quality was evaluated using Molprobit⁶⁹ and EMRinger⁷⁰. The final model fits the map well and

contains residues 1-736 (of 761) of α chain A, 5-742 (of 761) of α chain B, 1-341 (of 375) β chain D, and 1-375 (of 375) β chain F. Figures of the model and map were generated using UCSF ChimeraX. COOT, Phenix, and ChimeraX were licensed through the SBGrid Consortium⁷¹ operated out of Harvard Medical School. Refinement and model statistics are summarized in **Table II.2**.

2.F References

- 1 Nordlund, P. & Reichard, P. Ribonucleotide reductases. *Annu Rev Biochem* **75**, 681-706, doi:10.1146/annurev.biochem.75.103004.142443 (2006).
- 2 Brown, N. C. & Reichard, P. Role of effector binding in allosteric control of ribonucleoside diphosphate reductase. *J Mol Biol* **46**, 39-55 (1969).
- 3 Reichard, P. Ribonucleotide reductases: substrate specificity by allostery. *Biochem Biophys Res Commun* **396**, 19-23, doi:10.1016/j.bbrc.2010.02.108 (2010).
- 4 Hofer, A., Crona, M., Logan, D. T. & Sjöberg, B. M. DNA building blocks: keeping control of manufacture. *Crit Rev Biochem Mol Biol* **47**, 50-63, doi:10.3109/10409238.2011.630372 (2012).
- 5 Cotruvo, J. A. & Stubbe, J. Class I ribonucleotide reductases: metallocofactor assembly and repair in vitro and in vivo. *Annu Rev Biochem* **80**, 733-767, doi:10.1146/annurev-biochem-061408-095817 (2011).
- 6 Worsdorfer, B. *et al.* Function of the diiron cluster of Escherichia coli class Ia ribonucleotide reductase in proton-coupled electron transfer. *J Am Chem Soc* **135**, 8585-8593, doi:10.1021/ja401342s (2013).
- 7 Stubbe, J., Nocera, D. G., Yee, C. S. & Chang, M. C. Radical initiation in the class I ribonucleotide reductase: long-range proton-coupled electron transfer? *Chem Rev* **103**, 2167-2201, doi:10.1021/cr020421u (2003).
- 8 Yokoyama, K., Smith, A. A., Corzilius, B., Griffin, R. G. & Stubbe, J. Equilibration of tyrosyl radicals (Y356*, Y731*, Y730*) in the radical propagation pathway of the Escherichia coli class Ia ribonucleotide reductase. *J Am Chem Soc* **133**, 18420-18432, doi:10.1021/ja207455k (2011).
- 9 Minnihan, E. C. *et al.* Generation of a stable, aminotyrosyl radical-induced alpha2beta2 complex of Escherichia coli class Ia ribonucleotide reductase. *Proc Natl Acad Sci U S A* **110**, 3835-3840, doi:10.1073/pnas.1220691110 (2013).
- 10 Seyedsayamdost, M. R., Xie, J., Chan, C. T., Schultz, P. G. & Stubbe, J. Site-specific insertion of 3-aminotyrosine into subunit alpha2 of E. coli ribonucleotide reductase: direct evidence for involvement of Y730 and Y731 in radical propagation. *J Am Chem Soc* **129**, 15060-15071, doi:10.1021/ja076043y (2007).
- 11 Ravichandran, K. R., Minnihan, E. C., Wei, Y., Nocera, D. G. & Stubbe, J. Reverse Electron Transfer Completes the Catalytic Cycle in a 2,3,5-Trifluorotyrosine-Substituted Ribonucleotide Reductase. *J Am Chem Soc* **137**, 14387-14395, doi:10.1021/jacs.5b09189 (2015).
- 12 Mao, S. S. *et al.* A model for the role of multiple cysteine residues involved in ribonucleotide reduction: amazing and still confusing. *Biochemistry* **31**, 9733-9743, doi:10.1021/bi00155a029 (1992).
- 13 Aberg, A. *et al.* Evidence for two different classes of redox-active cysteines in ribonucleotide reductase of Escherichia coli. *J Biol Chem* **264**, 12249-12252 (1989).
- 14 Holmgren, A. Glutathione-dependent synthesis of deoxyribonucleotides. Purification and characterization of glutaredoxin from Escherichia coli. *J Biol Chem* **254**, 3664-3671 (1979).

- 15 Holmgren, A. Glutathione-dependent synthesis of deoxyribonucleotides. Characterization of the enzymatic mechanism of Escherichia coli glutaredoxin. *J Biol Chem* **254**, 3672-3678 (1979).
- 16 Climent, I., Sjöberg, B. M. & Huang, C. Y. Carboxyl-terminal peptides as probes for Escherichia coli ribonucleotide reductase subunit interaction: kinetic analysis of inhibition studies. *Biochemistry* **30**, 5164-5171, doi:10.1021/bi00235a008 (1991).
- 17 Nordlund, P., Sjöberg, B. M. & Eklund, H. Three-dimensional structure of the free radical protein of ribonucleotide reductase. *Nature* **345**, 593-598, doi:10.1038/345593a0 (1990).
- 18 Uhlin, U. & Eklund, H. Structure of ribonucleotide reductase protein R1. *Nature* **370**, 533-539, doi:10.1038/370533a0 (1994).
- 19 Ando, N. *et al.* Structural interconversions modulate activity of Escherichia coli ribonucleotide reductase. *Proc Natl Acad Sci U S A* **108**, 21046-21051, doi:10.1073/pnas.1112715108 (2011).
- 20 Aravind, L., Wolf, Y. I. & Koonin, E. V. The ATP-cone: an evolutionarily mobile, ATP-binding regulatory domain. *J Mol Microbiol Biotechnol* **2**, 191-194 (2000).
- 21 Zimanyi, C. M. *et al.* Tangled up in knots: structures of inactivated forms of E. coli class Ia ribonucleotide reductase. *Structure* **20**, 1374-1383, doi:10.1016/j.str.2012.05.009 (2012).
- 22 Zimanyi, C. M., Chen, P. Y., Kang, G., Funk, M. A. & Drennan, C. L. Molecular basis for allosteric specificity regulation in class Ia ribonucleotide reductase from Escherichia coli. *Elife* **5**, e07141, doi:10.7554/eLife.07141 (2016).
- 23 Brown, N. C. & Reichard, P. Ribonucleoside diphosphate reductase. Formation of active and inactive complexes of proteins B1 and B2. *J Mol Biol* **46**, 25-38 (1969).
- 24 Seyedsayamdost, M. R., Chan, C. T., Mugnaini, V., Stubbe, J. & Bennati, M. PELDOR spectroscopy with DOPA-beta2 and NH2Y-alpha2s: distance measurements between residues involved in the radical propagation pathway of E. coli ribonucleotide reductase. *J Am Chem Soc* **129**, 15748-15749, doi:10.1021/ja076459b (2007).
- 25 Seyedsayamdost, M. R. & Stubbe, J. Site-specific replacement of Y356 with 3,4-dihydroxyphenylalanine in the beta2 subunit of E. coli ribonucleotide reductase. *J Am Chem Soc* **128**, 2522-2523, doi:10.1021/ja057776q (2006).
- 26 Bennati, M. *et al.* EPR distance measurements support a model for long-range radical initiation in E. coli ribonucleotide reductase. *J Am Chem Soc* **127**, 15014-15015, doi:10.1021/ja054991y (2005).
- 27 Salowe, S. P., Ator, M. A. & Stubbe, J. Products of the inactivation of ribonucleoside diphosphate reductase from Escherichia coli with 2'-azido-2'-deoxyuridine 5'-diphosphate. *Biochemistry* **26**, 3408-3416, doi:10.1021/bi00386a024 (1987).
- 28 Salowe, S. *et al.* Alternative model for mechanism-based inhibition of Escherichia coli ribonucleotide reductase by 2'-azido-2'-deoxyuridine 5'-diphosphate. *Biochemistry* **32**, 12749-12760, doi:10.1021/bi00210a026 (1993).
- 29 Silva, D. J., Stubbe, J., Samano, V. & Robins, M. J. Gemcitabine 5'-triphosphate is a stoichiometric mechanism-based inhibitor of Lactobacillus leichmannii

- ribonucleoside triphosphate reductase: evidence for thiyl radical-mediated nucleotide radical formation. *Biochemistry* **37**, 5528-5535, doi:10.1021/bi972934e (1998).
- 30 Vanderdonk, W. A., Stubbe, J., Gerfen, G. J., Bellew, B. F. & Griffin, R. G. Epr Investigations of the Inactivation of Escherichia-Coli Ribonucleotide Reductase with 2'-Azido-2'-Deoxyuridine 5'-Diphosphate - Evidence for the Involvement of the Thiyl Radical of C225-R1. *Journal of the American Chemical Society* **117**, 8908-8916, doi:DOI 10.1021/ja00140a003 (1995).
- 31 Brignole, E. J., Ando, N., Zimanyi, C. M. & Drennan, C. L. The prototypic class Ia ribonucleotide reductase from Escherichia coli: still surprising after all these years. *Biochem Soc Trans* **40**, 523-530, doi:10.1042/BST20120081 (2012).
- 32 Seyedsayamdost, M. *Investigations of the mechanism of radical propagation in E. coli ribonucleotide reductase by site-specific incorporation of unnatural amino acids.*, Massachusetts Institute of Technology, (2007).
- 33 Lin, Q. *et al.* Glutamate 52-beta at the alpha/beta subunit interface of Escherichia coli class Ia ribonucleotide reductase is essential for conformational gating of radical transfer. *J Biol Chem* **292**, 9229-9239, doi:10.1074/jbc.M117.783092 (2017).
- 34 Yokoyama, K., Uhlin, U. & Stubbe, J. Site-specific incorporation of 3-nitrotyrosine as a probe of pKa perturbation of redox-active tyrosines in ribonucleotide reductase. *J Am Chem Soc* **132**, 8385-8397, doi:10.1021/ja101097p (2010).
- 35 Minnihan, E. C., Yokoyama, K. & Stubbe, J. Unnatural amino acids: better than the real things? *F1000 Biol Rep* **1**, 88, doi:10.3410/B1-88 (2009).
- 36 Minnihan, E. C., Seyedsayamdost, M. R., Uhlin, U. & Stubbe, J. Kinetics of radical intermediate formation and deoxynucleotide production in 3-aminotyrosine-substituted Escherichia coli ribonucleotide reductases. *J Am Chem Soc* **133**, 9430-9440, doi:10.1021/ja201640n (2011).
- 37 Oyala, P. H. *et al.* Biophysical Characterization of Fluorotyrosine Probes Site-Specifically Incorporated into Enzymes: E. coli Ribonucleotide Reductase As an Example. *J Am Chem Soc* **138**, 7951-7964, doi:10.1021/jacs.6b03605 (2016).
- 38 Fritscher, J. *et al.* Structure of the nitrogen-centered radical formed during inactivation of E. coli ribonucleotide reductase by 2'-azido-2'-deoxyuridine-5'-diphosphate: trapping of the 3'-ketonucleotide. *J Am Chem Soc* **127**, 7729-7738, doi:10.1021/ja043111x (2005).
- 39 Thelander, L. & Larsson, B. Active site of ribonucleoside diphosphate reductase from Escherichia coli. Inactivation of the enzyme by 2'-substituted ribonucleoside diphosphates. *J Biol Chem* **251**, 1398-1405 (1976).
- 40 Ge, J., Yu, G., Ator, M. A. & Stubbe, J. Pre-steady-state and steady-state kinetic analysis of E. coli class I ribonucleotide reductase. *Biochemistry* **42**, 10071-10083, doi:10.1021/bi034374r (2003).
- 41 Assarsson, M. *et al.* Restoring proper radical generation by azide binding to the iron site of the E238A mutant R2 protein of ribonucleotide reductase from Escherichia coli. *J Biol Chem* **276**, 26852-26859, doi:10.1074/jbc.M008190200 (2001).

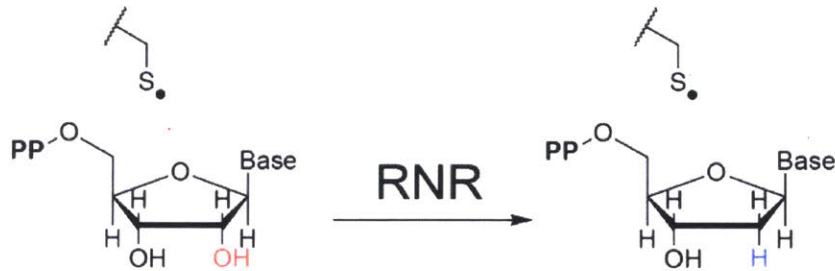
- 42 Tong, W. *et al.* Characterization of Y122F R2 of Escherichia coli ribonucleotide reductase by time-resolved physical biochemical methods and X-ray crystallography. *Biochemistry* **37**, 5840-5848, doi:10.1021/bi9728811 (1998).
- 43 Nick, T. U., Ravichandran, K. R., Stubbe, J., Kasanmascheff, M. & Bennati, M. Spectroscopic Evidence for a H Bond Network at Y356 Located at the Subunit Interface of Active E. coli Ribonucleotide Reductase. *Biochemistry* **56**, 3647-3656, doi:10.1021/acs.biochem.7b00462 (2017).
- 44 Kasanmascheff, M., Lee, W., Nick, T. U., Stubbe, J. & Bennati, M. Radical transfer in E. coli ribonucleotide reductase: a NH2Y731/R411A-alpha mutant unmasks a new conformation of the pathway residue 731. *Chem Sci* **7**, 2170-2178, doi:10.1039/c5sc03460d (2016).
- 45 Eriksson, M. *et al.* Binding of allosteric effectors to ribonucleotide reductase protein R1: reduction of active-site cysteines promotes substrate binding. *Structure* **5**, 1077-1092 (1997).
- 46 Xu, H. *et al.* Structures of eukaryotic ribonucleotide reductase I provide insights into dNTP regulation. *Proc Natl Acad Sci U S A* **103**, 4022-4027, doi:10.1073/pnas.0600443103 (2006).
- 47 Brignole, E. J. *et al.* 3.3-A resolution cryo-EM structure of human ribonucleotide reductase with substrate and allosteric regulators bound. *Elife* **7**, doi:10.7554/eLife.31502 (2018).
- 48 Steeper, J. R. & Steuart, C. D. A rapid assay for CDP reductase activity in mammalian cell extracts. *Anal Biochem* **34**, 123-130, doi:10.1016/0003-2697(70)90092-8 (1970).
- 49 Sjoberg, B. M., Graslund, A. & Eckstein, F. A substrate radical intermediate in the reaction between ribonucleotide reductase from Escherichia coli and 2'-azido-2'-deoxynucleoside diphosphates. *J Biol Chem* **258**, 8060-8067 (1983).
- 50 Nick, T. U. *et al.* Hydrogen bond network between amino acid radical intermediates on the proton-coupled electron transfer pathway of E. coli alpha2 ribonucleotide reductase. *J Am Chem Soc* **137**, 289-298, doi:10.1021/ja510513z (2015).
- 51 Sintchak, M. D., Arjara, G., Kellogg, B. A., Stubbe, J. & Drennan, C. L. The crystal structure of class II ribonucleotide reductase reveals how an allosterically regulated monomer mimics a dimer. *Nat Struct Biol* **9**, 293-300, doi:10.1038/nsb774 (2002).
- 52 Climent, I., Sjoberg, B. M. & Huang, C. Y. Site-directed mutagenesis and deletion of the carboxyl terminus of Escherichia coli ribonucleotide reductase protein R2. Effects on catalytic activity and subunit interaction. *Biochemistry* **31**, 4801-4807, doi:10.1021/bi00135a009 (1992).
- 53 Ravichandran, K. *et al.* Glutamate 350 Plays an Essential Role in Conformational Gating of Long-Range Radical Transport in Escherichia coli Class Ia Ribonucleotide Reductase. *Biochemistry* **56**, 856-868, doi:10.1021/acs.biochem.6b01145 (2017).
- 54 Mastronarde, D. N. Automated electron microscope tomography using robust prediction of specimen movements. *J Struct Biol* **152**, 36-51, doi:10.1016/j.jsb.2005.07.007 (2005).

- 55 Scheres, S. H. W. RELION: Implementation of a Bayesian approach to cryo-EM structure determination. *J Struct Biol* **180**, 519-530, doi:10.1016/j.jsb.2012.09.006 (2012).
- 56 Glaeser, R. M. & Han, B. G. Opinion: hazards faced by macromolecules when confined to thin aqueous films. *Biophys Rep* **3**, 1-7, doi:10.1007/s41048-016-0026-3 (2017).
- 57 Glaeser, R. M. *et al.* Factors that Influence the Formation and Stability of Thin, Cryo-EM Specimens. *Biophys J* **110**, 749-755, doi:10.1016/j.bpj.2015.07.050 (2016).
- 58 Drulyte, I. *et al.* Approaches to altering particle distributions in cryo-electron microscopy sample preparation. *Acta Crystallogr D Struct Biol* **74**, 560-571, doi:10.1107/S2059798318006496 (2018).
- 59 Zheng, S. Q. *et al.* MotionCor2: anisotropic correction of beam-induced motion for improved cryo-electron microscopy. *Nat Methods* **14**, 331-332, doi:10.1038/nmeth.4193 (2017).
- 60 Penczek, P. A. *et al.* CTER-rapid estimation of CTF parameters with error assessment. *Ultramicroscopy* **140**, 9-19, doi:10.1016/j.ultramic.2014.01.009 (2014).
- 61 Moriya, T. *et al.* High-resolution Single Particle Analysis from Electron Cryo-microscopy Images Using SPHIRE. *Jove-J Vis Exp*, doi:ARTN e55448 10.3791/55448 (2017).
- 62 Bepler, T. *et al.* Positive-unlabeled convolutional neural networks for particle picking in cryo-electron micrographs. *Res Comput Mol Biol* **10812**, 245-247 (2018).
- 63 Zivanov, J. *et al.* New tools for automated high-resolution cryo-EM structure determination in RELION-3. *Elife* **7**, doi:ARTN e42166 10.7554/eLife.42166 (2018).
- 64 Rohou, A. & Grigorieff, N. CTFFIND4: Fast and accurate defocus estimation from electron micrographs. *J Struct Biol* **192**, 216-221, doi:10.1016/j.jsb.2015.08.008 (2015).
- 65 Kucukelbir, A., Sigworth, F. J. & Tagare, H. D. Quantifying the local resolution of cryo-EM density maps. *Nat Methods* **11**, 63-65, doi:10.1038/nmeth.2727 (2014).
- 66 Goddard, T. D. *et al.* UCSF ChimeraX: Meeting modern challenges in visualization and analysis. *Protein Sci* **27**, 14-25, doi:10.1002/pro.3235 (2018).
- 67 Emsley, P., Lohkamp, B., Scott, W. G. & Cowtan, K. Features and development of Coot. *Acta Crystallogr D* **66**, 486-501, doi:10.1107/S0907444910007493 (2010).
- 68 Adams, P. D. *et al.* PHENIX: a comprehensive Python-based system for macromolecular structure solution. *Acta Crystallogr D* **66**, 213-221, doi:10.1107/S0907444909052925 (2010).
- 69 Williams, C. J. *et al.* MolProbity: More and better reference data for improved all-atom structure validation. *Protein Sci* **27**, 293-315, doi:10.1002/pro.3330 (2018).
- 70 Barad, B. A. *et al.* EMRinger: side chain-directed model and map validation for 3D cryo-electron microscopy. *Nat Methods* **12**, 943-946, doi:10.1038/nmeth.3541 (2015).

71 Morin, A. *et al.* Collaboration gets the most out of software. *Elife* **2**, doi:ARTN e01456
10.7554/eLife.01456 (2013).

2.F Figures and Tables

A



B

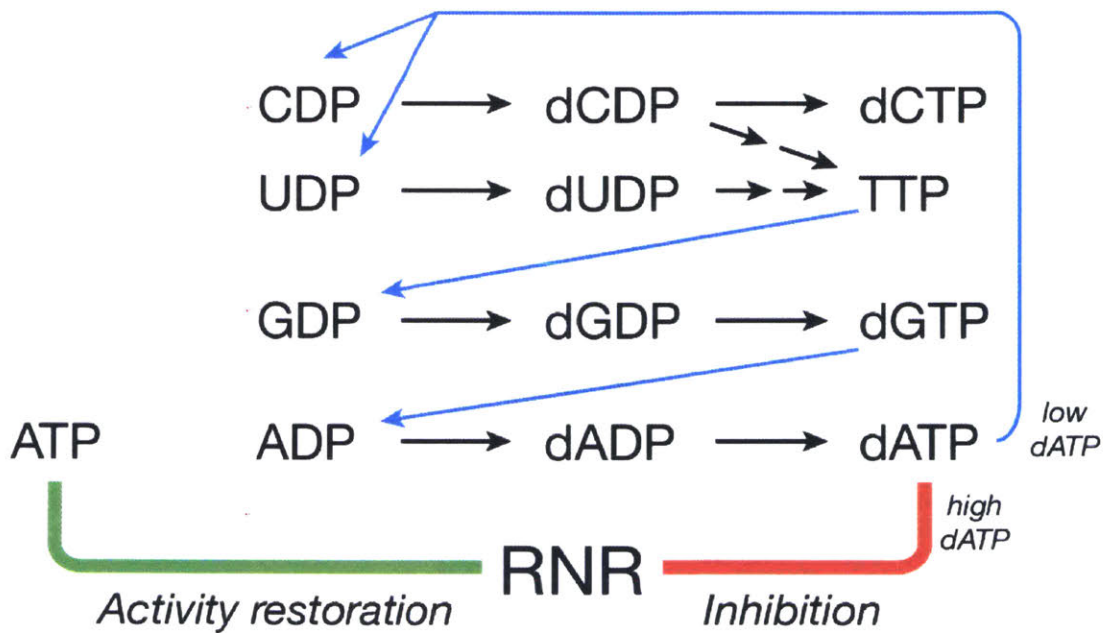


Figure 2.1: Reaction of ribonucleotide reductase. A) Class Ia RNR catalyzes the reduction of ribonucleoside diphosphates at their 2'-position to generate their deoxyribonucleotide counterparts. The reaction is initiated by a transient active-site thiyl-radical that gets regenerated after each turnover. B) Substrate specificity is regulated allosterically via the binding of deoxynucleotides. Under low concentrations of dATP, CDP and UDP reduction is favored. TTP in turn leads to GDP reduction and dGTP leads to ADP reduction. When the concentration of dATP increases, it can bind to a second allosteric site, the activity site, which inhibits enzymatic activity. ATP can compete for binding at this activity site to restore activity.

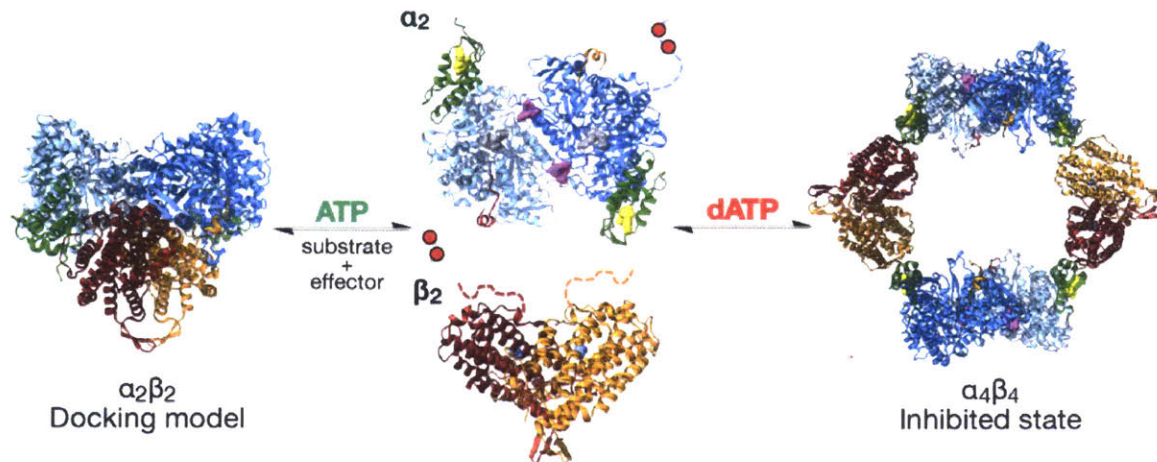


Figure 2.2: Oligomeric states of *E. coli* class Ia RNR. *E. coli* class Ia RNR is composed of two homodimeric subunits. α_2 , shown in cyan/blue/green, houses the active site (substrate shown in grey spheres) and two allosteric nucleotide-binding sites (effectors shown in yellow and purple spheres), and β_2 , shown in red/orange, houses the diferric tyrosyl radical cofactor (dark-blue spheres). dATP binding to the N-terminal cone domain of α_2 (green) generates the inhibited $\alpha_4\beta_4$ state and dATP displacement by ATP can shift the equilibrium towards the active $\alpha_2\beta_2$ state, shown above as the symmetric docking model. Both α_2 and β_2 have disordered C-terminal tails (shown as dotted lines of corresponding color) that play essential roles in catalysis. The C-terminus of α_2 has a pair of redox active cysteines (shown as red circles) that are responsible for re-reducing the disulfide that forms in the active site as a result of turnover. The position of the last ~ 15 residues of β_2 , known from previous crystal structures, are shown on α_2 in red/orange.

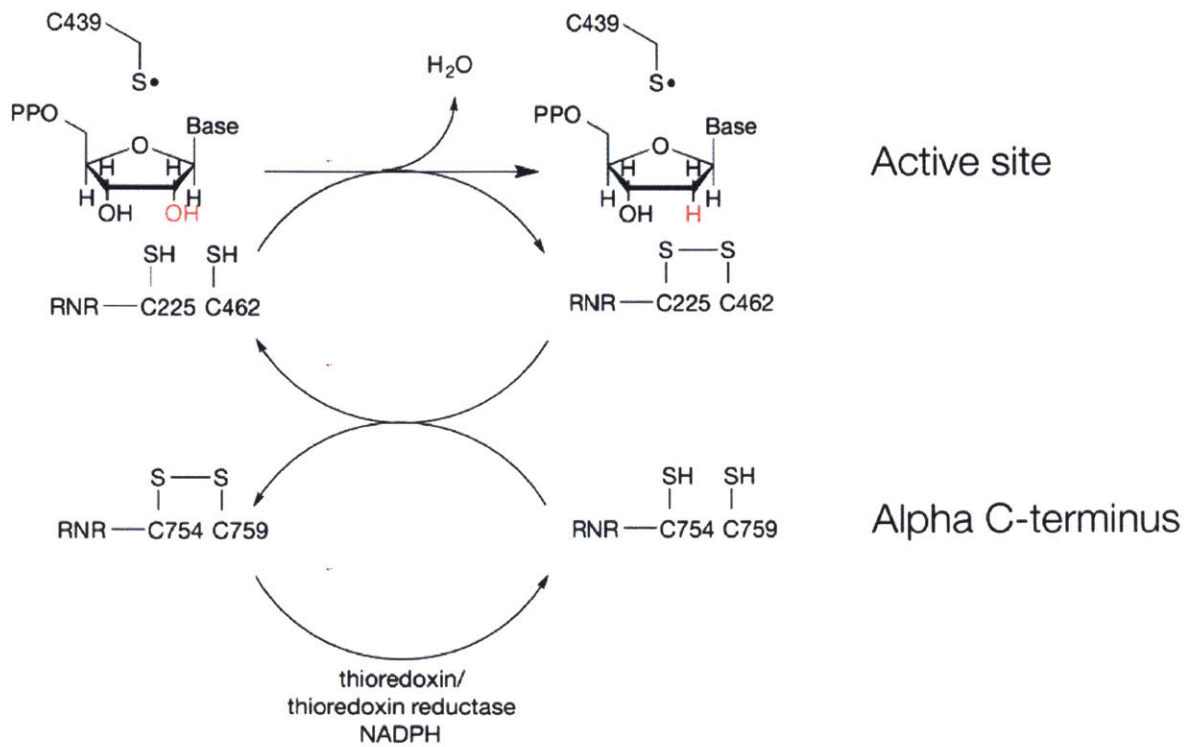


Figure 2.3: Enzymatic turnover in class Ia RNR involves a series of redox-active cysteine pairs. The reducing equivalents for nucleotide reduction is initially provided by a pair of cysteines (C225/462) in the active site that get oxidized to form a disulfide concomitant with product formation. This disulfide gets reduced by a second pair of redox-active cysteines (C754/759) found at the C-terminus of the $\alpha 2$ subunit. Ultimately, the disulfide between C754 and C759 gets reduced via the thioredoxin/thioredoxin reductase pair together with NADPH, thus allowing for additional rounds of turnover.

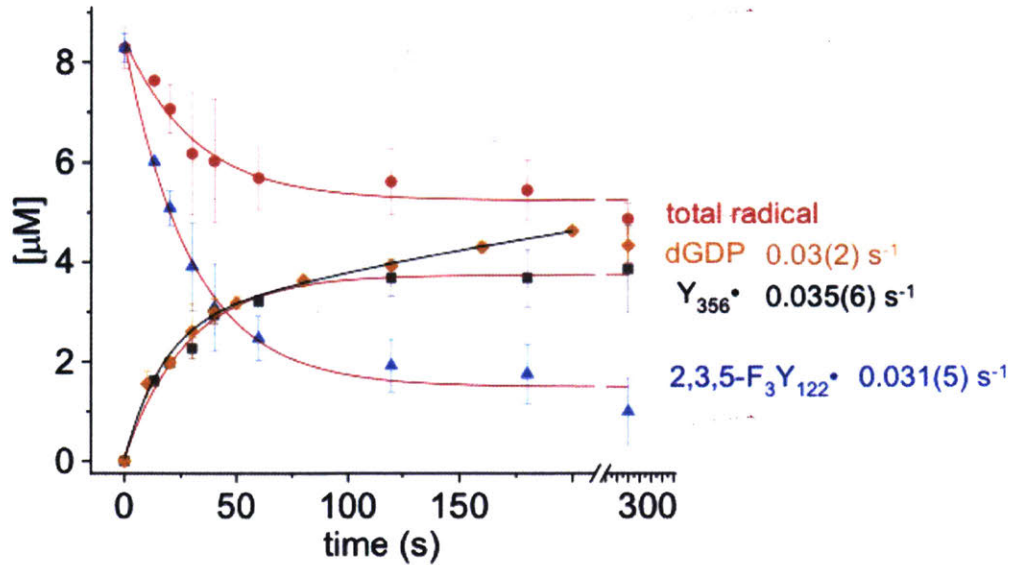
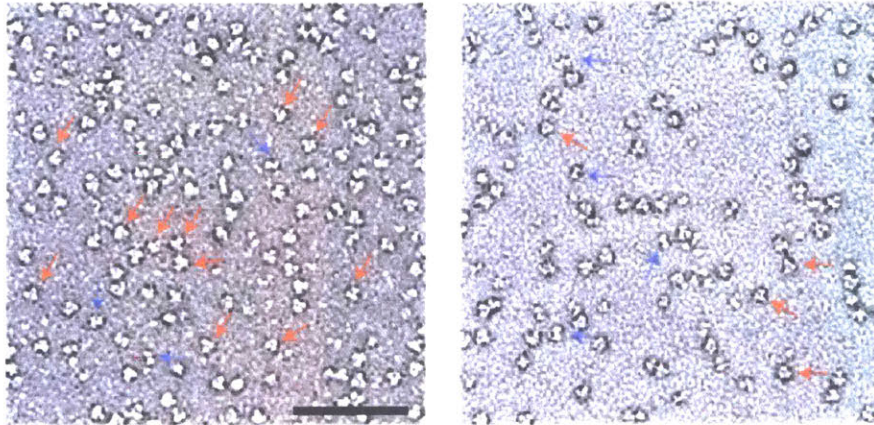


Figure 2.4: Monitoring turnover and radical content of WT- α 2 (20 μ M) and E52Q/trifluorotyrosine122(F3Y122)- β 2 (20 μ M) in the presence of substrate GDP and specificity effector TTP. A fast phase, in which we observe approximately one-half equivalents of product dGDP form, occurs within the first ~50-60 seconds following reaction initiation, followed by a slow phase where we observe continued formation of dGDP at 0.03 s^{-1} . Approximately 25% of total radical is lost during the fast phase as well as ~75% of F₃Y122•.

A

15 minutes after
reaction initiation

2 hours after
reaction initiation

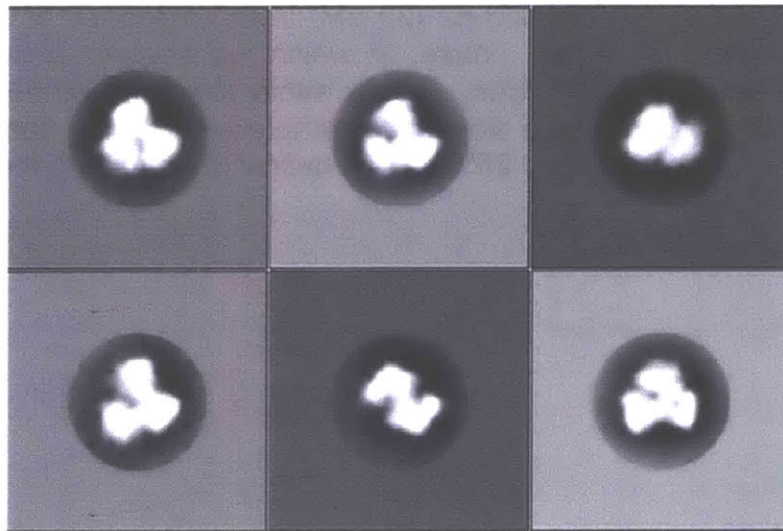
B

Figure 2.5: Time-dependence of $\alpha_2\beta_2$ complex stability examined by negative-stain EM. A) Negative stain grids prepared 15 min (left) and 2 hr (right) after reaction initiation by the addition of E52Q/F3Y122- β_2 to α_2 . Protein concentration is 13 ng/uL total protein and sample was prepared in 1 mM GDP, 0.2 mM TTP, 1x assay buffer. $\alpha_2\beta_2$ is highlighted with red arrows and α_2 is highlighted with blue arrows. Scale bar indicates 100 nm. B) Representative 2D class averages. The majority of particles were of a $\alpha_2\beta_2$ complex but a small subset were free- α_2 , easily identifiable by their canonical “S”-shape (middle, bottom row). Quantification revealed 91% of particles were $\alpha_2\beta_2$ at the 15 minute time-point and 77% were $\alpha_2\beta_2$ at the 2 hr time-point. Particles were defined as either $\alpha_2\beta_2$ or free- α_2 .

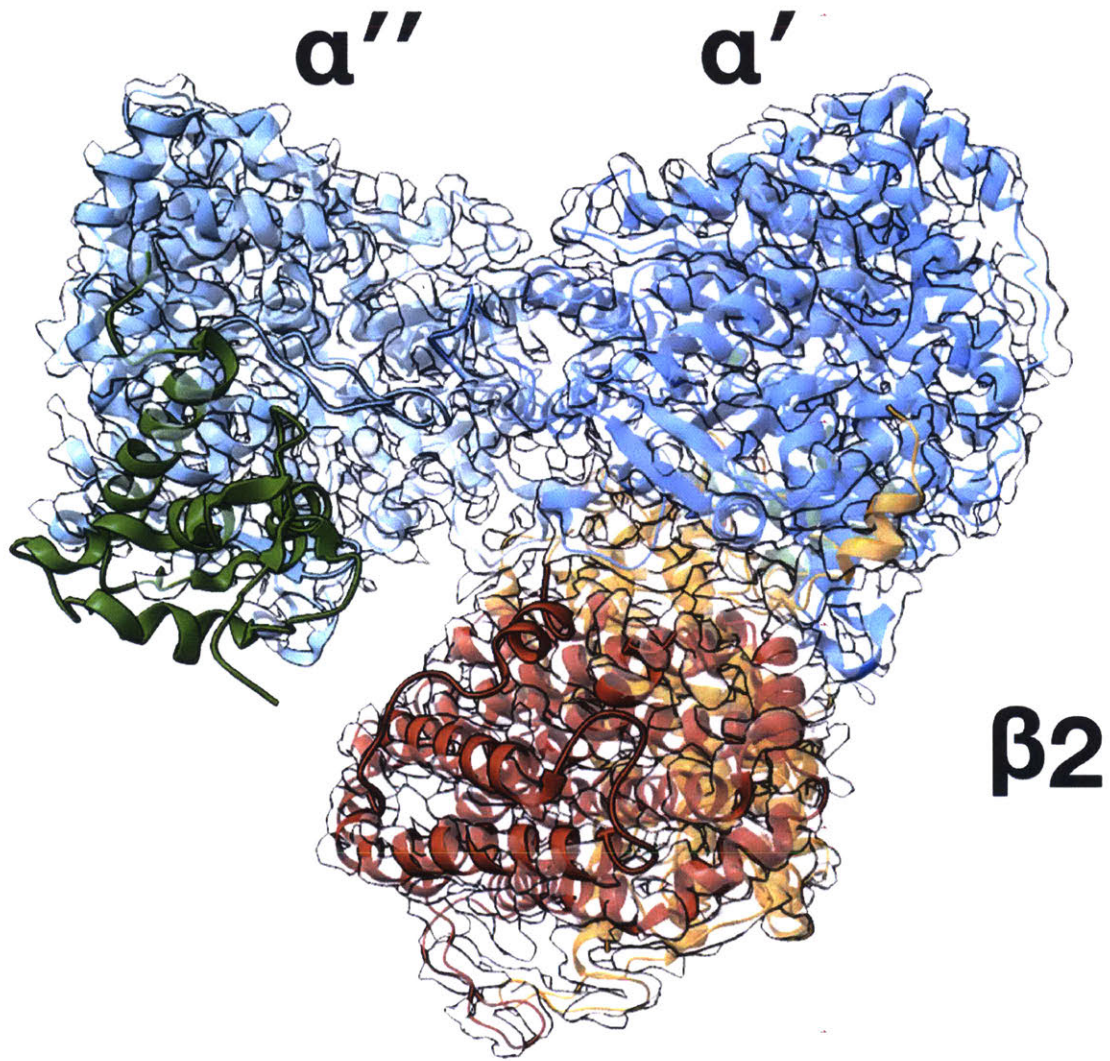


Figure 2.6: 3.6-Å resolution cryo-EM map of active *E. coli* RNR $\alpha_2\beta_2$ complex. A) The complex is asymmetric, with β_2 predominantly interacting with one α monomer (α'). Colors are as in Figure 2.2. Cryo-EM density is shown in transparent grey.

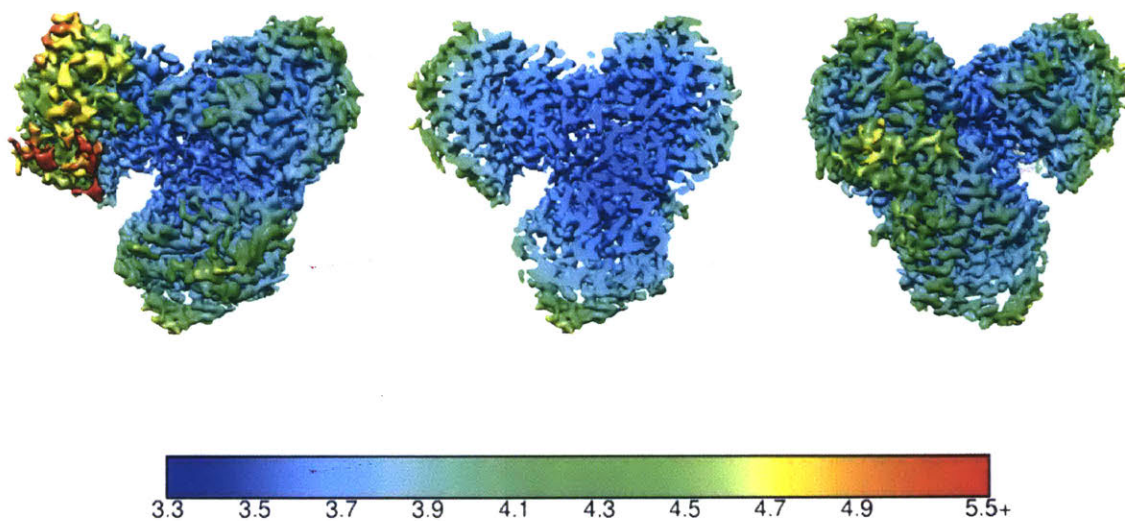


Figure 2.7: Local resolution maps of cryo-EM density. Left: Local resolution map of final 3D refinement. The resolution ranges from 3.4 Å or better within the core of the complex, including at the $\alpha 2$ - $\beta 2$ interface, to 5.5 Å or worse at the largely disordered N-terminus of one of the α monomers (α''). Middle: Cross-section view to highlight that the highest resolution region is found within the core of the complex, including the $\alpha 2$ - $\beta 2$ interface. Right: 180° rotation of the orientation shown on the far left (i.e. the backside). Resolution scale is as shown and is in Å.

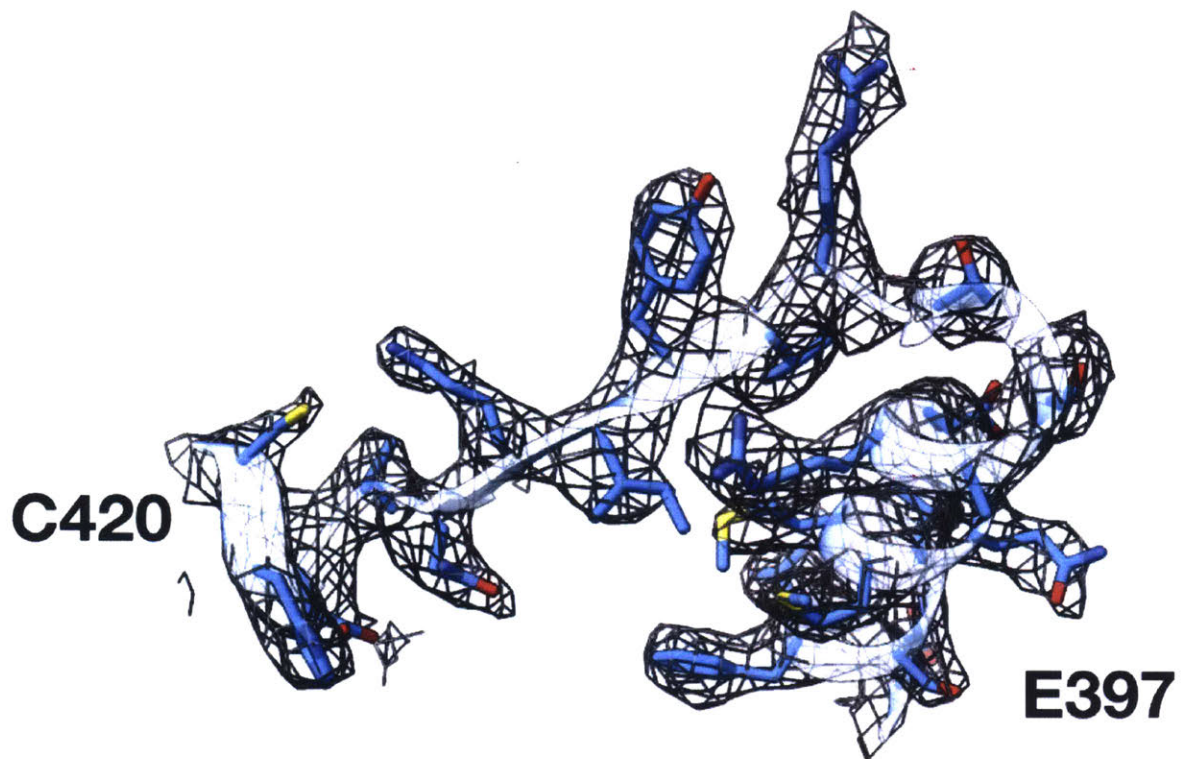


Figure 2.8: Representative cryo-EM density in region of highest resolution. Shown here are residues 397-420 in α' . Backbone atoms are shown in partially transparent ribbons.

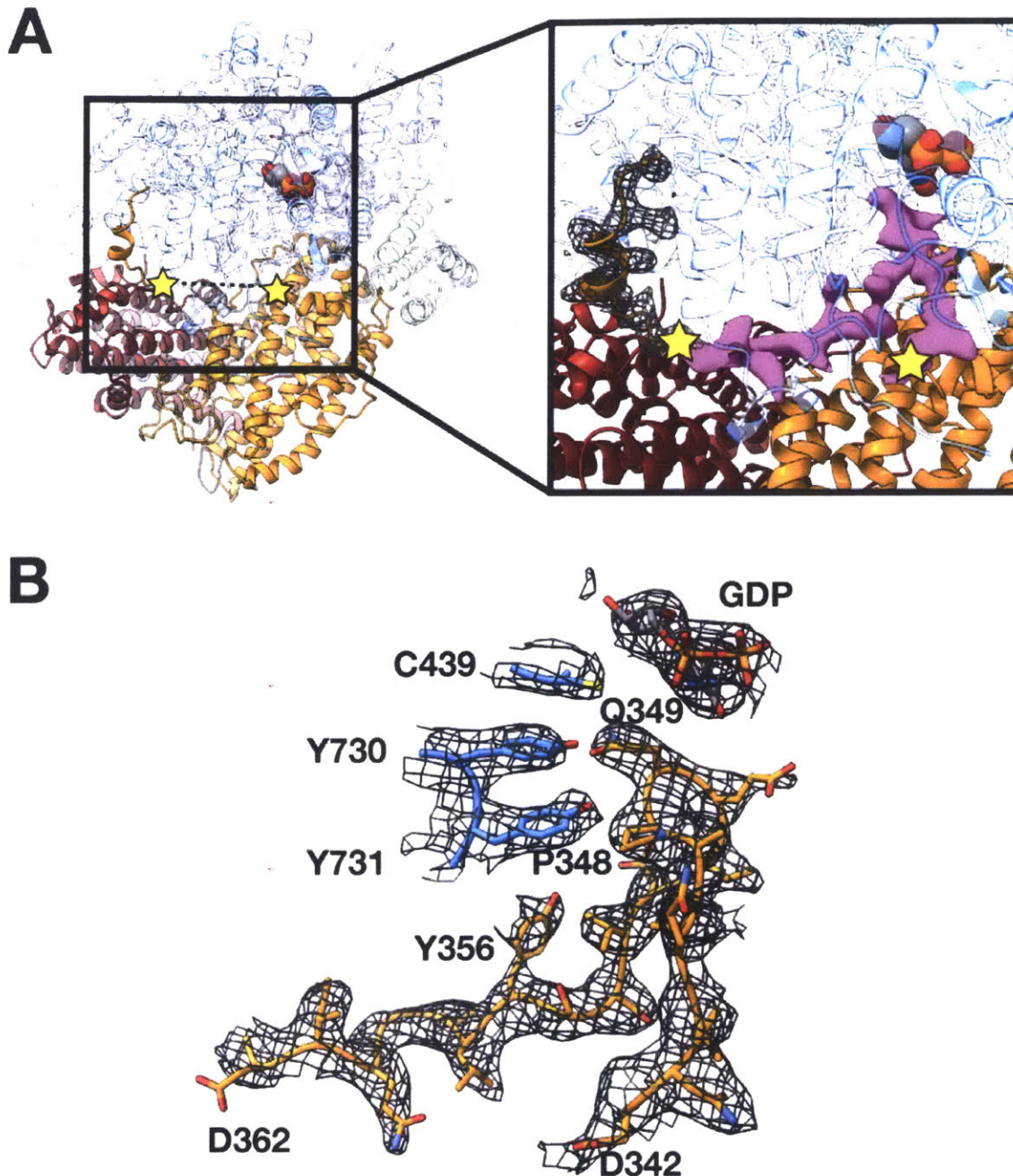


Figure 2.9: All previously structurally uncharacterized residues of beta can be modeled into cryo-EM density. A) The left and right stars indicate residues 363 and 342 of β' (orange), respectively. Colors are as in Figure 2.2, with $\alpha 2$ shown in partial transparency. Substrate GDP shown with carbons in grey spheres. Cryo-EM density corresponding to residues 342-362 of β' is shown in purple and residues 363-375 in grey mesh. B) Residues 342-362, including most side chains, can be modeled into cryo-EM density, shown in mesh. Locations of key residues are labeled for context. α' residues are shown in blue and β' residues in orange.

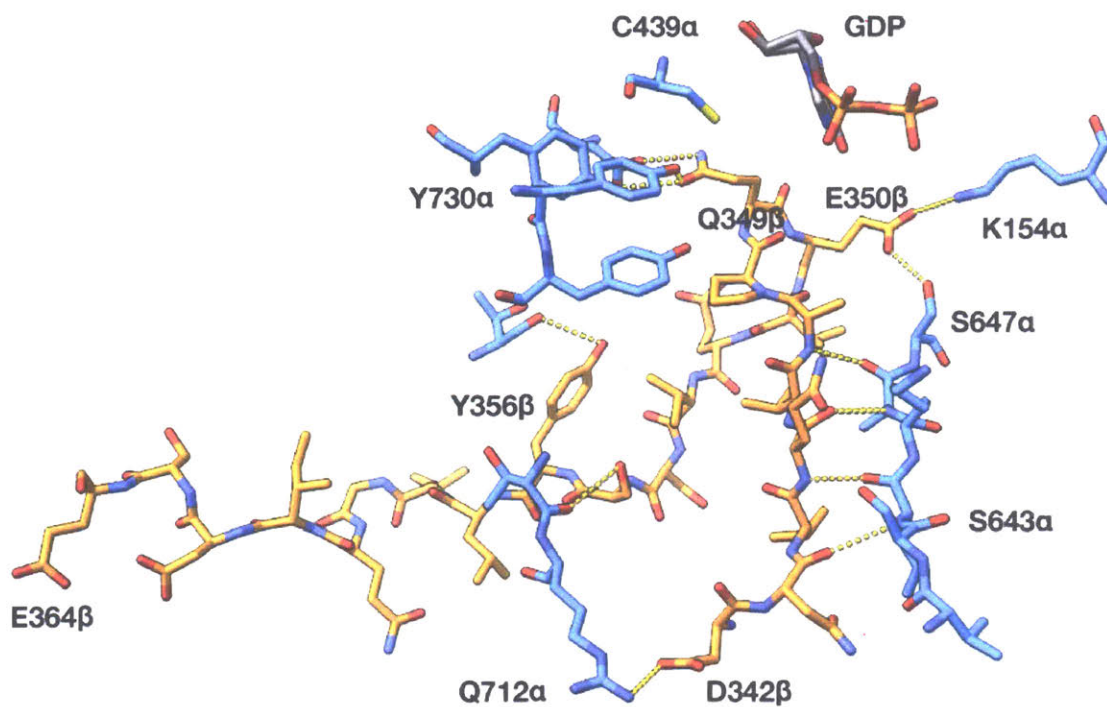
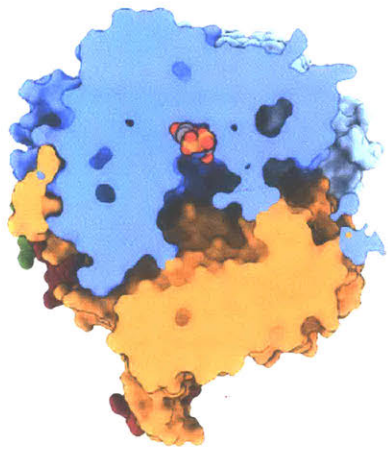
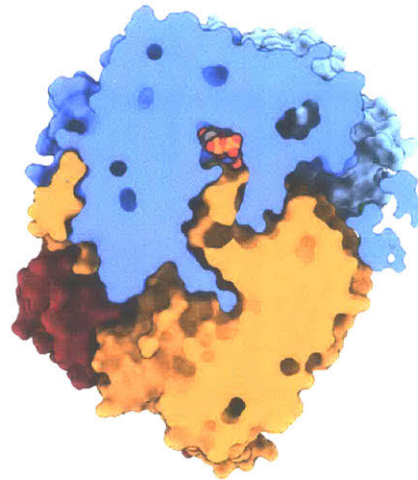


Figure 2.10: Interactions between residues 342-364 of β' and nearby residues of α' . Distances of 4 Å or less are highlighted and shown in yellow dashed lines. Key residues are labeled for context.



Docking model



Cryo-EM model

Figure 2.11: Cryo-EM model shows tight packing of active site. A surface representation of the docking model (left) reveals a large cavity around the substrate and active site. The cryo-EM model (right) shows that β' (orange) packs in very tightly into the active site of α' (blue), blocking solvent accessibility. Substrate GDP is shown in spheres.

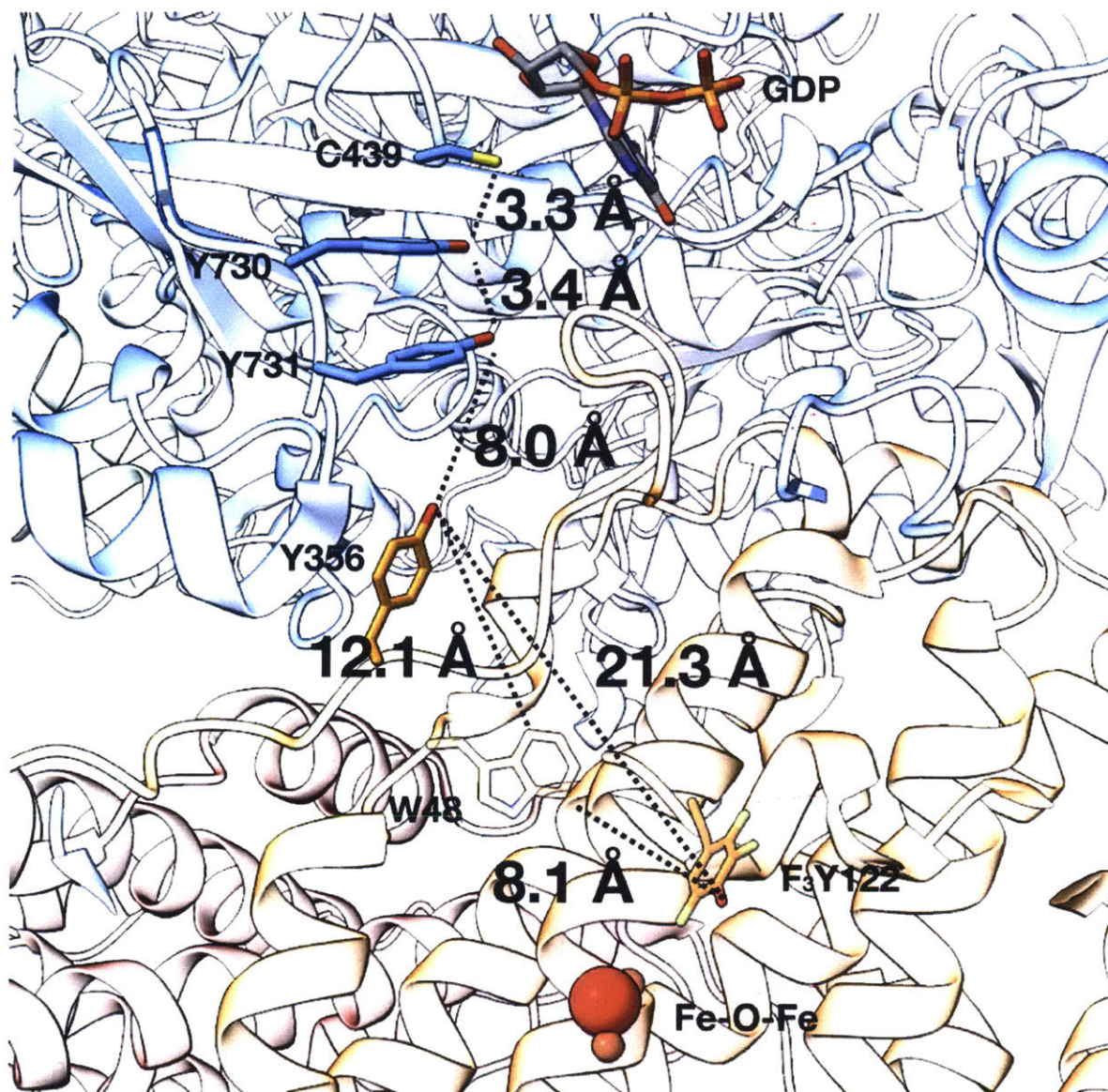


Figure 2.12: The entire PCET pathway is structurally resolved. Distances are shown between key residues in Å. W48 is shown in partial transparency due to uncertainty regarding its direct participation in PCET. The distance from F₃Y122 in β' to C439 in α' is 32.6 Å.

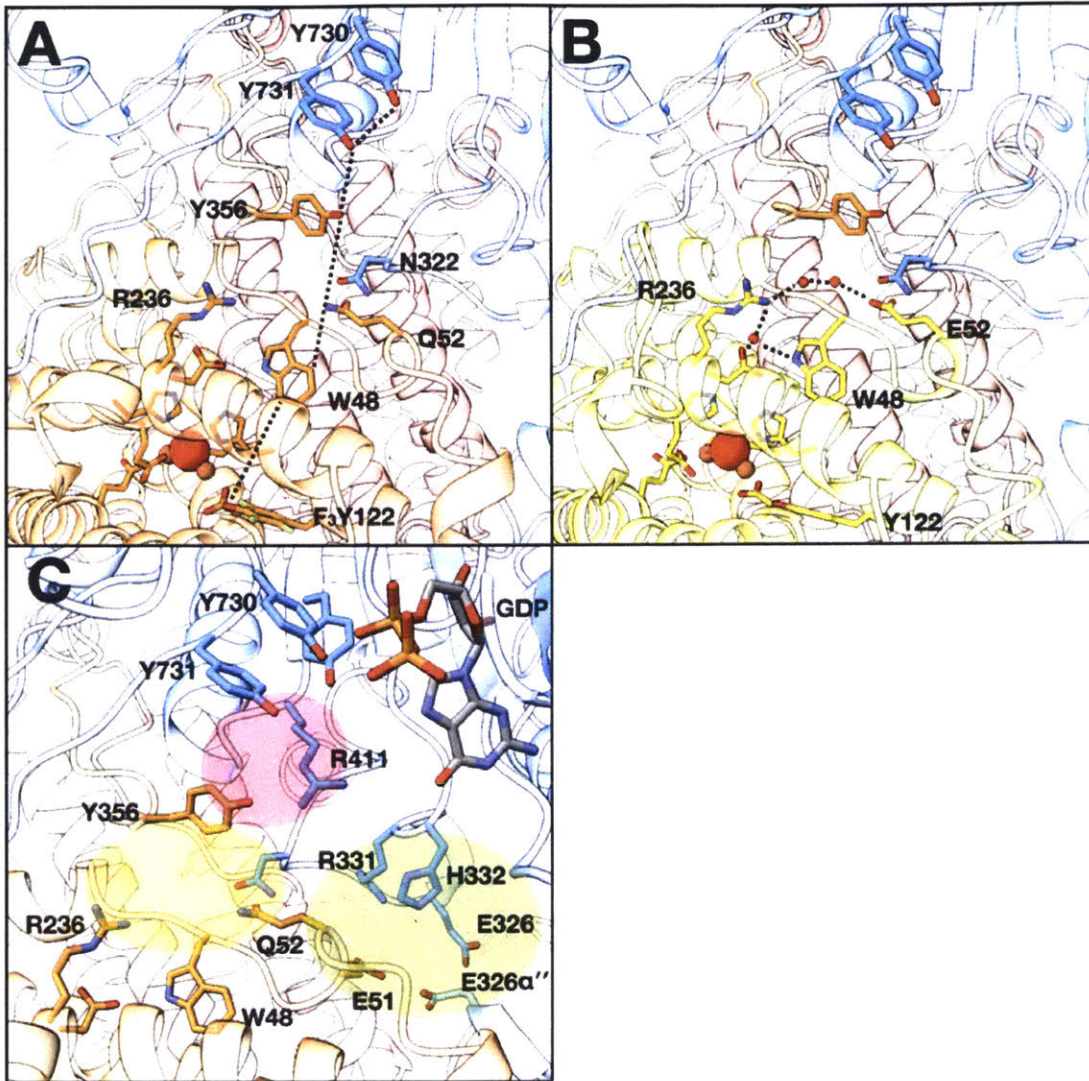


Figure 2.13: Q52 aligns with WT-E52 in the “in” position. A) The side chain of Q52 of β' interacts with the side chain of N322 on loop 3 of α' , found 2.5 Å away. As modeled, the side chain amino group of Q52 is positioned 7.0 Å from Y356 and 5.2 Å from W48 in β' . Key residues of the PCET pathway are highlighted with dashed lines for context. Colors are as in Figure 3. B) Superimposing a higher-resolution structure of WT- β (PDB 5C14), we see that key residues align well, including E52 with Q52 in our structure (Figure 2.14). E52 is involved in a putative H-bonding network that involves several waters and extends to the diiron cluster. WT- β is shown in yellow and waters are shown in red spheres. Interactions between waters and residue side chains are shown in dashed lines. C) Regions surrounding E/Q52 are very polar. In transparent yellow is shown the region with conserved waters shown in Figure 13B. In transparent pink highlights region enclosed by Y356- β' , E352- β' , Y731- α' , and R411- α' . The guanidinium group of R411 is positioned 4-5 Å from both Y356 and Y731. E352- β' not shown for clarity. In transparent green is shown a polar channel primarily formed by contributions from loop 3 (residues 320-335) on both α' and α'' .

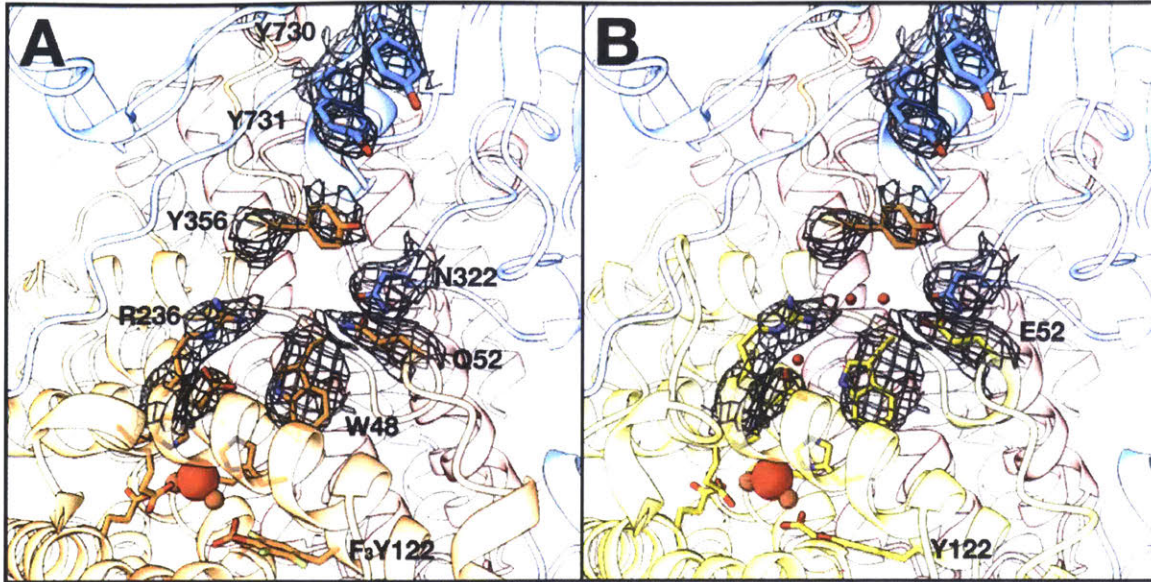


Figure 2.14: The conformation of Q52 is in the “in” position. Superposition of a 2.05-Å resolution crystal structure of $\beta 2$ with E52 found in the “in” position (PDB 5C14) with β' shows they align well within the cryo-EM density. Colors are as in Figure 2.13.

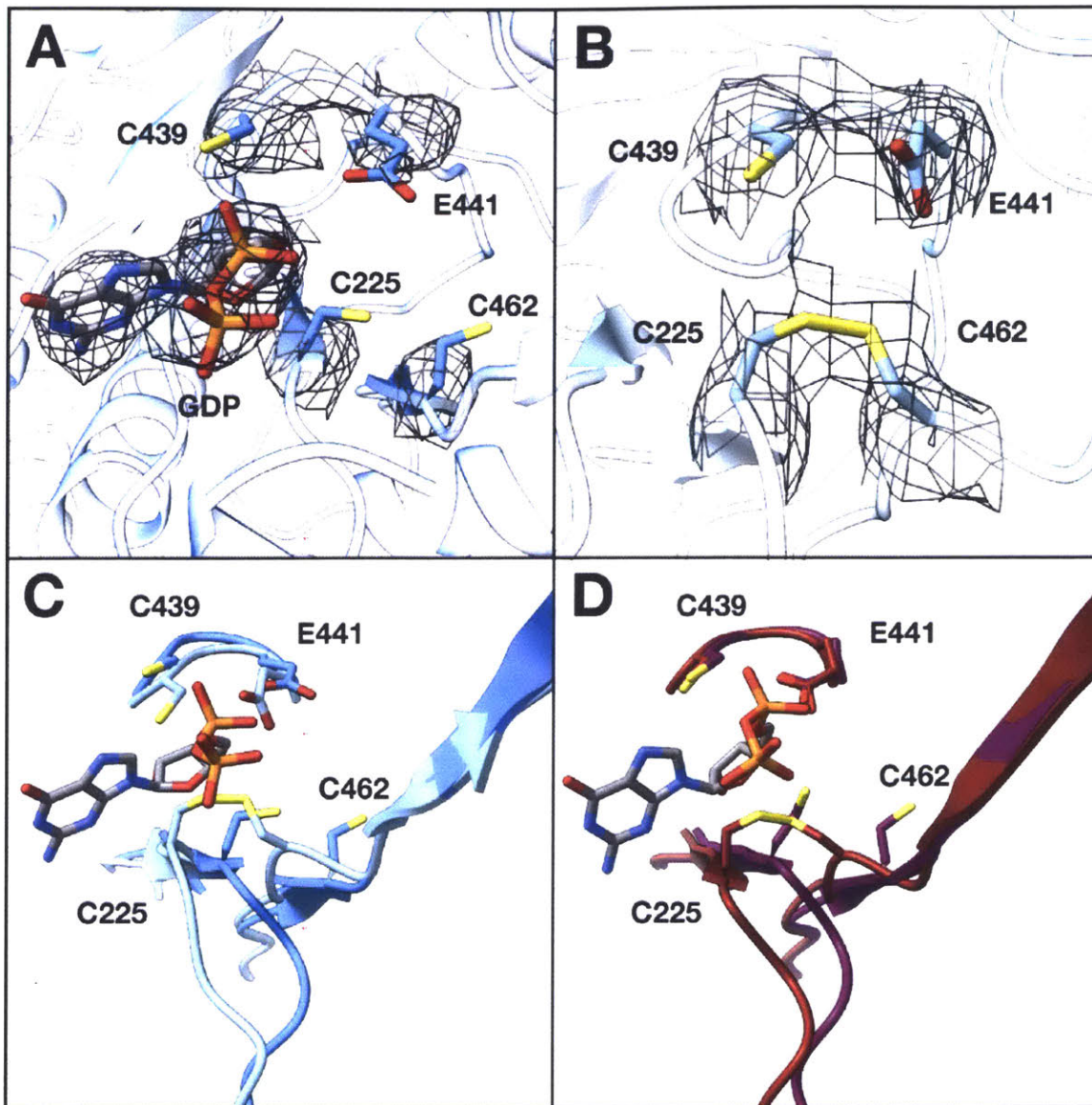


Figure 2.15: The active sites of α' and α'' are structurally different. A) In α' , we see clear density (shown in mesh) for substrate GDP, as well as no evidence of a disulfide between C225 and C462. C439 and E441, two other residues involved in turnover, are shown for context. B) The active site of α'' shows evidence of a disulfide between C225-C462, indicative of a post-turnover state. C) Overlay of active sites of α' and α'' . The formation of the disulfide is accompanied by a ~ 3 Å shift of C α of both C225 and C462 toward the loop containing C439 and E441. D) Overlay of previously reported crystal structures of α_2 with reduced (purple, PDB 5CNV) and oxidized (brown, PDB 2R1R) active sites.

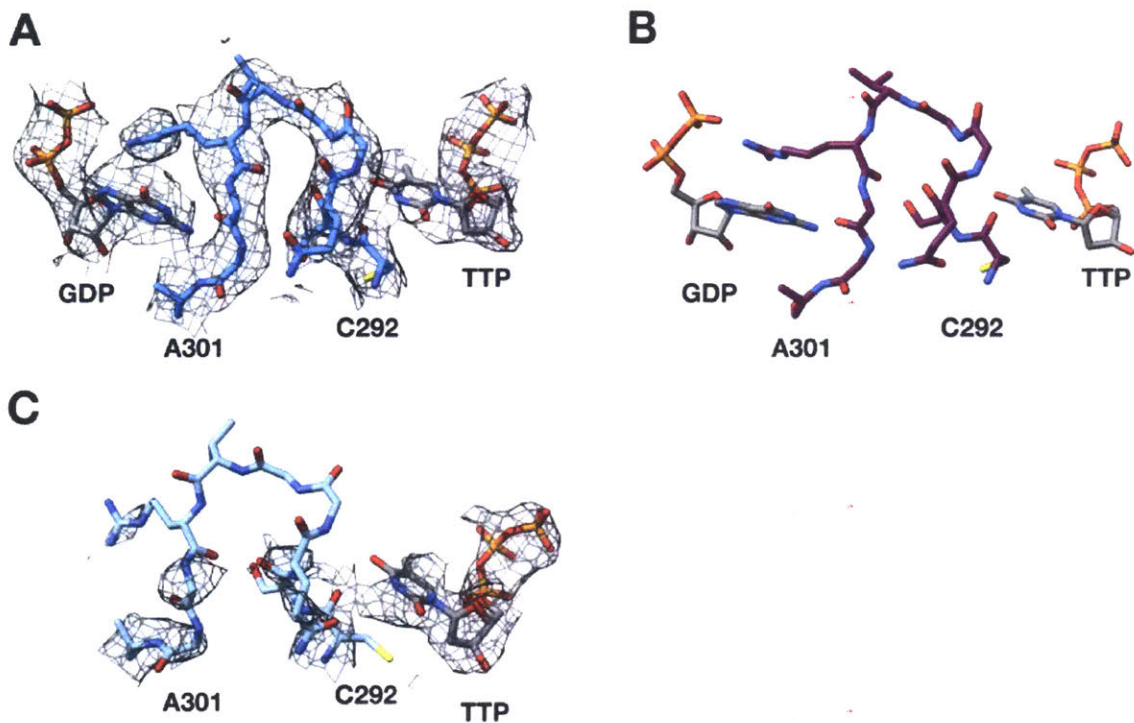


Figure 2.16: Loop 2 (residues 292-301) in α plays a key role in the communication between the specificity site and active site. A) Loop 2 in α' is fully ordered. Nucleotide carbons shown in grey and protein carbons shown in blue. B) Loop 2 in the $\alpha 4\beta 4$ crystal structure with GDP/TTP bound recapitulates contacts observed in panel A. Protein carbons shown in purple. C) Loop 2 in α'' is largely disordered. Protein carbons shown in light-blue.

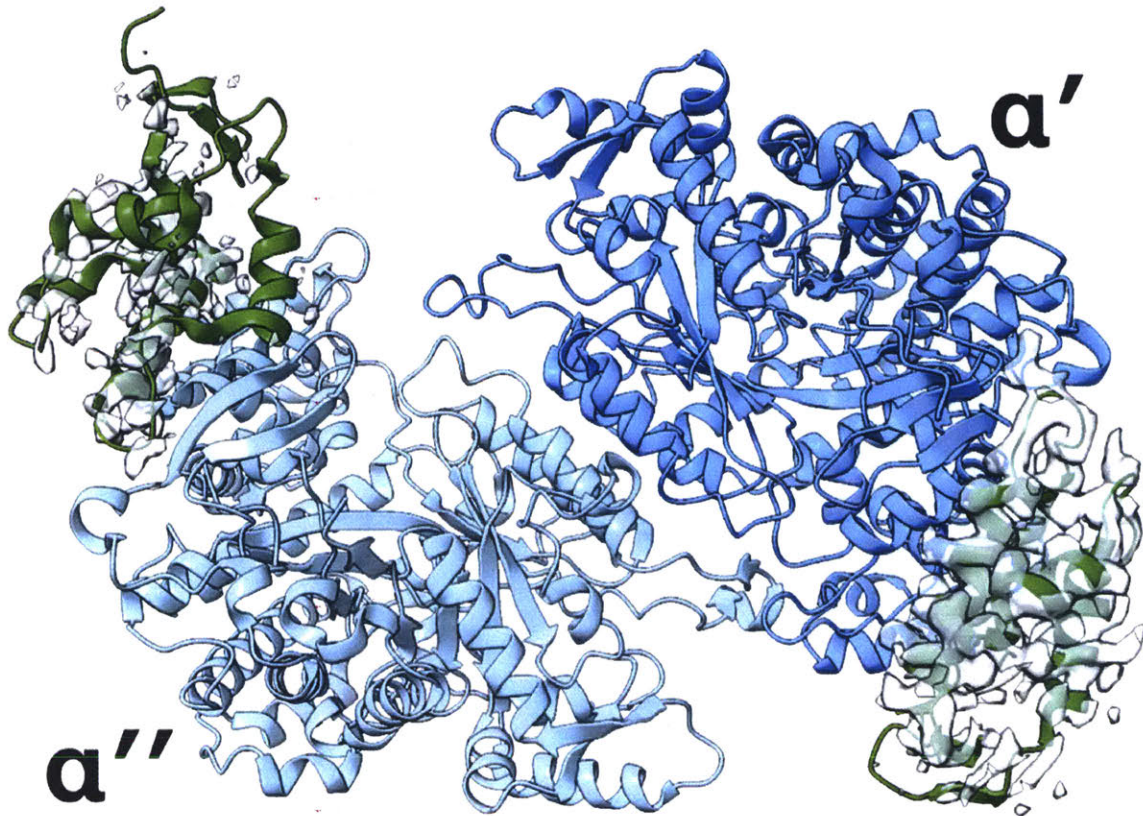


Figure 2.17: N-terminal four-helix cone domain is only ordered in one α monomer. The cone-domain (shown in green in both monomers) of α' is mostly ordered, whereas it is largely disordered in α'' . Local cryo-EM density corresponding to residues 1-100 is shown in transparent grey.

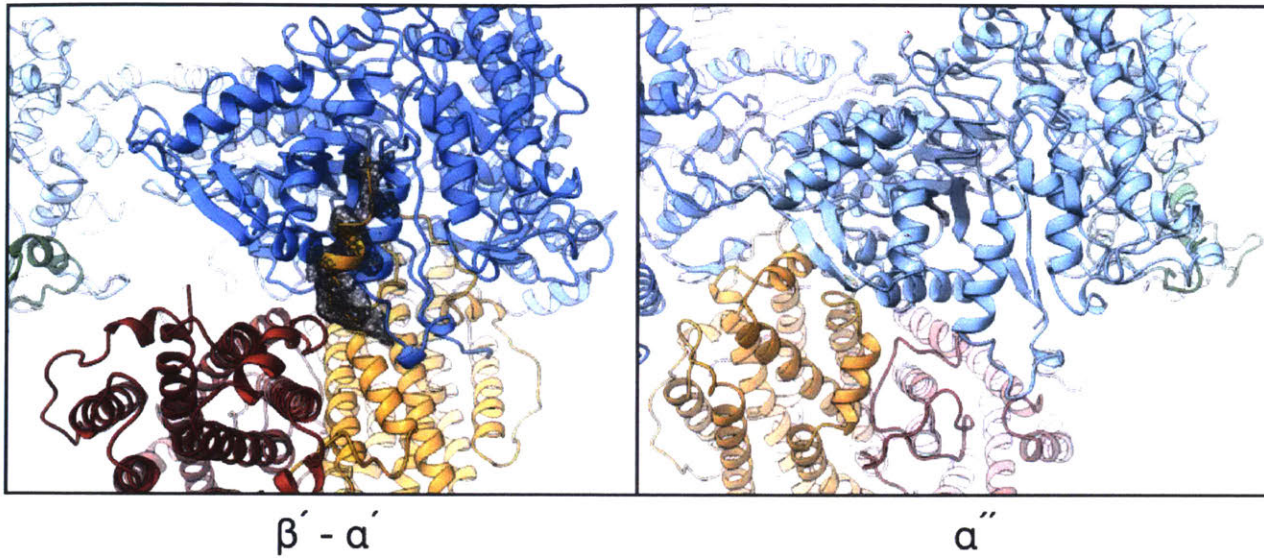


Figure 2.18: Only one C-terminus of β_2 is bound to α_2 . There is clear cryo-EM density, shown in grey mesh, showing that the C-terminus of β' interacts with α' in the same orientation as observed in previous crystal structures of both α_2 and $\alpha_4\beta_4$ (left, refs). On the other hand, we see no evidence of cryo-EM density corresponding to the C-terminus of β'' in the equivalent location along α'' (right).

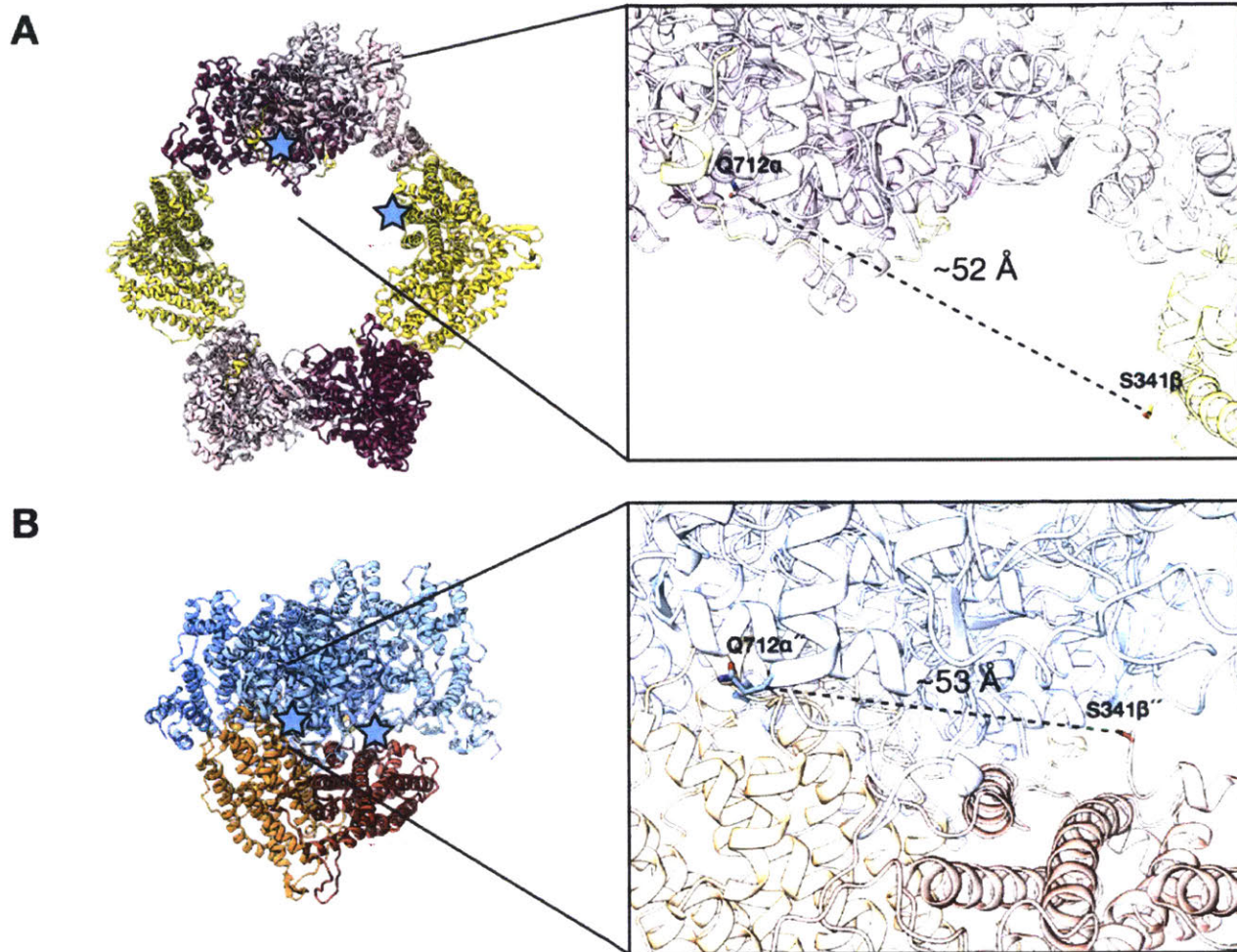


Figure 2.19: Distance comparison of β C-terminus with structure of $\alpha_4\beta_4$. A) In the crystal structure of $\alpha_4\beta_4$, the distance between S341- β and Q712- α , highlighted as blue stars, is ~ 52 Å. The intervening residues are disordered. α_2 is shown in purple/pink and β_2 in yellow. B) In our structure of $\alpha_2\beta_2$, the distance between S341- β'' and Q712- α'' , highlighted as blue stars, is ~ 53 Å. $\alpha_2\beta_2$ is colored as in Figure 2.2. Distances were measured between the C β s of residues.

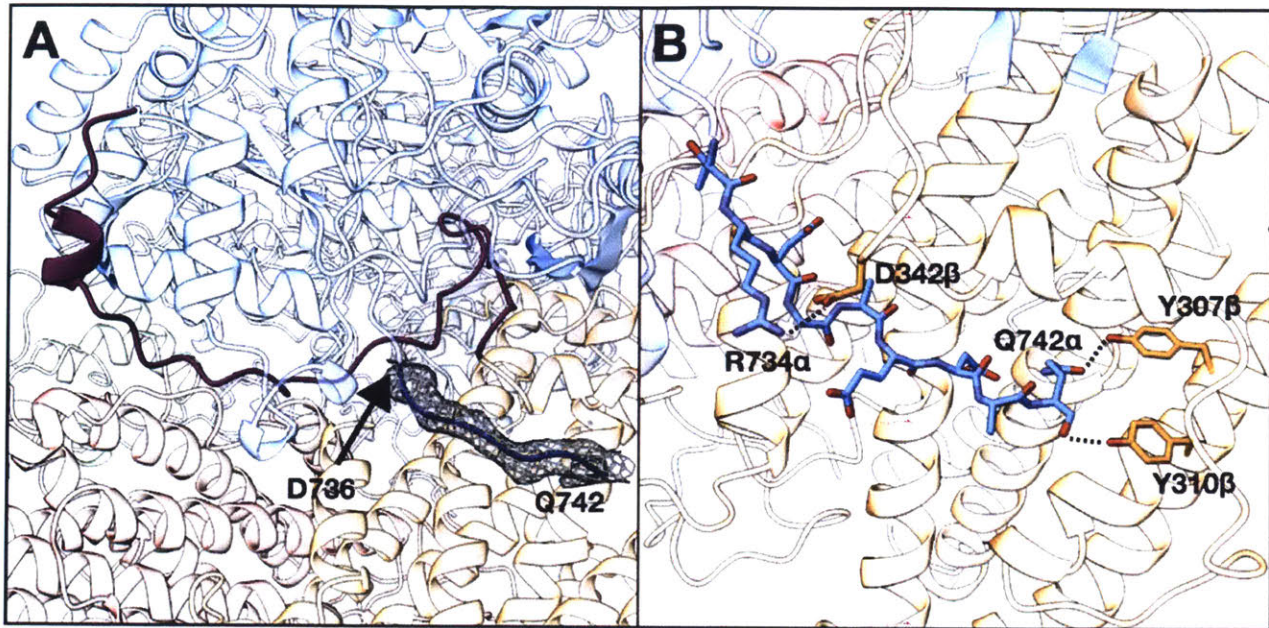


Figure 2.20: Cryo-EM density extends beyond the last visible residue in the $\alpha 2$ crystal structure that was used as the starting model. A) The crystal structure of $\alpha 2$ that was used as part of the starting model to dock into our cryo-EM density was structurally resolved until residue D736. Six additional residues, extending to Q742, were built into the extra cryo-EM density and are colored in dark-blue. Residues 342-375 of β' are shown in purple to highlight its position relative to the C-terminus of α' . B) The C-terminus of α' makes several contacts along β' , including a charge-charge interaction between the side chains of R734 in α' and D342 in β' , and possible H-bonding interactions between the hydroxyl groups of Y307 and Y310 in β' and the side chain and carboxyl group of Q742 in α' , respectively.

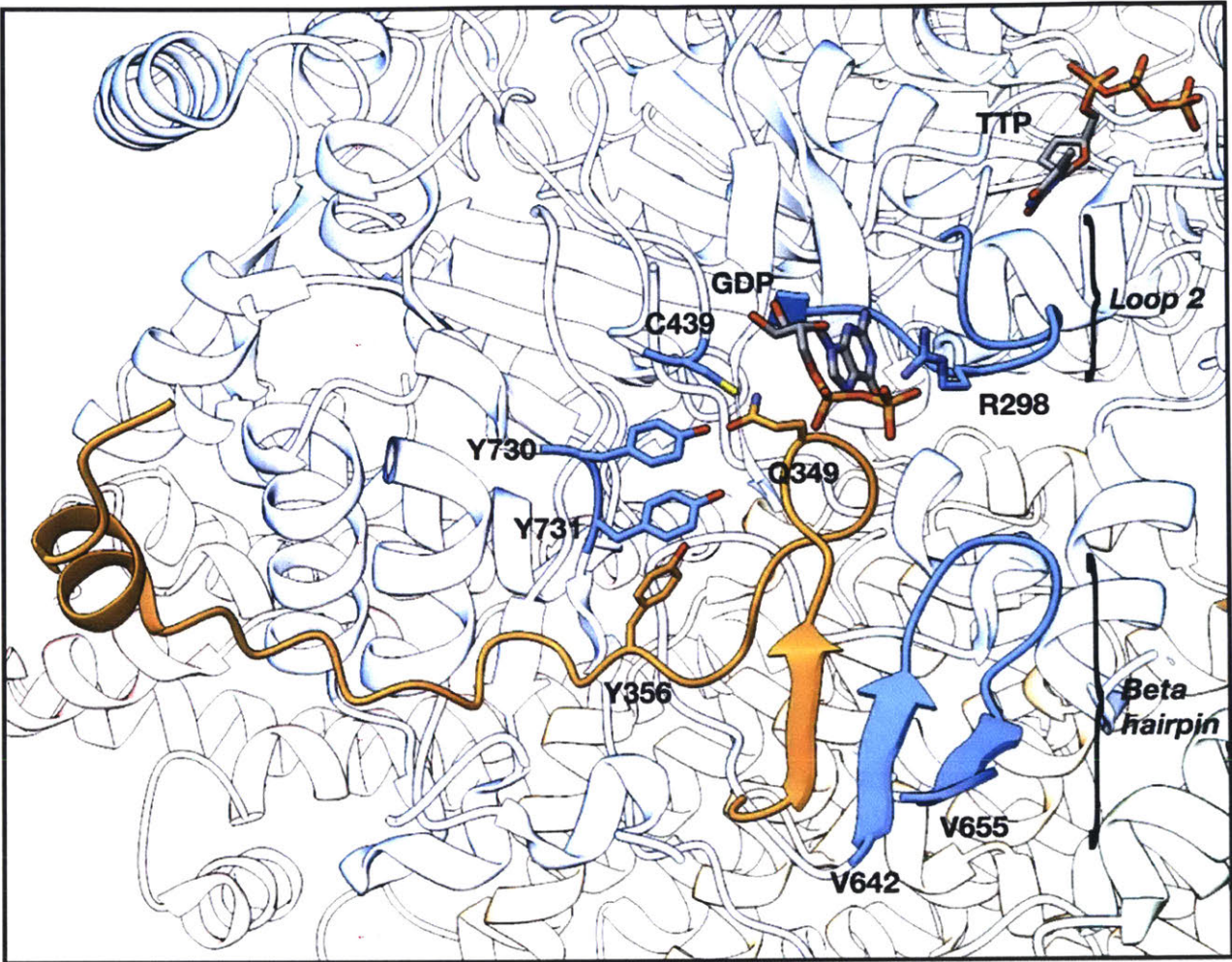


Figure 2.21: Active site environment of the $\alpha_2\beta_2$ complex. The effector TTP binding in the specificity site orients loop 2 of α (residues 292-301) to allow for proper positioning of substrate GDP in the active site. The correct orientation of effector, loop 2, and substrate is recognized by β , which forms a loop that interacts directly with the active site. This loop of β is further stabilized by forming a β -sheet extension with a β -hairpin (residues 642-655) found in α . Colors are as in Figure 2.2.

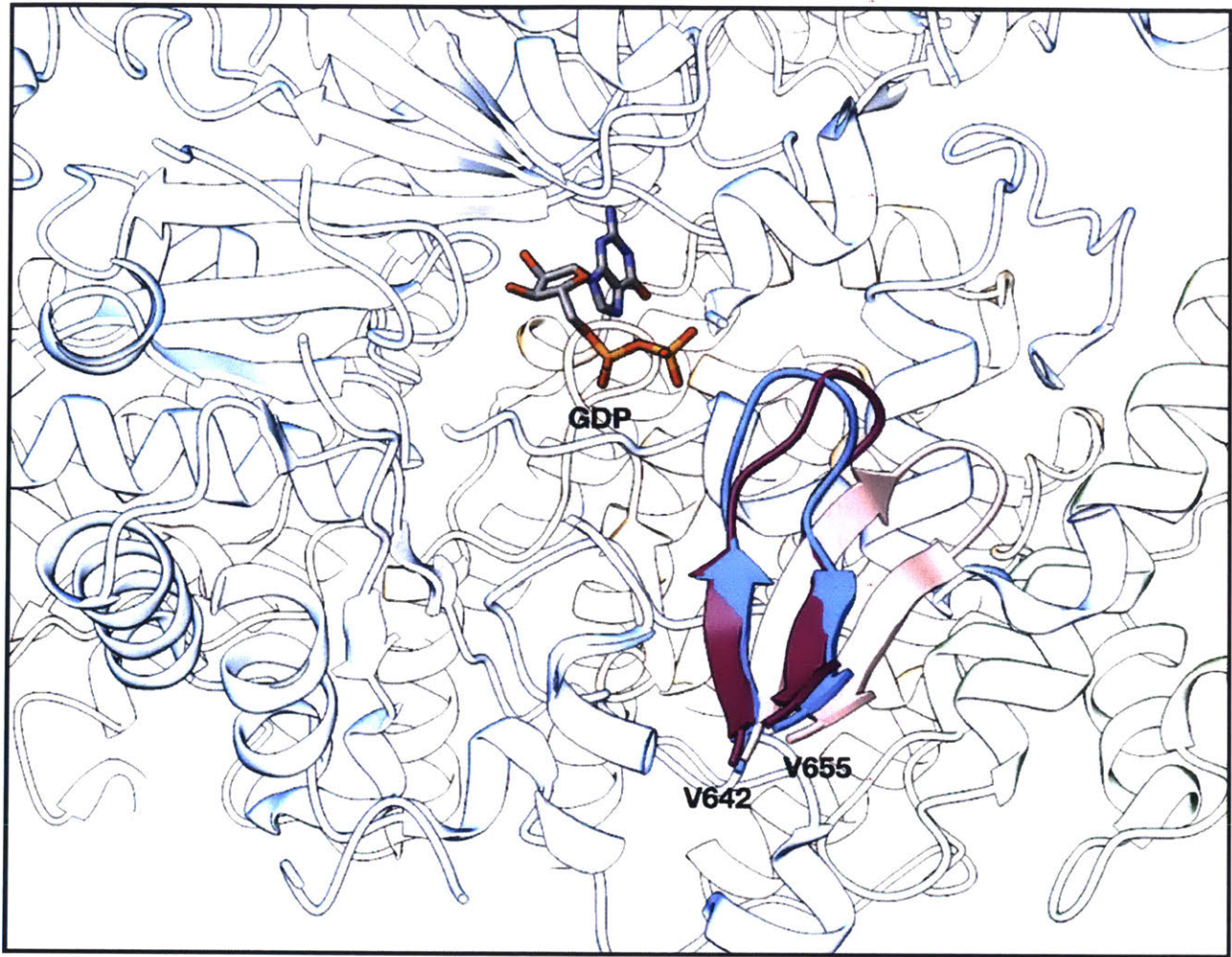


Figure 2.22: β -hairpin of α shifts toward active site upon substrate binding. Upon substrate binding, a β -hairpin in α comprising residues 642-655 shifts towards the active site. Three $\alpha 2$ structures were aligned to highlight the movement of this β -hairpin: substrate-free $\alpha 2$ shown in pink (PDB 2R1R), substrate/effector-bound $\alpha 2$ from inhibited $\alpha 4\beta 4$ shown in purple (PDB 5CNV), and substrate-bound $\alpha 2$ from our structure of active $\alpha 2\beta 2$ shown in blue.

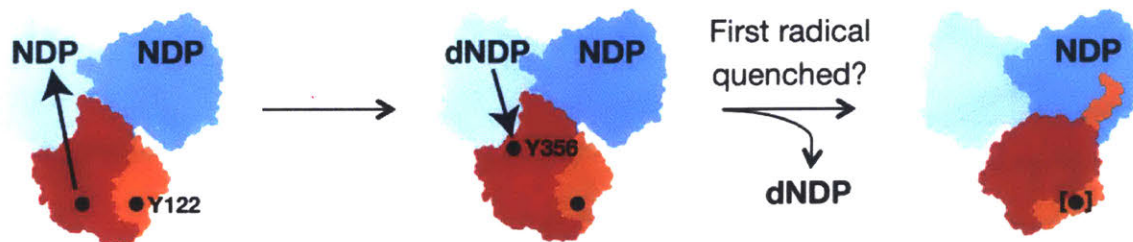


Figure 2.23: Model for single-turnover state trapped by cryo-EM in the presence of WT- α_2 and E52Q/F₃Y122- β_2 . Left: Both monomers of α_2 are primed with substrate and effector and both monomers of β_2 have a radical at F₃Y122. The radical from the β shown in red (β'') fires and turnover occurs in the active site of α shown in light blue (α''). Middle: The radical is stalled on Y356. Product dissociates and β_2 swings over to the other α monomer shown in darker blue (α'). It is unclear if F₃Y122 is re-oxidized prior to this shift. Right: The state trapped in our cryo-EM structure. Substrate is observed in the active site and all key residues on the PCET pathway seem primed for chemistry. The fates of both radicals at this stage are not known.

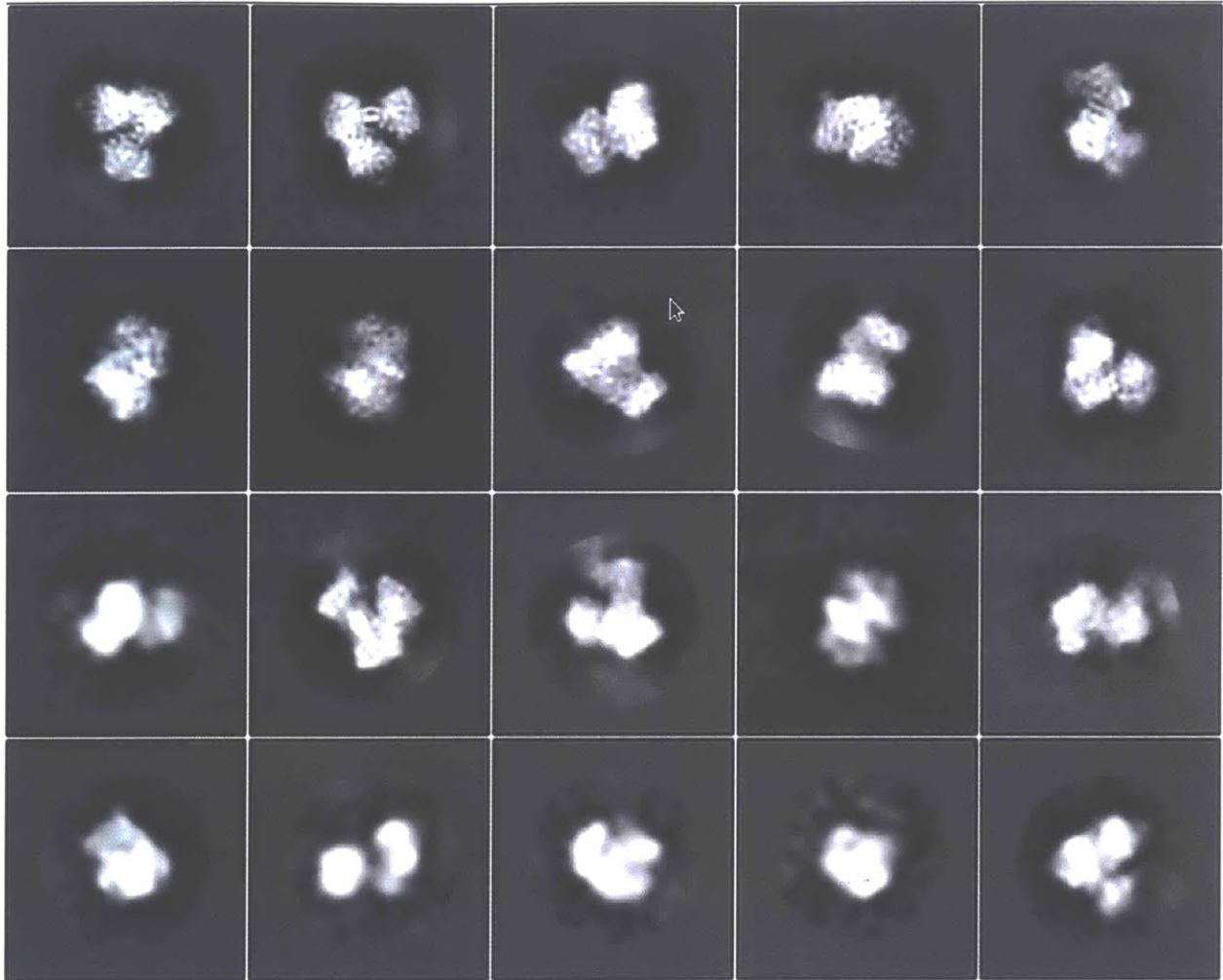


Figure 2.24: Representative classes from initial 2D classification. In some classes, we can observe secondary structural features such as α -helices (top row, second from the left), and others appear less well defined (third row, far left). The classes that are less well defined could either be a result of fewer particles aligning to that particular class or an indication of heterogeneity.

Table 2.1

Imaging parameters and 3D Reconstruction	
Acceleration voltage (kV)	300
Magnification (X)	130,000
Pixel size (Å)	1.059
Number of frames	30
Exposure time (s)	6
Total exposure (e ⁻ / Å)	47.1
Particles	
Micrographs used for selection	5062
Defocus range (um)	1.3-2.8
Windowed	~200,000
In final 3D reconstruction	80,386
Resolution	
'Gold-standard' at FSC 0.143 (Å)	3.6

Table 2.2

Model refinement	
Resolution in phenix.real_space_refine (Å)	3.2
Number of atoms/residues/molecules	
Protein atoms, residues per chain	
Chain A	5854, 736
Chain B	5874, 738
Chain F	3061, 375
Chain D	2792, 341
Nucleotide atoms, molecules per chain	
Chain A	29, 1
Chain B	57, 2
Mg ²⁺	2
Fe	4
Water molecules	4
Secondary structure restraints	
Helices	102
Sheets	12
Ramachandran	2176
Hydrogen bonds	968
C-beta torsion restraints	4148
Ramachandran angles	
Favored (%)	94.03
Allowed (%)	5.97
Outliers (%)	0.05
r.m.s. deviations	
Bond lengths (Å)	0.004
Bond angles (°)	0.634
Molprobit	
Score	1.98
Clashscore	11.52
Omegalize outliers (residues per chain)	0
EMRinger Score	1.98

Chapter 3

Cryo-EM structure of wildtype $\alpha 2\beta 2$ in the presence of mechanism-based inhibitor N_3UDP

We thank Dr. Kanchana Ravichandran for providing protein and N_3UDP that made this project possible. We thank Dr. Ed Brignole, who helped with optimizing parameters for cryo-EM grid preparation. Emily Damato worked with Dr. Ed Brignole to generate the initial reconstruction processed in SPHIRE. Emily worked with Tristan Bepler in optimizing parameters for automated particle-picking, leading to the particle coordinates that were used in subsequent reprocessing of the data. The data discussed herein were collected at Janelia Research Campus of the Howard Hughes Medical Institute with the help of Dr. Rick Huang.

3.A Summary

Ribonucleotide reductases (RNRs) catalyze the reduction of nucleotides to their deoxynucleotide counterparts, a critical process in DNA synthesis and repair. Class Ia RNRs are composed of two homodimeric subunits, α_2 and β_2 , and successful nucleotide reduction is dependent on the careful coordination of both chemical and physical steps. Here, we discuss a structure of wildtype *E. coli* class Ia RNR in its active $\alpha_2\beta_2$ state solved in the presence of substrate inhibitor 2'-azido-2'-deoxyuridine-5'-diphosphate (N_3 UDP), which has been widely used to probe the chemical mechanism of nucleotide reduction in RNR. The incubation of N_3 UDP with RNR leads to the generation of a unique nitrogen-centered radical ($N\bullet$) within the active site whose formation is tied to an increase in $\alpha_2\beta_2$ -complex lifetime, allowing for structural studies. The use of the unnatural substrate, N_3 UDP, results in unique structural conformations within the active site following chemistry compared to the structure of E52Q/F₃Y- $\alpha_2\beta_2$ discussed in Chapter 2, which contained natural substrate GDP. Additionally, we observe across several methods of analysis, the appearance of extra cryo-EM density in a common location along the α_2 subunit, which we speculate may be the C-terminus of α_2 . The C-terminus of α_2 is known to contain a pair of redox-active cysteines that shuttle reducing equivalents for nucleotide reduction to the active site but has yet to be visualized in the well-studied *E. coli* class Ia RNR and its structural dynamics during turnover remain an open question.

3.B Introduction

Ribonucleotide reductase (RNR) is responsible for generating deoxyribonucleotides from their ribonucleotide counterparts and is thus a critical player in the maintenance of DNA biosynthesis in all organisms^{1,2}. Class Ia RNR from *Escherichia coli* is composed of two homodimeric subunits, α 2 and β 2 (**Figure 3.1**), and utilizes a tyrosyl-radical cofactor to generate a transient thiyl-radical in the active site that initiates nucleotide reduction³⁻⁵. The radical-cofactor is generated and housed within β 2 (Y122•), whereas the active-site cysteine that undergoes oxidation to form the thiyl-radical (C439) is found in α 2. Thus for chemistry to occur, the two subunits must come together to form the active α 2 β 2 complex^{3,6}. The reducing equivalents for nucleotide reduction come from a pair of conserved redox-active cysteines (C225, C462) in the active-site that get oxidized to a disulfide concomitant with product formation. Before subsequent rounds of turnover can occur, these cysteines are re-reduced via disulfide exchange by a second pair of cysteines (C754, C759) located on the very C-terminus of the α 2 subunit⁷ (**Figure 3.1**). α 2 also contains an allosteric N-terminal activity site, referred to as the cone-domain, that regulates overall activity^{3,8}. dATP binding to this site inhibits enzymatic activity by shifting the oligomeric equilibrium towards the formation of an α 4 β 4 ring complex⁹, which precludes radical transfer between the subunits and ATP can displace dATP at this site to restore activity¹⁰ (**Figure 3.1**). Given the intimate coordination between chemical and physical steps, we need an understanding of both processes in order to have a full appreciation of RNR activity.

Since their discovery in the late 1970s, the mechanism-based inhibitors, 2'-azido-2'-deoxynucleotides (N₃NDPs), have been used to investigate the catalytic mechanism of nucleotide reduction of RNR *in vitro*¹¹⁻¹⁷. The incubation of N₃NDP with RNR results in the formation of 0.5 equivalents of a new nitrogen-centered radical in the active site (N•) concomitant with the stoichiometric loss of Y122•, evidence for half-sites reactivity in the wildtype enzyme^{11,16}. The structure of the N• has been proposed via biochemical and spectroscopic studies to consist of a nitrogen atom that is covalently attached to both

the nucleotide through the 3'-carbon of the ribose and the active site residue C225¹³ (**Figure 3.2**). However, the structure of N• has never been structurally visualized and remains an open question. The appearance of the N• is also accompanied by an increased affinity between the $\alpha 2$ and $\beta 2$ subunits, which interested us from a structural standpoint as a possible strategy to obtain a structure of the active $\alpha 2\beta 2$ complex, which at the time had yet to be solved.

To add to the complexity of studying the process of nucleotide reduction, class Ia RNR is rate-limited not by the chemical steps but by physical conformationally dynamic steps both preceding and following turnover¹⁸. One of these physical steps includes the dynamics of re-reduction of the disulfide that forms between C225 and C462 in the active site by C754/C759 subsequent to turnover⁷. This lack of molecular information is largely attributable to the fact that the two cysteines, C754/C759 are located in the last ~25 residues of the C-terminus of $\alpha 2$, which have been disordered in all previous *E. coli* class Ia RNR structures^{3,19,20}.

Here, we present and discuss a structure of active *E. coli* class Ia RNR solved in the presence of WT- $\alpha 2\beta 2$ and N₃UDP, using cryo-electron microscopy (cryo-EM). The dataset was processed twice using two different software packages SPHIRE and Relion 3.0, which lead to structures that were 8-Å and 5-Å resolution, respectively. The complex, as with the active-state structure discussed in Chapter 2 (E52Q/F₃Y- $\alpha 2\beta 2$), is again an asymmetric $\alpha 2\beta 2$ complex. The consequences of using the unnatural substrate N₃UDP lead to key structural differences within the active site where chemistry had occurred relative to the post-turnover active site found in E52Q/F₃Y- $\alpha 2\beta 2$. Further, the presence of ATP in our reaction conditions lead to both cone-domains of $\alpha 2$ being structurally ordered, with observed cryo-EM density indicative of bound nucleotide. Lastly, the observation of additional cryo-EM density found along the outside of the cone-domain proximal to the $\beta 2$ subunit lead us to speculate on the position and role of the α C-terminus during turnover.

3.C Results

Data processing using SPHIRE software suite

Chronologically, the initial data processing using the SPHIRE²¹ (**SP**arx for **H**igh **R**esolution **E**lectron **M**icroscopy) software suite was performed prior to the acquisition of the data and structure discussed in Chapter 2 (E52Q/F₃Y- α 2 β 2).

The dataset processed using the SPHIRE software package lead to an ~8-Å resolution cryo-EM density map where we could confidently dock in the crystal structures of the α 2 and β 2 subunits (**Figure 3.3**). It is an asymmetric α 2 β 2 complex, with β 2 mostly interacting with one α monomer (hereto referred to as α') (**Figure 3.3**). The crystal structures of α 2 and β 2 that were docked into the density were resolved to residues 737 (of 762) and 340 (of 375), respectively^{19,22} (PDB 4R1R, 1RIB). Additionally, the docked structure of α 2 was co-crystallized with a peptide sharing the sequence of the C-terminus of β 2, with 16 residues (corresponding to 360-375) being structurally resolved in the overall structure. There were therefore 19 residues of the β 2 subunit (341-359) for which we lacked any structural information at the time.

At this resolution, secondary structural features such as α -helices begin to become apparent (**Figure 3.4A**). Additionally, we observe density corresponding to the position of the last 16 residues of the C-terminus of β 2, bound in the groove formed by two α -helices, comprising residues 341-348 and 711-723, of the α subunit, similar to both the crystal structure of α 2 alone^{3,19} or in the α 4 β 4 inhibited complex²⁰, as well as now the structure of E52Q/F₃Y- α 2 β 2 (Chapter 2). Mirroring the E52Q/F₃Y- α 2 β 2 structure, we only observe density for the C-terminus of β along one α -monomer (hereto referred to as α'), rather than both as in the crystal structures of α 2 and α 4 β 4 (**Figure 3.4B**). However, given the lack of density at the interface, we were at the time unable to determine from which of the two β monomers the observed C-terminus originated. Another major difference between the two α -monomers is observed in the rigidity of the

N-terminal cone-domains, wherein the one belonging to α' appears well ordered and the one belonging to the other α monomer (hereto referred to as α'') has some associated cryo-EM density but much less so, suggesting a higher degree of heterogeneity (**Figure 3.4C**).

Unfortunately, little to no cryo-EM density was observed at the α 2- β 2 interface. Not only did we not observe any density that could correspond to the structurally uncharacterized residues of β 2 (341-359), there was not enough cryo-EM density to model in known structural features including loops and helices (**Figure 3.5**).

3D classification and 3D variance analyses in SPHIRE

In an effort to tease out any structural heterogeneity that may be present in the overall 3D reconstruction, 3D classification was performed wherein five target classes were generated. One class clearly converged to an α 2 β 2 complex whereas the remaining four classes consisted of high levels of noise. In the converged class, we observe nominal extra density at the α' - β 2 interface, including between residue 342 of one β monomer (hereto referred to as β') and the visible β C-terminal region (**Figure 3.6**).

Calculating 3D variance, which highlights regions of relative structural heterogeneity, revealed two regions of density corresponding to high variance. Unsurprisingly, the first corresponded to the cone-domain of α'' . This variance was not observed for the cone-domain of α' , perhaps suggesting β 2 plays a role in further stabilizing the cone-domain structure. The second region of variance density was observed close to the last visible residue at the C-terminus of both α monomers, leading away from the core of the subunit. In the case of α' , this density was observed along the cone-domain of α' near helices 1 and 2 (residues 20-48, **Figure 3.7**). Surprisingly, the variance density along the outside of the cone-domain of α' align closely with extra density observed in our results from 3D classification. (**Figure 3.8**). We were somewhat puzzled at the time to find that 3D variance analysis revealed no additional density at the α 2- β 2 interface.

Data processing using Relion 3.0

The re-processing of the data in Relion 3.0²³ was performed after having solved the structure of E52Q/F₃Y- α 2 β 2, affording us a higher-resolution structure (3.6-Å resolution, Chapter 2) as a starting point in our analyses.

Re-processing the data in Relion 3.0, using a new particle set generated from the automatic particle-picker Topaz²⁴, lead to a reconstruction that was ~5-Å resolution (**Figure 3.9**). At this resolution, secondary structural features such as α -helices and in some cases β -strands become readily apparent, and we were able to perform real-space refinement²⁵ using the structure of E52Q/F₃Y- α 2 β 2 as the starting model against the new cryo-EM density described here. Unfortunately, the resolution does not allow us to visualize or refine side chains. The structure refined into the 5-Å resolution map processed in Relion will be referred to as N₃UDP- α 2 β 2.

Comparisons with E52Q/F₃Y- α 2 β 2

In order to examine which regions of the N₃UDP- α 2 β 2 structure deviated most from the structure of E52Q/F₃Y- α 2 β 2, root-mean-square deviation (RMSD) values were calculated between pairs of each respective subunit monomer and are summarized in **Table 3.1**.

The highest deviation was found between α'' of N₃UDP- α 2 β 2 and α'' of E52Q/F₃Y- α 2 β 2, with an RMSD of 1.49 Å over 736 C α atoms. The RMSDs between the remaining chain pairs (i.e. α' - α' , β' - β' , β'' - β'') across all respective C α atoms were ~0.9-1.0 Å.

The C-terminus of β is fully resolved

To our surprise, we observe cryo-EM density for the entire length of one β monomer (β'), and the positioning of the β -tail to form a loop towards the active site of α' mirrors

that observed in the structure of E52Q/F₃Y- α 2 β 2 (**Figure 3.10**, **Figure 2.9**). This is in stark contrast to our previous analyses using SPHIRE described above, where we observed no identifiable cryo-EM density at the α' - β 2 interface, neither in the overall reconstruction nor after 3D variance and classification analyses, which had lead us to believe that the interface region was disordered, possibly as a consequence of using the N₃UDP substrate.

Both cone domains are ordered

We observe that both cone-domains of α' and α'' are largely ordered, unsurprising given the presence of ATP in our reaction conditions, which binds at this site²⁶. Even so, we see that at the same density contour level, the cone-domain of α' shows better defined cryo-EM density relative to α'' , indicative of being more structurally rigid (**Figure 3.11**). The observation that both cone-domains are ordered is in contrast to E52Q/F₃Y- α 2 β 2, where in the absence of activity effector, the cone-domain of α'' was completely disordered (**Figure 2.17**).

In both cone-domains, we observe extra cryo-EM density that is not accounted for after docking of the helix bundle, that we suspect is ATP, which was present in our experimental conditions at 3 mM. In a previous crystal structure of α 2 solved in the presence of ATP, it was found that the nucleotides interact with residues K9, R10, E15, N18, K21, R24, W28, T55, H59, F87, F97 of the cone-domain²⁶. We find that the extra density we observe in the cone-domain are indeed near these residues (**Figure 3.12**) and do not observe comparable density in the E52Q/F₃Y- α 2 β 2 structure. An additional consequence of ATP being bound in the cone-domain is that we observe some cryo-EM density for the N-terminal β -hairpin loop (residues 1-16), which interacts with bound activity effector. This observation is again in contrast to what was observed in the structure of E52Q/F₃Y- α 2 β 2, which lacked any effector bound at this site, and thus this β -hairpin loop was disordered (**Figure 3.12**).

C225/C462 of N₃UDP- α 2 β 2 α'' are found in a unique conformation

In the case of E52Q/F₃Y- α 2 β 2, we observed that only one α monomer of the symmetric α 2 crystal structure docks properly into the α 2 cryo-EM density, motivating us to further explore the differences between the two α monomers. This investigation led to the realization that one active site, that of α'' , had undergone turnover with a disulfide observed between C225/C462, which are the two cysteines that provide the reducing equivalents for nucleotide reduction. The active site of α' in E52Q/F₃Y- α 2 β 2 appeared to have not yet undergone turnover, with clear density for substrate and C225/C462 in their reduced state (**Figure 2.15**).

Similarly, with N₃UDP- α 2 β 2 discussed here, we again noticed that the overall structures of the α monomers were different from each other when docked into the cryo-EM density. α' of N₃UDP- α 2 β 2 mirrors what we observed with α' of E52Q/F₃Y- α 2 β 2. Even at the current resolution, we observe density in the active site indicative of bound N₃UDP, and the two β -strands housing the redox active cysteine pair C225/C462 align as if they are in the reduced state (**Figure 3.13A**). Interestingly, the analogous β -strands in α'' are positioned neither clearly as found in the structures with reduced C225/C462 nor oxidized C225/C462. Rather, there is a “smear” of density wherein following refinement into the density, C462 appears positioned somewhere in between its position in the reduced and oxidized states, and C225 closer to its position in the oxidized state (**Figure 3.13B**). In contrast to the active site of α'' in the E52Q/F₃Y- α 2 β 2 structure where we observed no additional density for substrate or product, here we observe additional density adjacent to, and possibly contiguous with, the density corresponding to the C225 (**Figure 3.13C**). This finding is especially interesting in light of the proposed structure of N• being covalently attached to the 3'-C of the ribose and C225¹³.

C-terminus of α subunit

In all previous crystal structures of α_2 , approximately 25 residues (of 762) from the flexible C-terminus have always been disordered^{3,19,20}. In our structure of E52Q/F₃Y- $\alpha_2\beta_2$ discussed in Chapter 2, we observed additional cryo-EM density beyond what had been structurally characterized that allowed us to model an additional 6 residues extending out to residue 742. In our structure of N₃UDP- $\alpha_2\beta_2$ discussed here, we observe extra cryo-EM density in the same location such that the additional residues modeled into the E52Q/F₃Y- $\alpha_2\beta_2$ structure fit well into the N₃UDP- $\alpha_2\beta_2$ cryo-EM density (**Figure 3.14A**).

Further, we again observe additional density near the cone-domain of α' , specifically adjacent to helices 1 and 2, as was observed previously in our 3D variance and classification analyses using SPHIRE. Given the proximity of this extra density to the last visible residue in the structure (742 of α'), we speculate that it could correspond to part of the remaining structurally uncharacterized residues of the α C-terminus (**Figure 3.14B**).

3.D Discussion

The dataset corresponding to N₃UDP- α 2 β 2 was processed twice, once using the SPHIRE software suite, and a second time using Relion 3.0. Chronologically, the analysis in SPHIRE was done first, followed by the analysis of E52Q/F₃Y- α 2 β 2 using Relion 3.0 (discussed in Chapter 2), and lastly, the analysis of N₃UDP- α 2 β 2 using Relion 3.0. Prior analysis of the E52Q/F₃Y- α 2 β 2 data afforded us the luxury of a higher-resolution structure with which to compare the re-processed structure of N₃UDP- α 2 β 2 and thus much of the discussion will be in that context.

Nucleotide reduction performed by class Ia RNRs requires a careful coordination of both chemical and conformational steps^{5,18,27}. Therefore, compared to the use of wild-type substrate, we had to recognize that the use of N₃UDP, which causes a significant chemical and physical perturbation within the active site, could lead to structural consequences such as increased heterogeneity when it comes to studying the α 2 β 2 complex.

One such consequence of incubating N₃UDP with RNR is the proposed formation of a unique N• in the active site. This N• is proposed to form a covalent adduct to the 3'-C of the nucleotide as well as C225 of α ¹³. Mechanistically, the use of N₃UDP prevents a disulfide from forming between C225 and C462, which as we discussed in Chapter 2, leads to a contraction of the active site that we believe promotes product release. As a result, we observe an interesting state in our structure of N₃UDP- α 2 β 2, where in the active site of α ' that appears to have undergone chemistry, C225 refines into a position closely aligned to its oxidized state and C462 refines to an intermediate position between its oxidized and reduced states. Rather than observing cryo-EM density indicative of a disulfide between C225-C462, we observe density contiguous with C225 toward the substrate-binding site within the active site of α '', which lead us to speculate whether we had trapped the reaction intermediate corresponding to N•. Notably, in previous studies examining the N• species by high-field EPR, the reaction mixture was

incubated for 5 minutes after the addition of N₃UDP, a time scale comparable to our sample preparations¹³ (grids were frozen following a 3.5-5 minute incubation at ambient temperature after reaction initiation). Analogous cryo-EM density near C225 is absent in the active site of α'' in E52Q/F₃Y- α 2 β 2, which included native substrate GDP in the reaction conditions (Chapter 2). Despite our reported average resolution for the overall structure, the fact that we observe cryo-EM density corresponding to nucleotides in other binding sites within α 2 lends further weight to the hypothesis that what we observe in the active-site of α'' may indeed be of the N• species. However, a higher-resolution structure is necessary to more confidently state one way or the other. Further, the observation that β 2 was found interacting with α' rather than α'' , suggests that full oxidation of the C225/C462 pair is not a prerequisite for β 2 translocating from one α monomer to the other.

A long-standing question when it comes to the α 2 subunit has been the dynamics of its C-terminal tail during the course of turnover, as it has always been disordered in previous structures. Therefore, when we were initially analyzing the E52Q/F₃Y- α 2 β 2 structure prior to the re-analysis of N₃UDP- α 2 β 2, we were somewhat surprised to find that we could model additional residues at the C-terminus of α' (extending out to residue 742), and further, that these residues appeared to be very close to, and possibly interacting with, the β 2 subunit (specifically β'). We observe cryo-EM density for these same residues in our structure of N₃UDP- α 2 β 2, suggesting that these additional interactions between the C-terminus of α' and β' are part of forming a tight α 2 β 2 complex. Beyond these residues, we also repeatedly observed, both in our analyses in SPHIRE as well as Relion, additional cryo-EM density along the cone-domain of α' , specifically adjacent to helices 1 and 2 (residues 20-48). Based on the proximity of this density to residue 742- α' , it is tempting to speculate that we are observing part of the remaining 20 structurally uncharacterized residues of α' . Perhaps rather than remaining flexible and disordered during the course of turnover, the C-terminus of α remains in a sort of “resting state” proximal to its cone-domain. Based on our observation (see Chapter 2) that the active site is inaccessible to re-reduction as long as the radical

transfer pathway is intact, the positioning of the α C-terminus speculated here, if true, could be a way that the α C-terminus “senses” the departure of β after turnover.

The two structures of $\alpha_2\beta_2$, presented in Chapter 2 and now here, were each trapped using different perturbation methods with the common goal of stalling the radical off its native path. E52Q/F₃Y- $\alpha_2\beta_2$ involved perturbing the radical translocation pathway and N₃UDP- $\alpha_2\beta_2$ involved perturbing the nucleotide reduction reaction. However, it appears that in both cases the sequence of events is the same: the first radical fires (denoted in both discussed structures as radical firing from β'' to the active site of α''), after some time period β_2 migrates from one α monomer to the other (i.e. from α'' to α'), and the reaction is either stalled or prevented from occurring between β' and α' . In the case of E52Q/F₃Y- $\alpha_2\beta_2$, it is unclear whether the radical returns to F₃Y122- β'' before β_2 migrates from α'' to α' . And in the case of N₃UDP- $\alpha_2\beta_2$, the α'' active site following chemistry looks quite different from that of wildtype with the apparent presence of a reaction-intermediate adduct to C225. Yet in both cases, β_2 appears to have translocated from the α monomer it initially interacted with (α'') to the other α monomer (α'). Previous studies on the pre-steady state kinetics of *E. coli* class Ia RNR revealed a rapid phase during which approximately two equivalents of product are formed¹⁸, but it is interesting to think that this tendency towards two rounds of turnover may be strong enough to overcome deviations from native radical translocation and substrate turnover. Unfortunately, the resolutions of the two $\alpha_2\beta_2$ structures presented do not allow us to propose a structural reason as to how we have trapped structures in which the second radical (from β') appears to have not yet fired. However, we can speculate that perhaps there is a regulatory mechanism by which the second radical is either stalled or prevented from firing depending on whether a radical is present on the opposite Y122.

Higher-resolution structures will be necessary to confirm or refute what has been discussed here. To that end, efforts are on-going to obtain a structure of WT- $\alpha_2\beta_2$ in the presence of N₃CDP, which also forms the N• species in the active site¹¹, rather than N₃UDP. The kinetics of N• formation in N₃CDP (seconds time scale for reaction

completion) is much faster than in N₃UDP (minutes times scale for reaction completion), which may facilitate trapping a more homogeneous complex²⁸. Additionally, obtaining a structure of $\alpha_2\beta_2$ whereby the last ~20 residues of α_2 have been truncated, may shed light on the identity of the extra density we observe adjacent to the cone-domain of α' .

3.E Materials and Methods

Protein preparation

$\alpha 2$ (specific activity of ~ 2500 nmol/min/mg), $\beta 2$ (1.2 Y122●, ~ 7000 nmol/min/mg), and N_3 UDP were provided by Kanchana Ravichandran in the Stubbe lab and prepared as previously described^{16,29}. The concentrations of $\alpha 2$ and $\beta 2$ were determined using their respective extinction coefficients (A280) of 189 and 131 $\text{mM}^{-1}\text{cm}^{-1}$, respectively. All concentrations are for the respective dimers.

Grid preparation

Grids were prepared on Quantifoil 1.2-1.3 Cu 300 mesh holey-carbon grids and plunged on a Gatan Cp3 plunger in the cold room. The final protein solution contained 0.66 μM $\alpha 2$, 1.3 μM $\beta 2$, 1 mM N_3 UDP, 3 mM ATP, 50 mM HEPES, 15 mM MgSO_4 , 1 mM EDTA, pH 7.6. $\alpha 2$ was incubated with nucleotides for 1 minute at RT before reaction initiation with $\beta 2$. The final solution was incubated for an additional 3 min at 25°C before plunging. Grids were glow-discharged at -15 mA for 1 minute before protein solution was applied. 2.6 μL sample was applied to the grids that were blotted for 4.5 seconds (Whatman filter paper #1) before plunging into liquid ethane and transferring to storage grids.

Data collection

Data were collected at the Cryo-EM Core Facility at Janelia Research Campus on a Thermo Fisher Titan Krios 300 kV electron microscope equipped with a Gatan GIF K2 camera. Parameters were as follows: 81,000x magnification, 1.35 Å/pix (collected at super-resolution of 0.675 Å/pix), 50 frames over 15 seconds, 82.3 $\text{e}^{-}/\text{Å}^2$ total dose, defocus range 1.5-3.0 μm . 1582 total dose fractionated movies were acquired (**Table 3.2**).

Initial frame alignment, defocus estimation, and micrograph assessment in SPHIRE

Using a script provided by Dr. Ed Brignole (~ed/sxlib/MicrosFrameAlign.py), the collected movies were gain corrected with IMOD³⁰, frames were aligned using Unblur³¹, and movies were summed with and without dose compensation using SumMovie³¹. CTF estimation was performed in SPHIRE²¹ and subsequent CTF and drift assessments were used to trim the data set down to ~1200 micrographs.

Particle selection and sub-selection

e2boxer.py within EMAN2³² was used to initially generate 7592 particles from a subset of 51 micrographs. Class averages of these particles were used to select particles from the full ~1200 micrograph dataset resulting in 270,618 particles. Through iterative rounds of 2D class averaging using sxisac.py within SPHIRE²¹, and cutting bad particles, final lists of 98,234 and 64,791 particles were generated for further analysis, based on a qualitative cut-off for dataset purity (**Table III.2**).

3D map generation and post-processing in SPHIRE

2D class averages from the cleaned data sets were used to generate an initial model using sxrviper.py, which was then used to generate a refined 3D reconstruction with the full particle set using sxmeridien.py. 3D classification was performed to generate four classes consisting ~25,000 particles each. Both 3D variance and classification were performed using Sort3D within SPHIRE.

Particle selection in Topaz

An initial set of ~2000 particles were manually picked from a subset of aligned movies. These model particles were then used to train a neural-net automated particle picker Topaz²⁴, which was then used to automatically pick particles from the entire data set

using a threshold of 0 for the cut-off for positive signal, which resulted in 216,521 initial particle hits.

Frame alignment and defocus estimation in Relion 3.0

Frame alignment was rerun using Relion's implementation of motion_corr2³³ within the Relion 3.0 software suite²³. CTF estimation was also rerun using the output from Relion's motion_corr2 using ctffind4³⁴.

Map generation and refinement in Relion 3.0

The coordinate set of 216,521 particles from Topaz was used to re-extract particles and perform initial 2D classification of 1000 classes. From these, 28 of the best qualitative classes (as defined by structural definition), comprising 85,753 particles were chosen for further analysis (**Table III.2**). These 28 classes were used to generate the initial reference-free 3D model followed by high-resolution 3D refinement using the entire particle set. CTF refinement was performed using CTF parameter fitting and per-particle defocus fitting. Particle polishing was performed using the Bayesian method of particle motion estimation. The refined particle set was used to rerun high-resolution 3D refinement to generate the final map. The final resolution at FSC=0.143 was 5.0 Å.

Model building and refinement

Coordinates from the structure of the $\alpha 2\beta 2$ complex solved using WT- $\alpha 2$ and E52Q-(2,3,5)F3Y- $\beta 2$ (Chapter 2) were docked into the EM reconstruction using UCSF ChimeraX³⁵ and used as the starting model. After manually disrupting the disulfide between C225 and C462 in chain A using COOT³⁶, one round of refinement was performed using Phenix Real Space Refine²⁵. For real space refinement, resolution was set to 4.5 Å, and electron scattering table was selected. Figures of the model and map were generated using UCSF ChimeraX.

3.F References

- 1 Hofer, A., Crona, M., Logan, D. T. & Sjoberg, B. M. DNA building blocks: keeping control of manufacture. *Crit Rev Biochem Mol Biol* **47**, 50-63, doi:10.3109/10409238.2011.630372 (2012).
- 2 Nordlund, P. & Reichard, P. Ribonucleotide reductases. *Annu Rev Biochem* **75**, 681-706, doi:10.1146/annurev.biochem.75.103004.142443 (2006).
- 3 Uhlin, U. & Eklund, H. Structure of ribonucleotide reductase protein R1. *Nature* **370**, 533-539, doi:10.1038/370533a0 (1994).
- 4 Nordlund, P., Sjoberg, B. M. & Eklund, H. Three-dimensional structure of the free radical protein of ribonucleotide reductase. *Nature* **345**, 593-598, doi:10.1038/345593a0 (1990).
- 5 Stubbe, J., Nocera, D. G., Yee, C. S. & Chang, M. C. Radical initiation in the class I ribonucleotide reductase: long-range proton-coupled electron transfer? *Chem Rev* **103**, 2167-2201, doi:10.1021/cr020421u (2003).
- 6 Brown, N. C. & Reichard, P. Ribonucleoside diphosphate reductase. Formation of active and inactive complexes of proteins B1 and B2. *J Mol Biol* **46**, 25-38 (1969).
- 7 Mao, S. S. *et al.* A model for the role of multiple cysteine residues involved in ribonucleotide reduction: amazing and still confusing. *Biochemistry* **31**, 9733-9743, doi:10.1021/bi00155a029 (1992).
- 8 Aravind, L., Wolf, Y. I. & Koonin, E. V. The ATP-cone: an evolutionarily mobile, ATP-binding regulatory domain. *J Mol Microbiol Biotechnol* **2**, 191-194 (2000).
- 9 Zimanyi, C. M. *et al.* Tangled up in knots: structures of inactivated forms of E. coli class Ia ribonucleotide reductase. *Structure* **20**, 1374-1383, doi:10.1016/j.str.2012.05.009 (2012).
- 10 Ando, N. *et al.* Structural interconversions modulate activity of Escherichia coli ribonucleotide reductase. *Proc Natl Acad Sci U S A* **108**, 21046-21051, doi:10.1073/pnas.1112715108 (2011).
- 11 Sjoberg, B. M., Graslund, A. & Eckstein, F. A substrate radical intermediate in the reaction between ribonucleotide reductase from Escherichia coli and 2'-azido-2'-deoxynucleoside diphosphates. *J Biol Chem* **258**, 8060-8067 (1983).
- 12 Thelander, L. & Larsson, B. Active site of ribonucleoside diphosphate reductase from Escherichia coli. Inactivation of the enzyme by 2'-substituted ribonucleoside diphosphates. *J Biol Chem* **251**, 1398-1405 (1976).
- 13 Fritscher, J. *et al.* Structure of the nitrogen-centered radical formed during inactivation of E. coli ribonucleotide reductase by 2'-azido-2'-deoxyuridine-5'-diphosphate: trapping of the 3'-ketonucleotide. *J Am Chem Soc* **127**, 7729-7738, doi:10.1021/ja043111x (2005).
- 14 Vanderdonk, W. A., Stubbe, J., Gerfen, G. J., Bellew, B. F. & Griffin, R. G. Epr Investigations of the Inactivation of Escherichia-Coli Ribonucleotide Reductase with 2'-Azido-2'-Deoxyuridine 5'-Diphosphate - Evidence for the Involvement of the Thiyl Radical of C225-R1. *Journal of the American Chemical Society* **117**, 8908-8916, doi:DOI 10.1021/ja00140a003 (1995).

- 15 Salowe, S. *et al.* Alternative model for mechanism-based inhibition of Escherichia coli ribonucleotide reductase by 2'-azido-2'-deoxyuridine 5'-diphosphate. *Biochemistry* **32**, 12749-12760, doi:10.1021/bi00210a026 (1993).
- 16 Salowe, S. P., Ator, M. A. & Stubbe, J. Products of the inactivation of ribonucleoside diphosphate reductase from Escherichia coli with 2'-azido-2'-deoxyuridine 5'-diphosphate. *Biochemistry* **26**, 3408-3416, doi:10.1021/bi00386a024 (1987).
- 17 Bennati, M. *et al.* EPR distance measurements support a model for long-range radical initiation in E. coli ribonucleotide reductase. *J Am Chem Soc* **127**, 15014-15015, doi:10.1021/ja054991y (2005).
- 18 Ge, J., Yu, G., Ator, M. A. & Stubbe, J. Pre-steady-state and steady-state kinetic analysis of E. coli class I ribonucleotide reductase. *Biochemistry* **42**, 10071-10083, doi:10.1021/bi034374r (2003).
- 19 Eriksson, M. *et al.* Binding of allosteric effectors to ribonucleotide reductase protein R1: reduction of active-site cysteines promotes substrate binding. *Structure* **5**, 1077-1092 (1997).
- 20 Zimanyi, C. M., Chen, P. Y., Kang, G., Funk, M. A. & Drennan, C. L. Molecular basis for allosteric specificity regulation in class Ia ribonucleotide reductase from Escherichia coli. *Elife* **5**, e07141, doi:10.7554/eLife.07141 (2016).
- 21 Moriya, T. *et al.* High-resolution Single Particle Analysis from Electron Cryo-microscopy Images Using SPHIRE. *Jove-J Vis Exp*, doi:ARTN e55448 10.3791/55448 (2017).
- 22 Nordlund, P. & Eklund, H. Structure and function of the Escherichia coli ribonucleotide reductase protein R2. *J Mol Biol* **232**, 123-164, doi:10.1006/jmbi.1993.1374 (1993).
- 23 Zivanov, J. *et al.* New tools for automated high-resolution cryo-EM structure determination in RELION-3. *Elife* **7**, doi:ARTN e42166 10.7554/eLife.42166 (2018).
- 24 Bepler, T. *et al.* Positive-unlabeled convolutional neural networks for particle picking in cryo-electron micrographs. *Res Comput Mol Biol* **10812**, 245-247 (2018).
- 25 Afonine, P. V. *et al.* Real-space refinement in PHENIX for cryo-EM and crystallography. *Acta Crystallogr D Struct Biol* **74**, 531-544, doi:10.1107/S2059798318006551 (2018).
- 26 Zimanyi, C. M. *Structural Studies of Allosteric Regulation in the Class Ia Ribonucleotide Reductase from Escherichia coli* Ph.D. thesis, Massachusetts Institute of Technology, (2013).
- 27 Greene, B. L., Taguchi, A. T., Stubbe, J. & Nocera, D. G. Conformationally Dynamic Radical Transfer within Ribonucleotide Reductase. *J Am Chem Soc* **139**, 16657-16665, doi:10.1021/jacs.7b08192 (2017).
- 28 Ekberg, M. *et al.* Preserved catalytic activity in an engineered ribonucleotide reductase R2 protein with a nonphysiological radical transfer pathway. The importance of hydrogen bond connections between the participating residues. *J Biol Chem* **273**, 21003-21008, doi:10.1074/jbc.273.33.21003 (1998).

- 29 Salowe, S. P. & Stubbe, J. Cloning, overproduction, and purification of the B2 subunit of ribonucleoside-diphosphate reductase. *J Bacteriol* **165**, 363-366, doi:10.1128/jb.165.2.363-366.1986 (1986).
- 30 Kremer, J. R., Mastronarde, D. N. & McIntosh, J. R. Computer visualization of three-dimensional image data using IMOD. *J Struct Biol* **116**, 71-76, doi:DOI 10.1006/jsbi.1996.0013 (1996).
- 31 Grant, T. & Grigorieff, N. Measuring the optimal exposure for single particle cryo-EM using a 2.6 Å reconstruction of rotavirus VP6. *Elife* **4**, e06980, doi:10.7554/eLife.06980 (2015).
- 32 Tang, G. *et al.* EMAN2: an extensible image processing suite for electron microscopy. *J Struct Biol* **157**, 38-46, doi:10.1016/j.jsb.2006.05.009 (2007).
- 33 Zheng, S. Q. *et al.* MotionCor2: anisotropic correction of beam-induced motion for improved cryo-electron microscopy. *Nat Methods* **14**, 331-332, doi:10.1038/nmeth.4193 (2017).
- 34 Rohou, A. & Grigorieff, N. CTFFIND4: Fast and accurate defocus estimation from electron micrographs. *J Struct Biol* **192**, 216-221, doi:10.1016/j.jsb.2015.08.008 (2015).
- 35 Goddard, T. D. *et al.* UCSF ChimeraX: Meeting modern challenges in visualization and analysis. *Protein Sci* **27**, 14-25, doi:10.1002/pro.3235 (2018).
- 36 Emsley, P., Lohkamp, B., Scott, W. G. & Cowtan, K. Features and development of Coot. *Acta Crystallogr D* **66**, 486-501, doi:10.1107/S09074444910007493 (2010).

3.G Figures and Tables

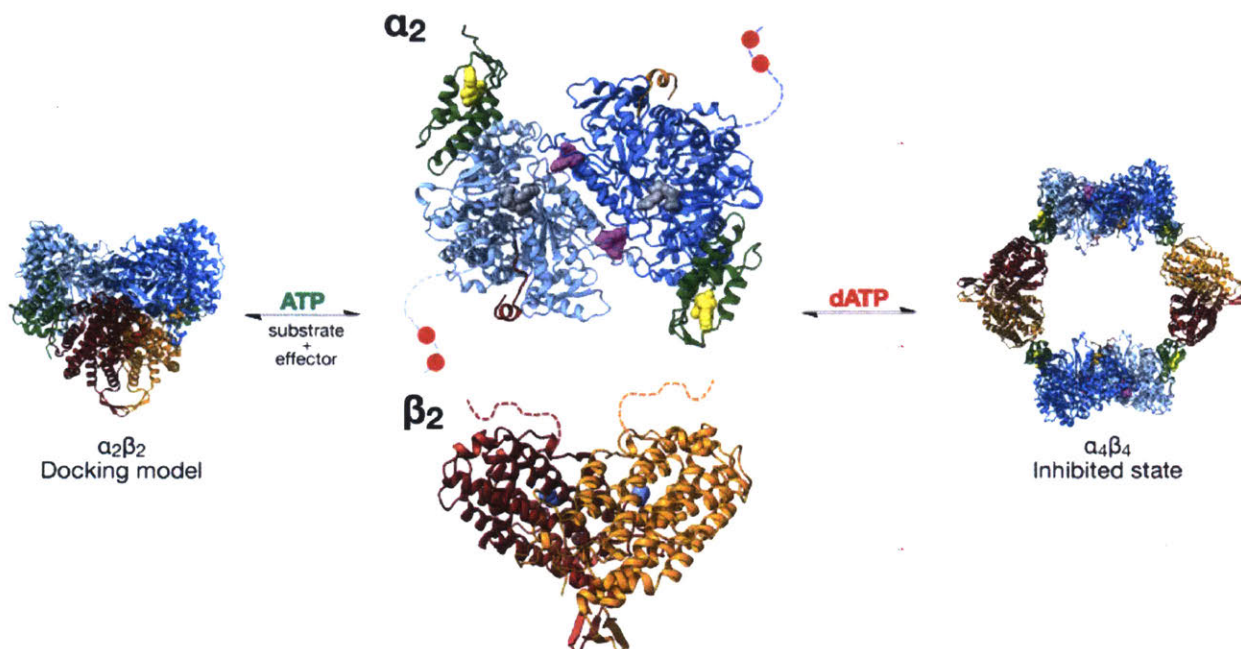


Figure 3.1: *E. coli* class Ia RNR is composed of α_2 and β_2 subunits. α_2 , shown in blue/cyan, houses the active site (substrate shown in grey spheres), an allosteric specificity site (effector shown in magenta spheres), and an N-terminal allosteric activity site, referred to as the “cone-domain” (cone-domain shown in green ribbon with activity effector dATP/ATP shown in yellow spheres). The disordered C-termini are shown in dotted lines with C754 and C759 indicated with red dots. β_2 is shown in orange/red, and the disordered C-termini shown in dotted lines. dATP binding to the cone-domain shifts the equilibrium towards an inhibited $\alpha_4\beta_4$ state, and its displacement by ATP restores activity by shifting the oligomeric state towards an active $\alpha_2\beta_2$ complex.

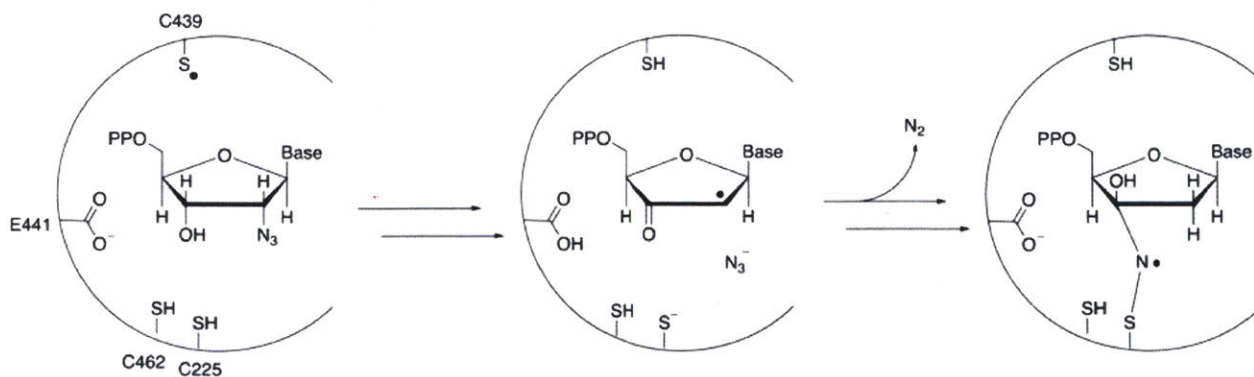


Figure 3.2: Reaction of N₃NDP with RNR. The incubation of N₃NDP with RNR results in the release of nitrogen gas accompanied by the formation of a nitrogen-centered radical species (N•) that is proposed to be covalently bound to the nucleotide via the 3'-carbon of the ribose as well as the thiol-moiety of C225 of α .

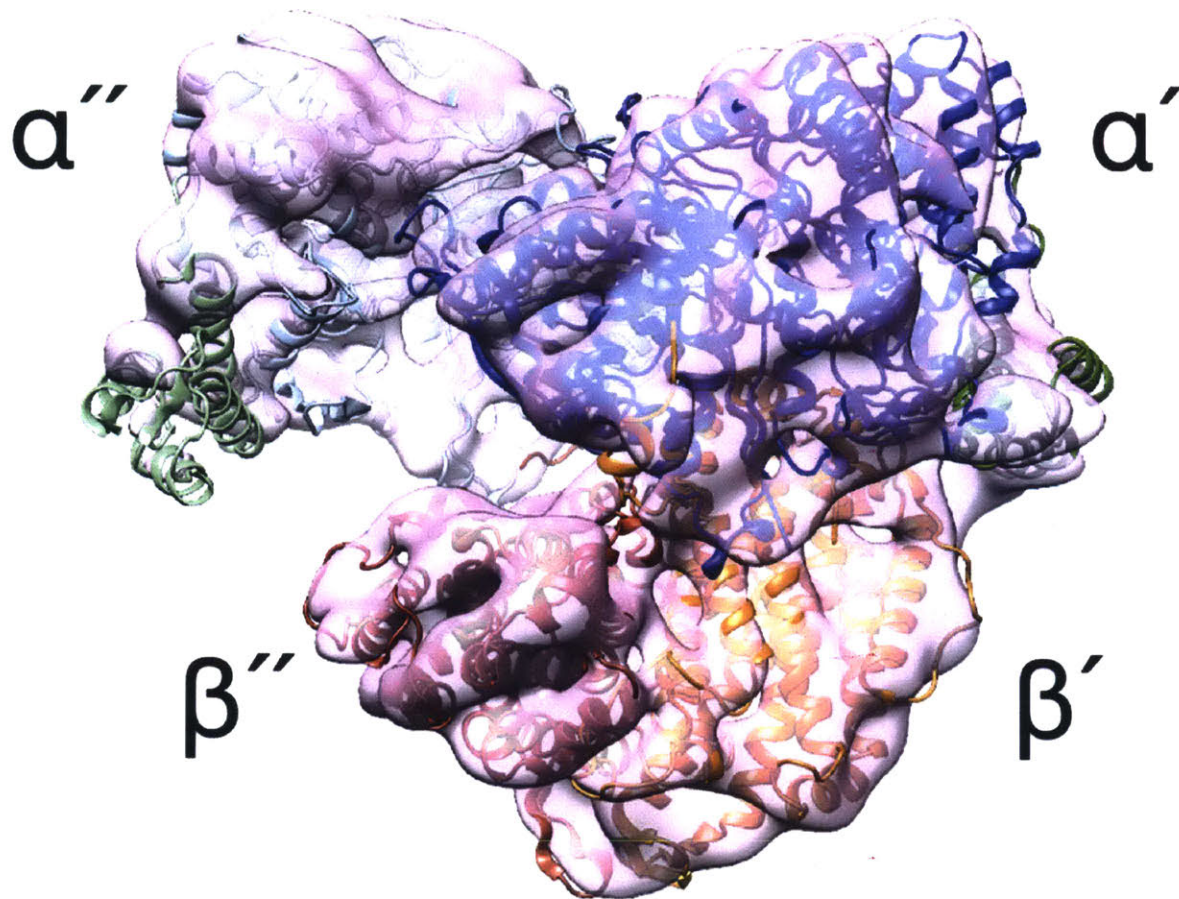


Figure 3.3: 8-Å resolution structure of WT- $\alpha_2\beta_2$ in the presence of N_3 UDP and ATP generated using the SPHIRE software suite. The $\alpha_2\beta_2$ complex is asymmetric with β_2 interacting with one α monomer. α' is shown in blue and α'' in light-blue with their conedomains shown in green and light-green, respectively. β' is shown in orange and β'' in red. Cryo-EM density is shown in transparent pink.

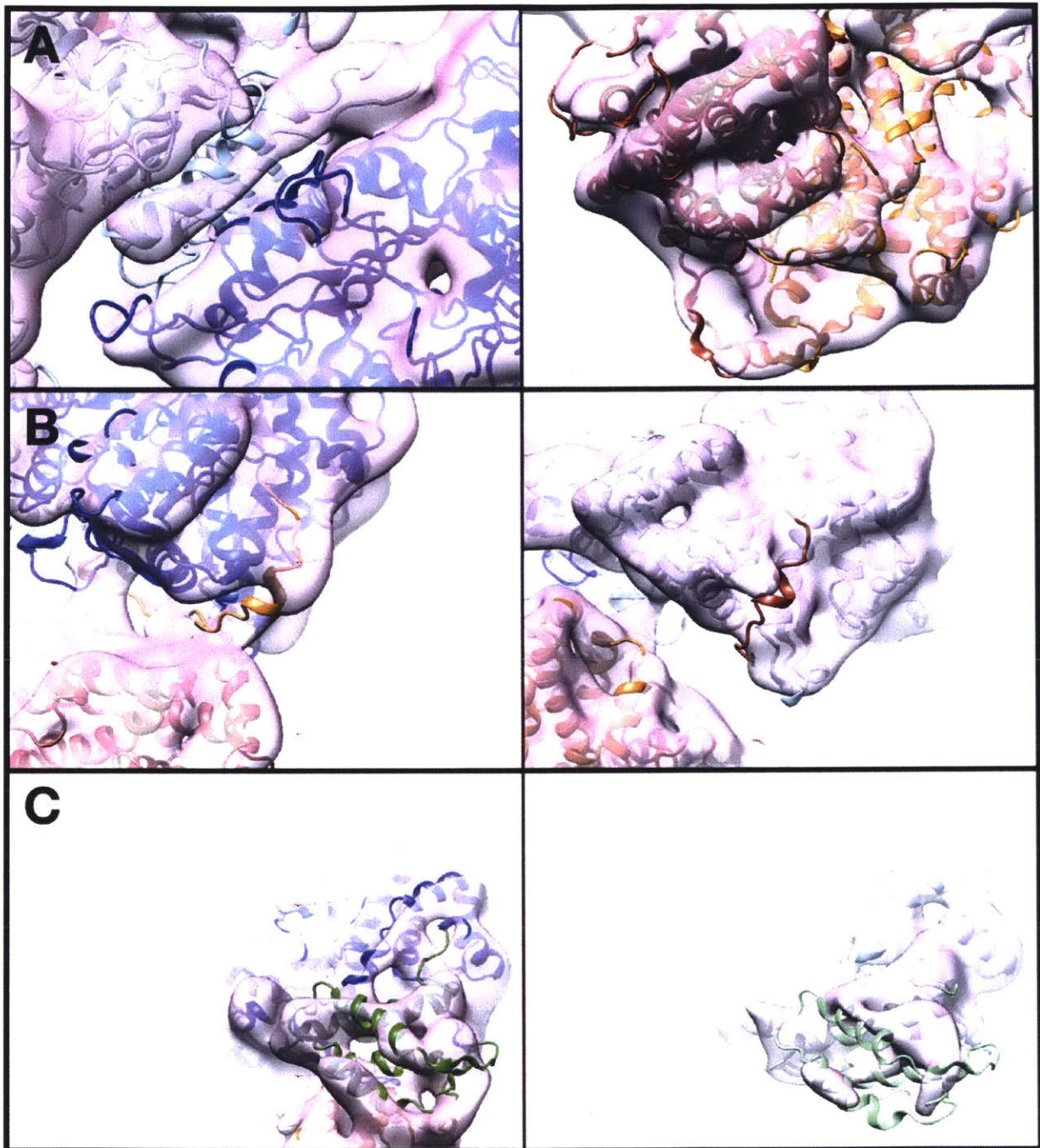


Figure 3.4: Key structural features of 8-Å resolution cryo-EM density. A) Secondary structural elements such as alpha helices begin to become apparent. Left shows the helix-bundle at the α' - α'' interface and right shows that the contouring of surface helices on the β_2 subunit are becoming visible. B) Only one of the two C-termini of the β_2 subunit have corresponding density. We observe density along α' (left) but not α'' (right). Although colored as part of β' , given the lack of density, the C-terminus cannot be assigned to a specific beta monomer at this resolution. C) The cone-domain of α' (left) is better ordered than that of α'' (right). Colors are as in Figure 3.3.

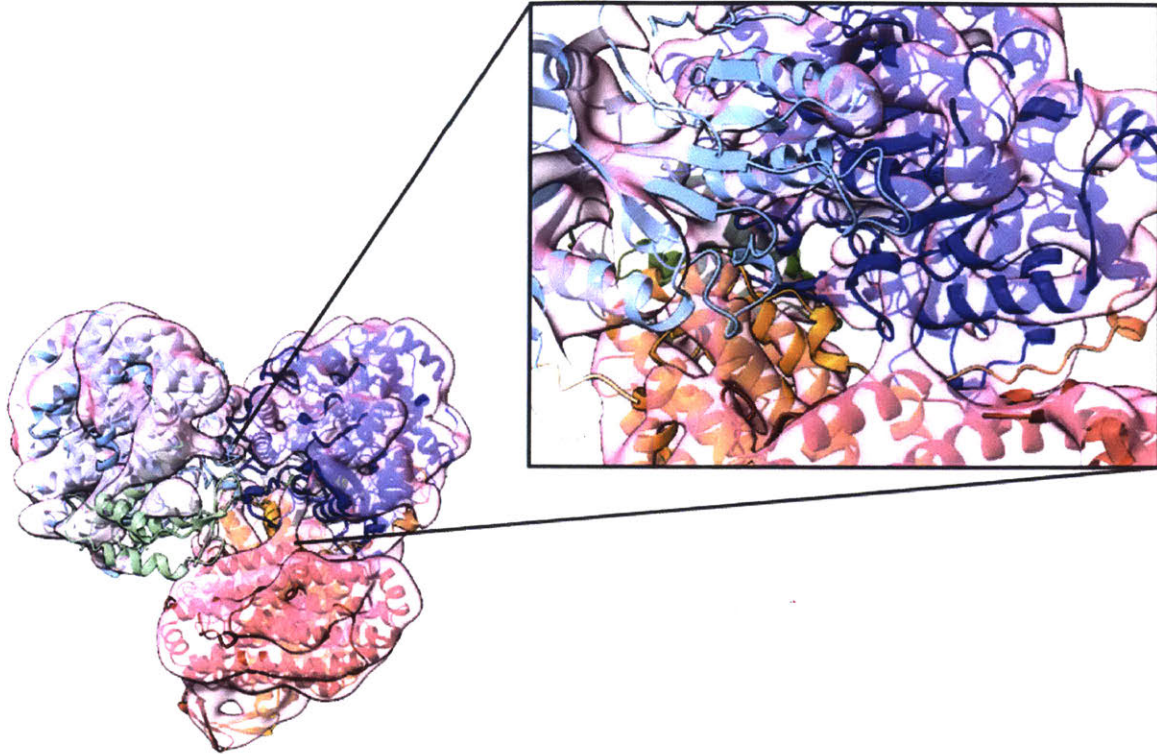


Figure 3.5: The α' - $\beta 2$ interface largely lacks cryo-EM density. At this resolution, we did not observe any cryo-EM density that could correspond to the 20 missing residues (342-362) of the $\beta 2$ subunit. Moreover, many parts of the docked crystal structures, including loop and helices, could not be modeled into any available density.

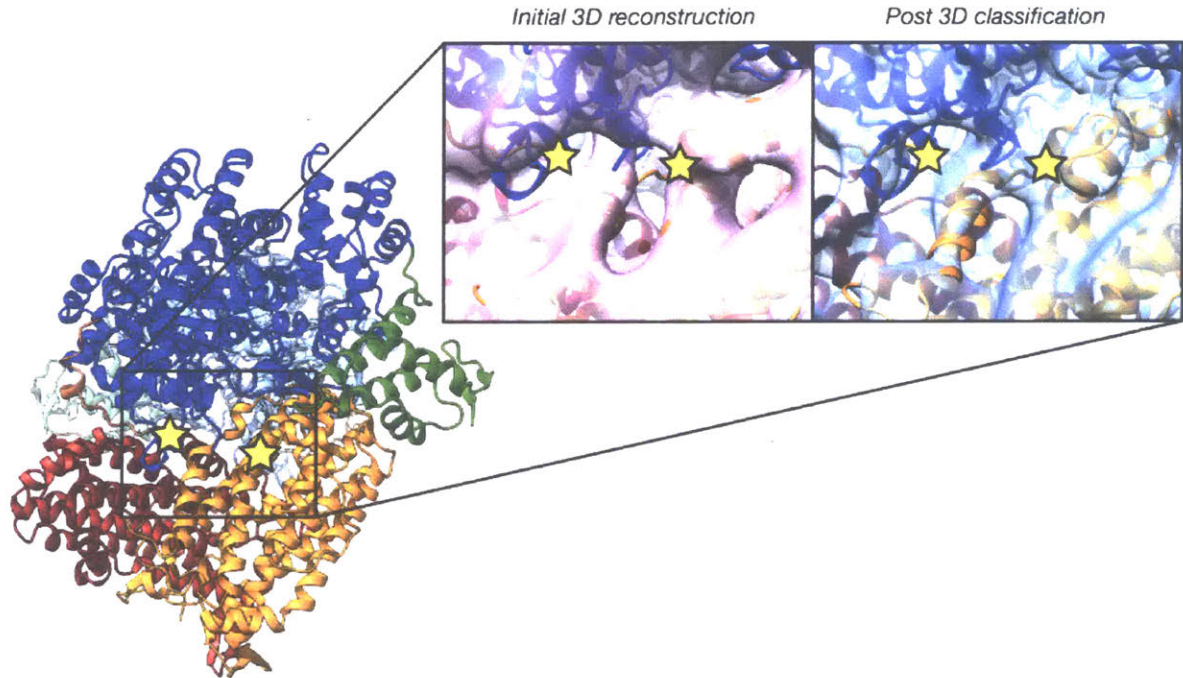


Figure 3.6: 3D classification reveals additional density at the α' - β_2 interface. The left and right stars denote residues 360 of the beta C-terminal peptide and 340 of β' , respectively. In the initial 3D reconstruction shown in the left zoomed panel (pink density), we observe no cryo-EM density between the two highlighted residues. Following 3D classification shown in the right zoomed panel (blue density), we observe the appearance of additional cryo-EM density in this region, although we are not able to structurally model any additional residues given the resolution.

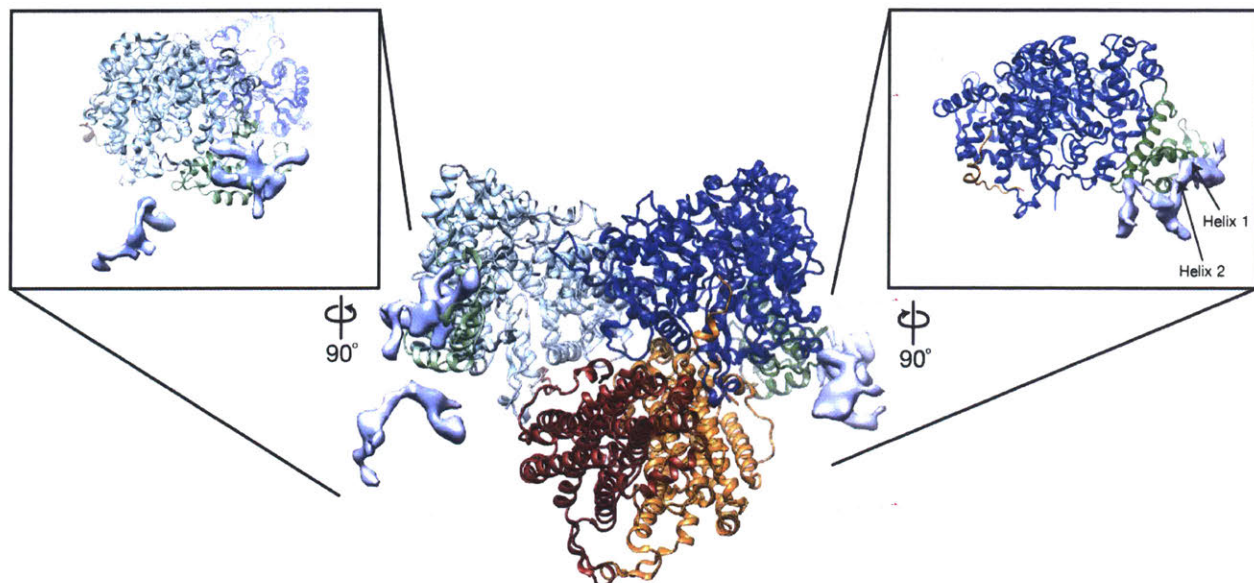


Figure 3.7: 3D variance reveals regions of relative structural heterogeneity. We observe two regions of higher structural variance corresponding to α'' and one region corresponding to α' . The two regions associated with α'' are near the C-terminus (residue 737) and within the cone-domain. The region in α' is found along the cone-domain, specifically adjacent to helices 1 and 2 (residues 20-48). Boxed panels are rotated 90° counter-clockwise (left box) and clockwise (right box) from the point of view of the structure shown in the middle.

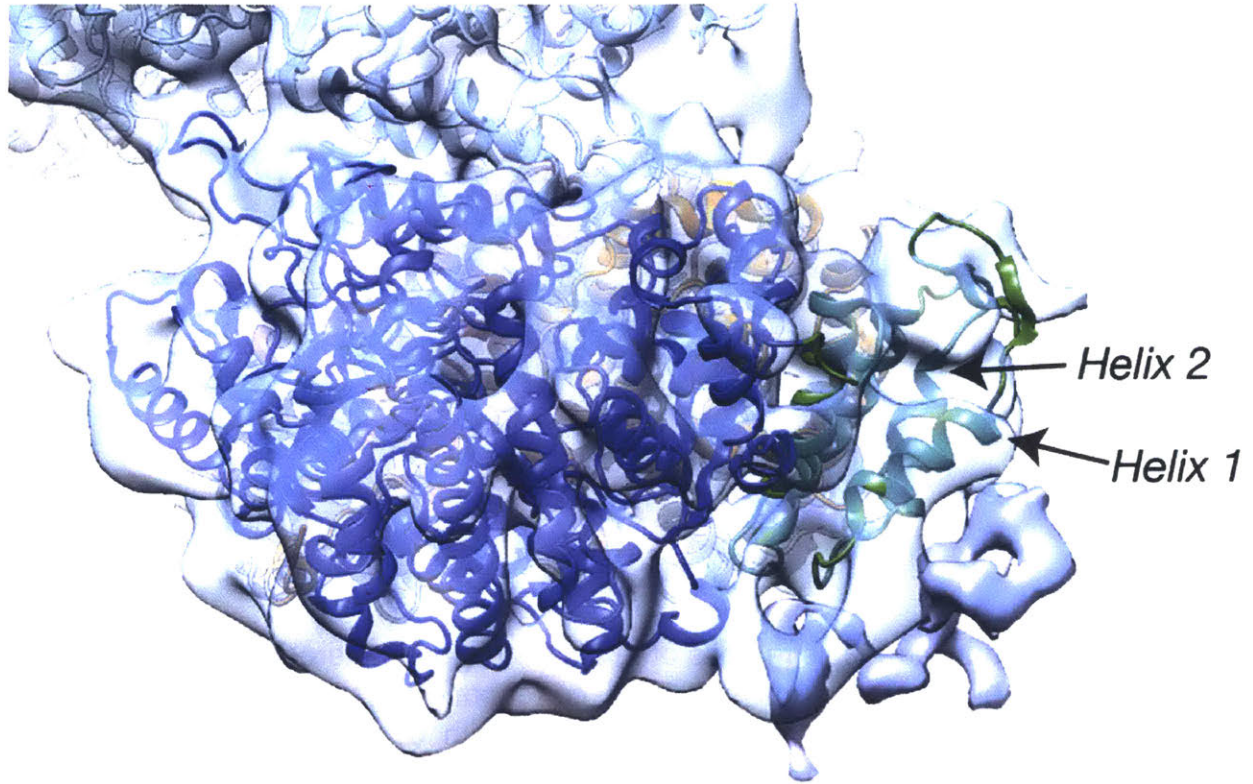


Figure 3.8: Overlay of results from 3D variance and classification at the cone-domain of α' . The extra density observed at the cone-domain of α' in the output of 3D classification aligns closely to the position of the density observed in 3D variance analysis. Density from 3D classification is shown in transparent blue and density from 3D variance is shown in solid blue.

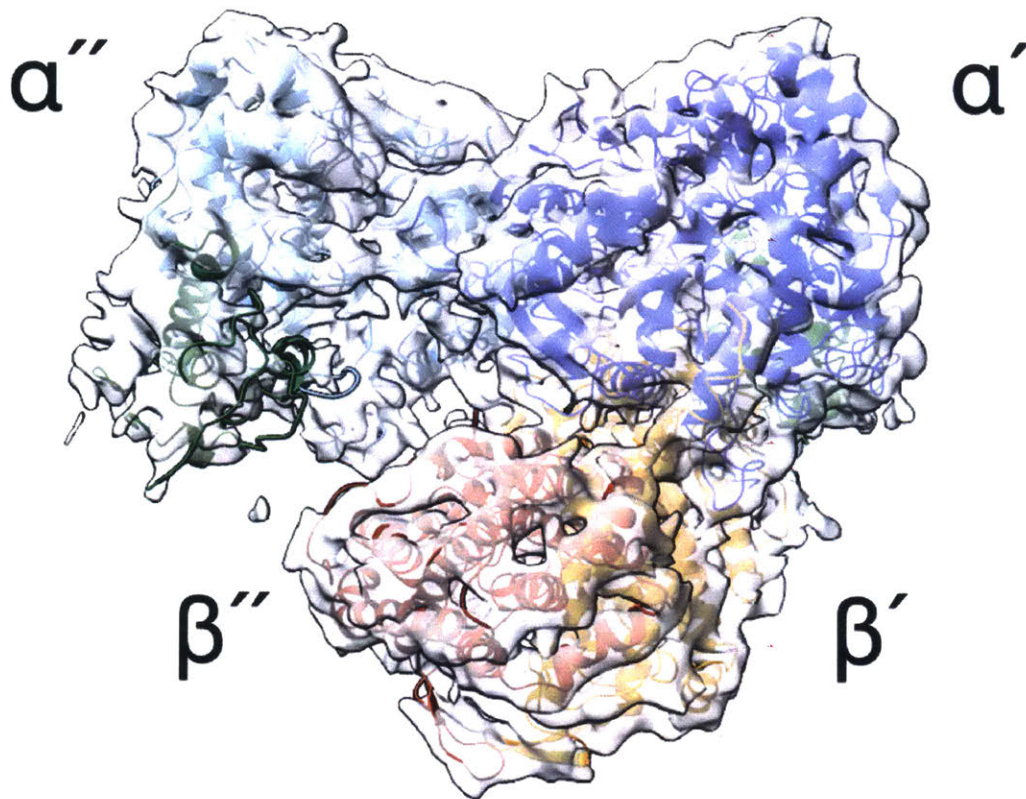


Figure 3.9: 5-Å resolution structure of WT- $\alpha 2\beta 2$ in the presence of N_3 UDP and ATP generated using Relion 3.0. α' is shown in blue and α'' in light-blue with their respective N-terminal cone-domains shown in green. β' is shown in orange and β'' in red. The cryo-EM density is shown in transparent grey.

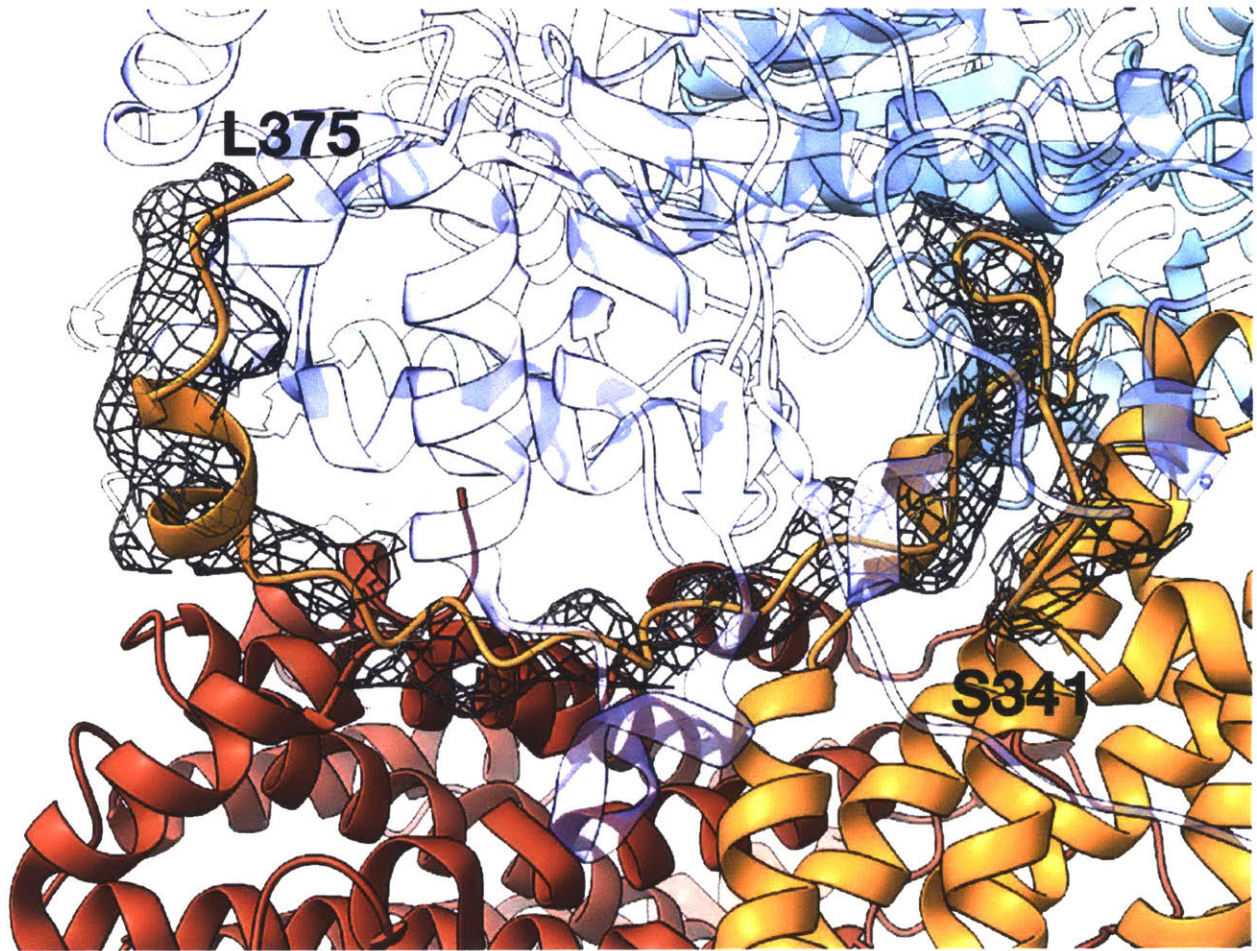


Figure 3.10: Full-length of C-terminus of β' of N_3 UDP- $\alpha_2\beta_2$ is observed by cryo-EM density. When the structure of E52Q/F₃Y- $\alpha_2\beta_2$ is docked into the re-processed cryo-EM density, we observe that the structure of the C-terminus of β' fits the observed density well.

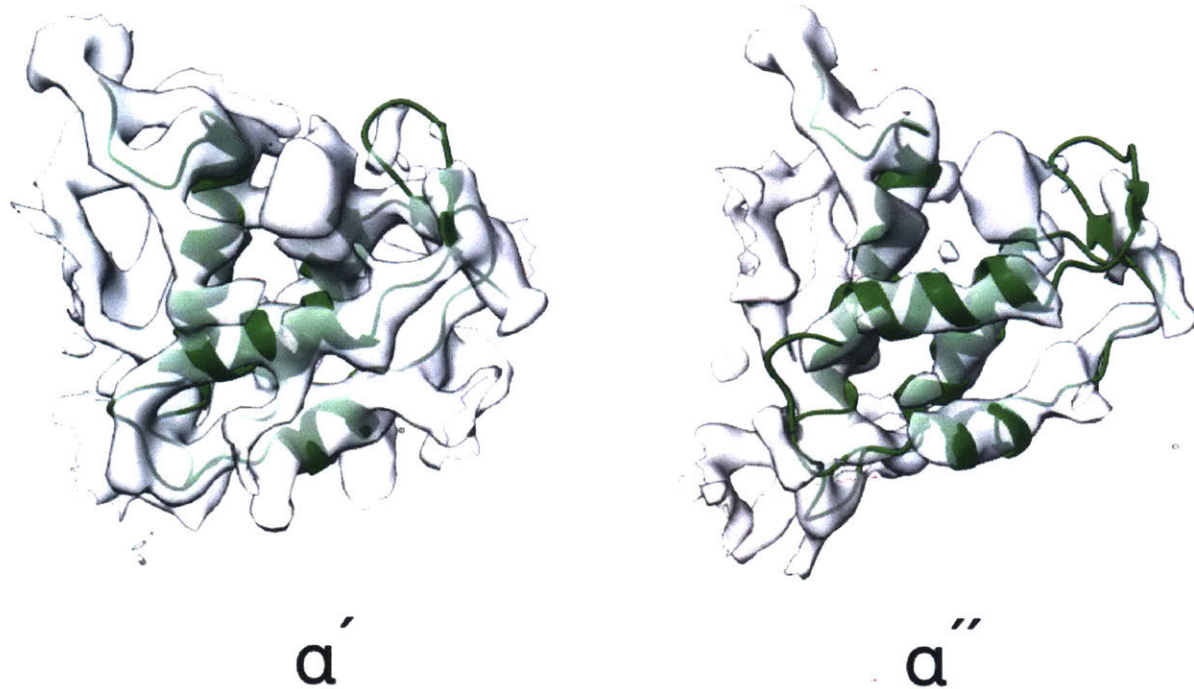


Figure 3.11: Both cone-domains of $\alpha 2$ in N_3 UDP- $\alpha 2\beta 2$ are ordered. The presence of 3 mM ATP in our reaction conditions leads to both cone-domains of $\alpha 2$ being structurally ordered. The cone-domain of α'' appears to have weaker cryo-EM density relative to the cone-domain of α' , which interacts with $\beta 2$. This suggests that the interaction with $\beta 2$ affords additional structural stability for the cone-domain beyond that provided by ATP binding. The cryo-EM density is shown in transparent grey and was visualized at the same contour threshold level (0.028) in ChimeraX.

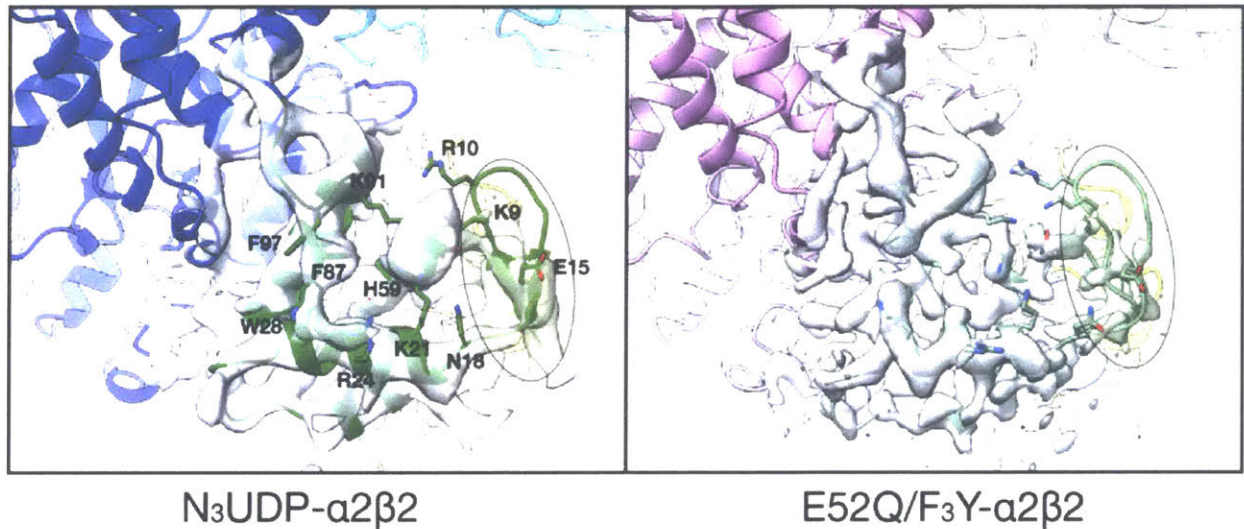


Figure 3.12: Extra density at the cone-domain of α' in N₃UDP- α ₂β₂ relative to that of E52Q/F₃Y- α ₂β₂. Residues previously identified as interacting with ATP in the cone-domain are labeled. Additional density near the side-chains of K9, K21, and K91, which we suspect corresponds to ATP, is observed in the case of N₃UDP- α ₂β₂ that is absent in E52Q/F₃Y- α ₂β₂, which contained no ATP in sample preparations. Further, we observe additional cryo-EM density corresponding to the β -sheet of the N-terminal hairpin loop in N₃UDP- α ₂β₂ relative to E52Q/F₃Y- α ₂β₂. Residues located on this hairpin loop, including K9 and R10, are known to interact with the phosphates of the activity effector (dATP or ATP). The hairpin loops are outlined and highlighted in transparent green. N₃UDP- α ₂β₂ is shown in blue/green and E52Q/F₃Y- α ₂β₂ in pink/light-green.

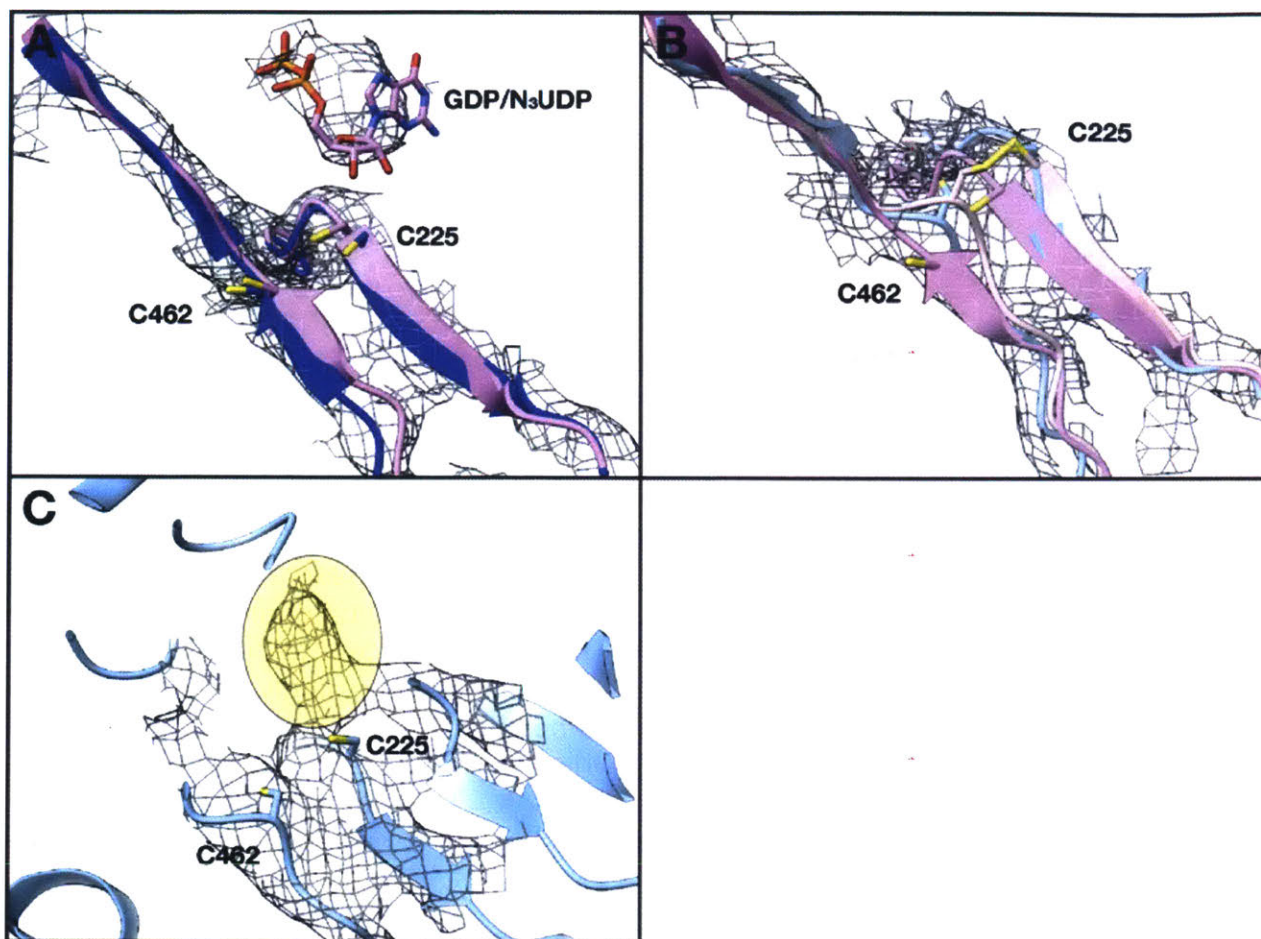


Figure 3.13: Active sites of α' and α'' in $N_3UDP-\alpha_2\beta_2$ compared to $E52Q/F_3Y-\alpha_2\beta_2$. α' and α'' of $N_3UDP-\alpha_2\beta_2$ are shown in blue and light-blue, respectively. α' and α'' of $E52Q/F_3Y-\alpha_2\beta_2$ are shown in pink and light-pink, respectively. $N_3UDP-\alpha_2\beta_2$ density shown in grey mesh. A) Alignment of $N_3UDP-\alpha_2\beta_2$ α' and $E52Q-F_3Y-\alpha_2\beta_2$ α' with cryo-EM density corresponding to $N_3UDP-\alpha_2\beta_2$ α' . C225 and C462 of $N_3UDP-\alpha_2\beta_2$ α' align well with their counterparts in $E52Q/F_3Y-\alpha_2\beta_2$ α' , suggesting they are in the reduced state. As highlighted by the docked GDP, we also observe density in the substrate binding site, which we assume is bound N_3UDP . B) Alignment of $N_3UDP-\alpha_2\beta_2$ α'' , $E52Q/F_3Y-\alpha_2\beta_2$ α' , and $E52Q/F_3Y-\alpha_2\beta_2$ α'' with cryo-EM density corresponding to $N_3UDP-\alpha_2\beta_2$ α'' . We find that the position of C225 of $N_3UDP-\alpha_2\beta_2$ α'' aligns well with the position of C225 in $E52Q/F_3Y-\alpha_2\beta_2$ α'' (i.e. in the oxidized position). Interestingly, the position of C462 of $N_3UDP-\alpha_2\beta_2$ α'' is more ambiguous, as it refines to a position somewhere between C462 in the oxidized and reduced states found in $E52Q/F_3Y-\alpha_2\beta_2$. C) We observe additional cryo-EM density adjacent to C225 in α'' of $N_3UDP-\alpha_2\beta_2$, highlighted in transparent yellow. Interestingly, the reaction of N_3NDP is proposed to proceed through a transient covalent adduct to C225. This density is absent in the structure of $E52Q/F_3Y-\alpha_2\beta_2$, which utilized natural substrate GDP.

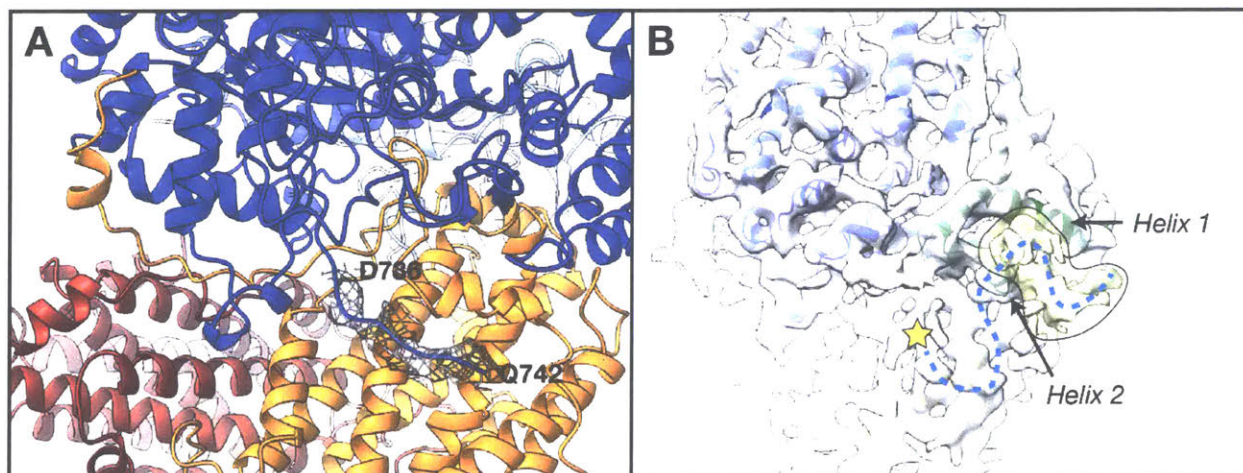


Figure 3.14: Additional cryo-EM density corresponding to C-terminus of alpha subunit. Left panel: Similar to the structure of E52Q-F₃Y- α 2 β 2, we observe cryo-EM density extending out to residue ~742 of α' . Right panel: At higher contouring levels for the density map, we also observe additional cryo-EM density adjacent to helices 1 and 2 of the cone-domain of α' , highlighted in yellow transparency. Interestingly, this is the same location where we observed additional density in both the 3D variance and classification analyses performed in SPHIRE (**Figure 3.8**), which we suspect may correspond to part of the structurally uncharacterized C-terminus of α . The yellow star indicates the position of Q742 of α' with the blue dotted line showing a possible path through the extra density along the cone-domain.

Table 3.1 RMSD values between equivalent chains from N₃UDP- α 2 β 2 and E52Q-F₃Y- α 2 β 2

Chain from N ₃ UDP- α 2 β 2	Chain from E52Q/F ₃ Y- α 2 β 2	RMSD (# residues)
α'	α'	1.03 Å (738 residues)
α''	α''	1.49 Å (736 residues)
β'	β'	0.93 Å (375 residues)
β''	β''	0.87 Å (341 residues)

Table 3.2

Imaging parameters and 3D Reconstruction	
Acceleration voltage (kV)	300
Magnification (X)	81,000
Pixel size (Å)	1.35
Number of frames	50
Exposure time (s)	15
Total exposure (e ⁻ / Å)	82.3
Particles	
Micrographs used for selection	1582
Defocus range (um)	1.5-3.0
Windowed	~270,000 (SPHIRE), ~216,000 (Relion)
In final 3D reconstruction	98,234 (SPHIRE), 85,753 (Relion)
Resolution	
'Gold-standard' at FSC 0.143 (Å)	5.0

Chapter 4

Class Ia RNR from T4 bacteriophage forms filaments composed of both α_2 and β_2

We thank Dr. Yifeng Wei and Dr. Wankyu Lee for providing all protein samples of T4 bacteriophage class Ia RNR. We thank Dr. Chen Xu and Dr. Mike Rigney for providing electron microscope instrument training for data screening and collection at the W.M. Keck Institute for Cellular Visualization at Brandeis University. Dr. Ed Brignole generated the initial filament reconstruction solved in the presence of dATP and CDP.

4.A Summary

Ribonucleotide reductase (RNR) is the only known enzyme capable of *de novo* generation of deoxynucleotides from their nucleotide counterparts and can remarkably reduce all four nucleotide substrates. In order to maintain the proper balance of nucleotides, RNR is under careful allosteric regulation where the identity of deoxynucleoside triphosphate (dNTP) binding to a remote site dictates substrate specificity. Class I RNRs are composed of two homodimeric subunits α_2 and β_2 . Some class I RNRs are under a second form of allosteric regulation that controls overall activity. Typically, dATP binding to this activity site inhibits enzymatic activity, whereas ATP can restore activity. The class Ia RNR from *E. coli* is one such RNR that is responsive to activity regulation and forms an inactive $\alpha_4\beta_4$ complex in the presence of dATP. The class Ia RNR from T4 bacteriophage shares high sequence identity to its host *E. coli* RNR yet was observed to not be inhibited by dATP and to exhibit tighter binding between its respective α_2 and β_2 subunits. As such, we initially approached the T4 RNR as a candidate for obtaining a structure of the active $\alpha_2\beta_2$ complex. Unexpectedly, the T4 RNR formed filaments in the presence of either dATP or ATP composed of both subunits, and the conformation of α_2 and β_2 within the filaments suggest that they are of an inactive form.

4.B Introduction

Ribonucleotide reductases (RNRs) catalyze the reduction of all four nucleotides (U,C,A,G) to their deoxynucleotide counterparts, thus playing a critical role in maintaining not only the overall amounts of deoxynucleotides but also the balance between them¹. The class Ia RNR from *Escherichia coli* has been the prototype for studying RNR mechanism and regulation since its discovery in the late 1960s and continues to reveal surprising insights into the process of ribonucleotide reduction today^{2,3}. The class I RNRs are composed of two homodimeric subunits, commonly referred to as α 2 and β 2². α 2 is the catalytic subunit that houses the nucleotide binding sites: the active site, an allosteric specificity site⁴, and depending on the subclass and organism, an N-terminal activity site (a four-helix bundle, referred to as the cone-domain) that acts as an enzymatic “on-off” switch⁵. If an activity site is present, dATP and ATP binding typically inactivate and restore enzymatic activity, respectively⁶. β 2 houses the radical cofactor that transiently oxidizes a conserved active site cysteine to generate a thiyl-radical that in turn initiates nucleotide reduction⁷. The active state of the enzyme was first proposed to be a tight, symmetric α 2 β 2 complex^{4,8} and we have now shown that it is indeed a tight α 2 β 2 complex, but asymmetric (discussed in Chapters 2 and 3).

The oligomeric states of class I RNRs are dynamic as well as diverse. The dATP-induced inhibited form of the *E. coli* class Ia RNR was revealed to be an α 4 β 4 ring complex of repeating α 2 and β 2 units that precludes oxidation of the active site cysteine by the radical cofactor in β 2⁹. Despite being members of the same subclass, the inhibited state of the human RNR was found to be an α 6 ring that physically prevents β 2 from interacting with α 2 to form an interface capable of performing chemistry¹⁰. More recently, it was reported that the inhibited state of the *Bacillus subtilis* RNR, a member of the class Ib subclass, forms helical filaments¹¹. Although the different modes of inhibitory regulation in different RNRs is in itself an interesting question, it has also led to challenges in structurally studying the active state of the enzyme as wildtype RNR is

always in a dynamic state of equilibrium between its active, inactive, and free-subunit states⁶.

Our initial interest in the class Ia RNR from T4 bacteriophage arose from our efforts to obtain the structure of the active $\alpha_2\beta_2$ complex of *E. coli* class Ia RNR, which at the time had not yet been solved. It was found that when *E. coli*, the natural host for T4 bacteriophage, was infected with the virus, it led to the isolation of a highly similar (>70% similarity, >50% identity) RNR, also composed of α_2 and β_2 , to its host¹²⁻¹⁴. Further, although its sequence indicated the presence of an N-terminal activity site, the T4 RNR appeared to be insensitive to dATP-induced inhibition, as is observed with its host RNR¹³. The α_2 - β_2 interaction also appeared tighter in the T4 enzyme relative to its *E. coli* counterpart¹⁵. These observations lead us to speculate at the time that we may be able to circumvent the typical challenges that are associated with the RNR forming an inhibited state when trying to study the active state.

To our surprise, the T4 bacteriophage class Ia RNR formed filaments of repeating $\alpha_2\beta_2$ units in the presence of either dATP or ATP, and substrate CDP, observable by negative-stain electron microscopy (EM). Generating a 3D reconstruction of the filaments revealed the relative orientation between α_2 and β_2 found in the filaments is most likely of an inactive state, based on the lack of a tight interface between the two subunits. We are currently pursuing a high-resolution structure of the filaments using cryo-EM in hopes of elucidating the molecular details and the role nucleotide binding may be playing in filament formation.

4.C Results

T4 class Ia RNR is less soluble than its E. coli counterpart

Early attempts to crystallize the T4 enzyme in the presence of both $\alpha 2$ and inactivated met- $\beta 2$ were unsuccessful due to issues regarding solubility compared to the *E. coli* class Ia RNR under identical conditions (e.g. 1 mM dATP, 1mM CDP, 15 mM MgCl_2 , 30 mM TRIS pH 7.6). Further investigation revealed that the specific addition of dATP, CDP, and MgCl_2 lead to protein precipitation in solution. Lowering the concentration of MgCl_2 from 15 mM to 5 mM temporarily slowed down aggregation, but precipitate formation would be observed over time.

T4 enzyme forms helical filaments under “inactivating” conditions

To explore how the observed precipitation may be playing out at the protein level, we prepared negative-stain electron microscopy (EM) grids with $\alpha 2$ and $\beta 2$ (1:1) in the presence of 1 mM CDP, 1 mM dATP, and 5 mM MgCl_2 , conditions that are known to inhibit *E. coli* class Ia RNR^{6,8}. Upon imaging the prepared grids, we observed a significant population of filaments of varying lengths, in stark contrast to the $\alpha 4\beta 4$ rings observed with *E. coli* class Ia RNR under similar conditions⁹ (**Figure 4.1**). We also observed a significant quantity of single particle species among the filaments, but further analysis is required to determine the subunit composition of the free particles. Further, the removal of nucleotides or magnesium leads to inability of the enzyme to form filaments (**Figure 4.2**). Finally, the filaments did not form in the absence of $\beta 2$, suggesting they are composed of both subunits.

Negative-stain reconstruction reveals helix composed of repeating $\alpha 2\beta 2$ units

Approximately 500 filaments were manually identified from 40 micrographs leading to a 20-Å resolution 3D reconstruction. As crystal structures of the T4 subunits are unavailable, crystal structures of the $\alpha 2$ and $\beta 2$ subunits^{16,17} (PDB 4R1R 1RIB,

respectively) from *E. coli* class Ia RNR were used as proxies, given their high sequence similarity, to dock into the EM density, which revealed that the repeating unit was composed of both $\alpha 2$ and $\beta 2$. The rise and rotation per repeating helical unit were ~ 75 Å and $\sim 56^\circ$, respectively. (**Figure 4.3**)

From the docked structures of *E. coli* RNR, we tried to identify possible regions of interaction between different subunits that could contribute to filament formation. Based on proximity, two sets of possible interacting regions were identified. The first was between a helix formed by residues 332-340 of β and helices 1 and 2 of the cone-domain of the $\alpha 2$ (residues 20-48) from the preceding helical unit. The second was between a β -strand formed by residues 390-395 of $\alpha 2$ and the β -hairpin formed by residues 1-16 of the cone-domain of the $\alpha 2$ of the preceding helical unit (**Figure 4.4**).

Orientation between $\alpha 2$ and $\beta 2$ in helical unit is rotated with respect to docking model

Docking the structures of *E. coli* $\alpha 2$ and $\beta 2$ into the helical density, we observe that $\beta 2$ in the helix is rotated approximately 90° with respect to $\beta 2$ in the symmetric “docking model” relative to $\alpha 2^4$ (**Figure 4.5**), and is thus unable to form a tight complex in this orientation. As a result, the distances between Y122 in $\beta 2$ and Y730 in $\alpha 2$ for the direct and diagonal pairs were measured to be 44-46 Å and 55-58 Å. In contrast, the docking model predicted the direct and diagonal distances for the same pairs of residues to be ~ 37 Å and ~ 40 Å, respectively. (**Figure 4.6**).

ATP in place of dATP does not affect filament quaternary structure

Next, we wanted to explore whether the formation of filaments was dependent on the presence of the higher concentrations of dATP we had been using (1 mM). Towards answering this question, negative-stain EM grids were prepared in the presence of dATP (1 mM or 175 μ M) or ATP (3 mM). The concentrations were chosen based on their respective cellular concentrations in *E. coli*¹⁸. In all three cases, we observed

approximately the same amount of filament formation (**Figure 4.7**), suggesting they were not dependent on the presence of dATP.

Further, a 3D reconstruction was generated of the filaments formed in the presence of ATP, and at their current resolution, there was no discernable difference between the filaments formed in the presence of either nucleotide (**Figure 4.8**).

4.D Discussion

Our initial interest in studying the class Ia RNR from T4 bacteriophage arose from observations that the α 2- β 2 interaction is tighter than its *E. coli* counterpart and that its activity did not appear to be affected by dATP, which we interpreted as possibly being able to circumvent the formation of an inhibited state^{13,15}. Given these observations, and its high sequence identity to its host RNR, we believed the T4 class Ia RNR to be a potential alternative to obtaining a structure of the α 2 β 2 active complex, which at the time had yet to be solved. Our early run-in with solubility issues lead to the realization that the T4 RNR was forming filaments in solution and our observation that the filaments only form in the presence of both α 2 and β 2, substrate, effector, and magnesium suggested to us that they may be a relevant form of the enzyme.

A big caveat to our analysis and discussion is that high-resolution structures of the T4 phage class Ia RNR subunits are unavailable. Given their high sequence identity, we decided to use the subunit structures from *E. coli* class Ia RNR as proxies, which fit well into the EM density. Based on this docking, it appears that both the α 2 and β 2 subunits may be contributing to interactions that stabilize filament formation (**Figure 4.4**). Recently, filament formation was reported in the class Ib RNR from *B. subtilis*, that also contained both α 2 and β 2 (NrdE and NrdF, respectively)¹¹. In the *B. subtilis* class Ib RNR, filament formation appeared mainly driven by interactions between repeating α 2 units, specifically at their partial cone-domains. Although density corresponding to β 2/NrdF was observed at high occupancy in the *B. subtilis* filaments, it was thought to be flexibly linked to NrdE via its C-terminus and thus lead to lower resolution for the NrdF core relative to NrdE. In the T4 filament negative-stain reconstruction, the density for α 2 and β 2 seem equally well resolved, and could potentially be due to additional stabilizing interactions between α 2 and β 2 that are not present in the filaments formed by the class Ib enzyme. The T4 α 2- β 2 interaction is likely further enhanced by the C-terminus of β 2 interacting with α 2, as has been repeatedly observed in the *E. coli* class Ia enzyme^{4,19,20}, as well as the *B. subtilis* class Ib filaments discussed above.

All of our initial experiments were performed in the presence of CDP and dATP (1 mM or 175 μ M, traditionally inhibiting conditions for *E. coli* RNR⁶), and we thus suspected that the filaments may be an inhibited form of the enzyme, despite previous biochemical studies suggesting the T4 class Ia RNR was not susceptible to negative activity regulation by dATP. This hypothesis was reinforced by our observation that the interface formed between α 2 and β 2 in each helical unit was not a tight interaction, as is most likely necessary for radical transfer. Surprisingly, ATP (3 mM) in place of dATP lead to no noticeable difference at the micrograph level with respect to filament formation. Further, a 3D reconstruction of the filaments formed in the presence of ATP aligned remarkably well with a reconstruction of filaments formed in the presence of dATP. In the case of the *E. coli* enzyme, dATP and ATP can both bind to the N-terminal activity site (cone-domain) of α 2, but only dATP binding causes oligomerization into the inactive state^{6,21}. A higher-resolution structure, currently being pursued by cryo-electron microscopy, is necessary to determine whether and how dATP and ATP are contributing to filament formation in the T4 enzyme. In addition, under all conditions where we observe filaments, we also observe a significant population of single particles. Their subunit compositions are currently unknown and further analysis needs to be pursued.

The diversity of oligomeric states formed through interactions involving the cone-domain in different class I RNRs is remarkable. In the class Ia *E. coli* RNR, the dATP-bound cone-domain interacts with β 2 to form an inhibited α 4 β 4 ring⁹. In the human and *S. cerevisiae* class Ia RNRs, the cone-domains are involved in the formation of α 6 rings^{10,22}. The class Ib RNR from *B. subtilis* has a partial cone-domain that plays a role in filament formation¹¹, and based on our predicted docking of the *E. coli* structures, we believe the cone-domain of the T4 enzyme may be playing a structural role in filament formation as well. Currently limited by resolution, we hope further studies and higher-resolution structures will go towards elucidating the molecular basis of filament formation in T4 class Ia RNR.

4.E Materials and Methods

Protein preparation

T4 bacteriophage class Ia $\alpha 2$ and inactivated (met) $\beta 2$ were provided by Yifeng Wei and Wankyu Lee in the Stubbe lab and were prepared as described, respectively²³⁻²⁵. The concentrations of $\alpha 2$ and $\beta 2$ were determined using their respective extinction coefficients (A280) of 258 and 139 $\text{mM}^{-1}\text{cm}^{-1}$, respectively. All concentrations are for the respective dimers. Nucleotides were purchased from Sigma-Aldrich and prepared in 30 mM TRIS-HCl pH 7.5, 15 mM MgCl_2 , 1 mM EDTA. Nucleotide concentrations were determined using their respective extinction coefficients of 9.1 $\text{mM}^{-1}\text{cm}^{-1}$ at A271 for CDP, 15.4 $\text{mM}^{-1}\text{cm}^{-1}$ at A259 for ATP, 15.2 $\text{mM}^{-1}\text{cm}^{-1}$ at A259 for ATP.

Grid preparation

For all grid preparations, $\alpha 2$ and $\beta 2$ were each present at 60 nM, prepared in 30 mM TRIS-HCl, pH 7.5, and 1 mM TCEP. The concentration of MgCl_2 was varied between 0 and 5 mM, ATP at 0 or 3 mM, dATP at 0, 175 μM , or 1 mM, and CDP at 0 or 1 mM. 300 mesh continuous carbon grids will glow-discharged for 1 minute at -15 mA before applying 5 μL of protein solution and incubating for 1 minute. Protein solution was removed with Whatman #1 filter paper and stained 3x with 2% uranyl-acetate (5 μL each).

Data imaging and collection

All screening of grid conditions were done on a Tecnai T12 BioTWIN microscope at the W.M. Keck Microscopy Facility in the Whitehead Institute, MIT imaged at 80 kV.

The data set of the sample prepared in the presence of 1 mM dATP and 1 mM CDP was collected at the W.M. Keck Microscopy Facility in the Whitehead Institute, MIT. 115 micrographs were manually collected at a magnification of 68,000x with a pixel size of

2.55 Å, imaged at 80 kV. Stage was manually shifted and focus was reset using live FFT for each individual micrograph and defocus was set to -0.7 μm prior to each image being collected. Images were collected adjacent to the focus area to avoid excess radiation damage.

The data set of the sample prepared in the presence of 3 mM ATP and 1 mM CDP was collected at the W.M. Keck Institute for Cellular Visualization at Brandeis University. The grids were imaged at 200 kV on a Tecnai F20 electron microscope equipped using SerialEM²⁶ at a magnification of 50,000x with a pixel size of 2.22 Å. 152 total images were collected at a defocus of -0.7 μm using SerialEM's automated collection protocol.

Particle selection and map generation

Using the GUI for `sxheliboxer.py`²⁷, 571 unique filaments were identified from 39 of the 115 collected micrographs. 256-pixel segments (corresponding to ~650 Å) were windowed for particle alignment. Initial results from 2D classification generated using `sxali2d.py`²⁸ were used to estimate that one full helical turn was approximately 176 pixels (~450 Å) and contains ~6 helical "units." This led to an initial estimation of 75 Å and 60° for the rise and rotation for repeating units. The windowed segments were used to generate an initial reconstruction using `sxhelicon.py`²⁷. A cylinder of radius 28 pixels (approximated radius for helical unit) was used as the initial search model for the reconstruction. The reconstruction was further polished using `sxheliconlocal.py`. Generating a reconstruction without prior helical symmetrization led to a new estimate for the rise and rotation of the helical units of 74.7 Å and 56.3°, close to our initial estimates for these values. Crystal structures of the α2 and β2 subunits (PDB 4R1R and 1RIB, respectively) from the *E. coli* class Ia enzyme were docked into the EM density and all structure representations were generated using UCSF Chimera.

4.F References

- 1 Hofer, A., Crona, M., Logan, D. T. & Sjoberg, B. M. DNA building blocks: keeping control of manufacture. *Crit Rev Biochem Mol Biol* **47**, 50-63, doi:10.3109/10409238.2011.630372 (2012).
- 2 Brown, N. C., Canellakis, Z. N., Lundin, B., Reichard, P. & Thelander, L. Ribonucleoside diphosphate reductase. Purification of the two subunits, proteins B1 and B2. *Eur J Biochem* **9**, 561-573, doi:10.1111/j.1432-1033.1969.tb00646.x (1969).
- 3 Brignole, E. J., Ando, N., Zimanyi, C. M. & Drennan, C. L. The prototypic class Ia ribonucleotide reductase from *Escherichia coli*: still surprising after all these years. *Biochem Soc Trans* **40**, 523-530, doi:10.1042/BST20120081 (2012).
- 4 Uhlin, U. & Eklund, H. Structure of ribonucleotide reductase protein R1. *Nature* **370**, 533-539, doi:10.1038/370533a0 (1994).
- 5 Aravind, L., Wolf, Y. I. & Koonin, E. V. The ATP-cone: an evolutionarily mobile, ATP-binding regulatory domain. *J Mol Microbiol Biotechnol* **2**, 191-194 (2000).
- 6 Ando, N. *et al.* Structural interconversions modulate activity of *Escherichia coli* ribonucleotide reductase. *Proc Natl Acad Sci U S A* **108**, 21046-21051, doi:10.1073/pnas.1112715108 (2011).
- 7 Nordlund, P., Sjoberg, B. M. & Eklund, H. Three-dimensional structure of the free radical protein of ribonucleotide reductase. *Nature* **345**, 593-598, doi:10.1038/345593a0 (1990).
- 8 Brown, N. C. & Reichard, P. Ribonucleoside diphosphate reductase. Formation of active and inactive complexes of proteins B1 and B2. *J Mol Biol* **46**, 25-38 (1969).
- 9 Zimanyi, C. M. *et al.* Tangled up in knots: structures of inactivated forms of *E. coli* class Ia ribonucleotide reductase. *Structure* **20**, 1374-1383, doi:10.1016/j.str.2012.05.009 (2012).
- 10 Brignole, E. J. *et al.* 3.3-A resolution cryo-EM structure of human ribonucleotide reductase with substrate and allosteric regulators bound. *Elife* **7**, doi:10.7554/eLife.31502 (2018).
- 11 Thomas, W. C. *et al.* Convergent allostery in ribonucleotide reductase. *Nat Commun* **10**, 2653, doi:10.1038/s41467-019-10568-4 (2019).
- 12 Berglund, O., Karlstrom, O. & Reichard, P. A new ribonucleotide reductase system after infection with phage T4. *Proc Natl Acad Sci U S A* **62**, 829-835, doi:10.1073/pnas.62.3.829 (1969).
- 13 Berglund, O. in *Journal of Biological Chemistry* Vol. 247 7276-7281 (American Society for Biochemistry and Molecular Biology, 1972).
- 14 Berglund, O. in *Journal of Biological Chemistry* Vol. 247 7270-7275 (American Society for Biochemistry and Molecular Biology, 1972).
- 15 Hanson, E. & Mathews, C. K. Allosteric effectors are required for subunit association in T4 phage ribonucleotide reductase. *J Biol Chem* **269**, 30999-31005 (1994).

- 16 Eriksson, M. *et al.* Binding of allosteric effectors to ribonucleotide reductase protein R1: reduction of active-site cysteines promotes substrate binding. *Structure* **5**, 1077-1092 (1997).
- 17 Nordlund, P. & Eklund, H. Structure and function of the Escherichia coli ribonucleotide reductase protein R2. *J Mol Biol* **232**, 123-164, doi:10.1006/jmbi.1993.1374 (1993).
- 18 Buckstein, M. H., He, J. & Rubin, H. Characterization of nucleotide pools as a function of physiological state in Escherichia coli. *Journal of Bacteriology* **190**, 718-726, doi:10.1128/Jb.01020-07 (2008).
- 19 Climent, I., Sjöberg, B. M. & Huang, C. Y. Carboxyl-terminal peptides as probes for Escherichia coli ribonucleotide reductase subunit interaction: kinetic analysis of inhibition studies. *Biochemistry* **30**, 5164-5171, doi:10.1021/bi00235a008 (1991).
- 20 Zimanyi, C. M., Chen, P. Y., Kang, G., Funk, M. A. & Drennan, C. L. Molecular basis for allosteric specificity regulation in class Ia ribonucleotide reductase from Escherichia coli. *Elife* **5**, e07141, doi:10.7554/eLife.07141 (2016).
- 21 Zimanyi, C. M. *Structural Studies of Allosteric Regulation in the Class Ia Ribonucleotide Reductase from Escherichia coli* Ph.D. thesis, Massachusetts Institute of Technology, (2013).
- 22 Fairman, J. W. *et al.* Structural basis for allosteric regulation of human ribonucleotide reductase by nucleotide-induced oligomerization. *Nat Struct Mol Biol* **18**, 316-322, doi:10.1038/nsmb.2007 (2011).
- 23 Brown, N. C., Eliasson, R., Reichard, P. & Thelander, L. Spectrum and iron content of protein B2 from ribonucleoside diphosphate reductase. *Eur J Biochem* **9**, 512-518, doi:10.1111/j.1432-1033.1969.tb00639.x (1969).
- 24 Salowe, S. P., Ator, M. A. & Stubbe, J. Products of the inactivation of ribonucleoside diphosphate reductase from Escherichia coli with 2'-azido-2'-deoxyuridine 5'-diphosphate. *Biochemistry* **26**, 3408-3416, doi:10.1021/bi00386a024 (1987).
- 25 Salowe, S. P. & Stubbe, J. Cloning, overproduction, and purification of the B2 subunit of ribonucleoside-diphosphate reductase. *J Bacteriol* **165**, 363-366, doi:10.1128/jb.165.2.363-366.1986 (1986).
- 26 Mastronarde, D. N. Automated electron microscope tomography using robust prediction of specimen movements. *J Struct Biol* **152**, 36-51, doi:10.1016/j.jsb.2005.07.007 (2005).
- 27 Behrmann, E. *et al.* Real-space processing of helical filaments in SPARX. *J Struct Biol* **177**, 302-313, doi:10.1016/j.jsb.2011.12.020 (2012).
- 28 Hohn, M. *et al.* SPARX, a new environment for Cryo-EM image processing. *J Struct Biol* **157**, 47-55, doi:10.1016/j.jsb.2006.07.003 (2007).

4.G Figures

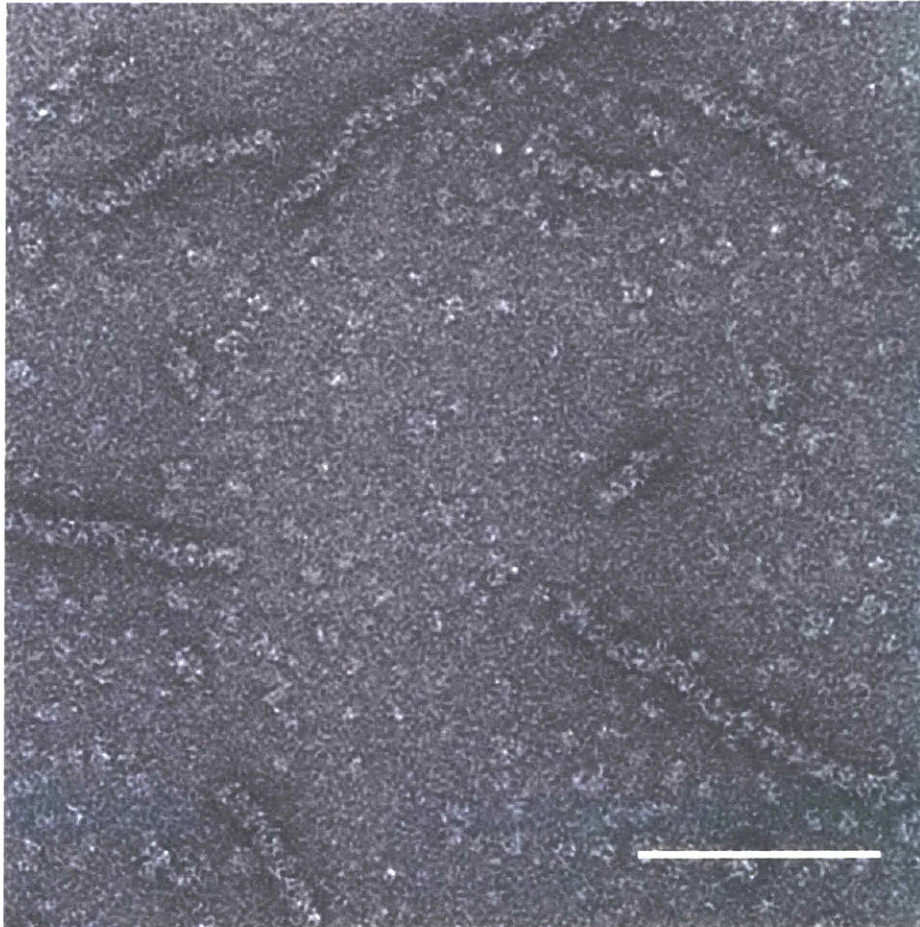


Figure 4.1: T4 class Ia RNR forms filaments under traditionally inhibitory conditions. In the presence of $\alpha 2$, $\beta 2$, 1 mM CDP, 1 mM dATP, and 5 mM $MgCl_2$, the T4 enzyme forms filaments. We also observe significant amount of “free” particles, but further analysis is required to determine their composition. $\alpha 2$ and $\beta 2$ were each present at 60 nM. Scale bar indicates 100 nm.

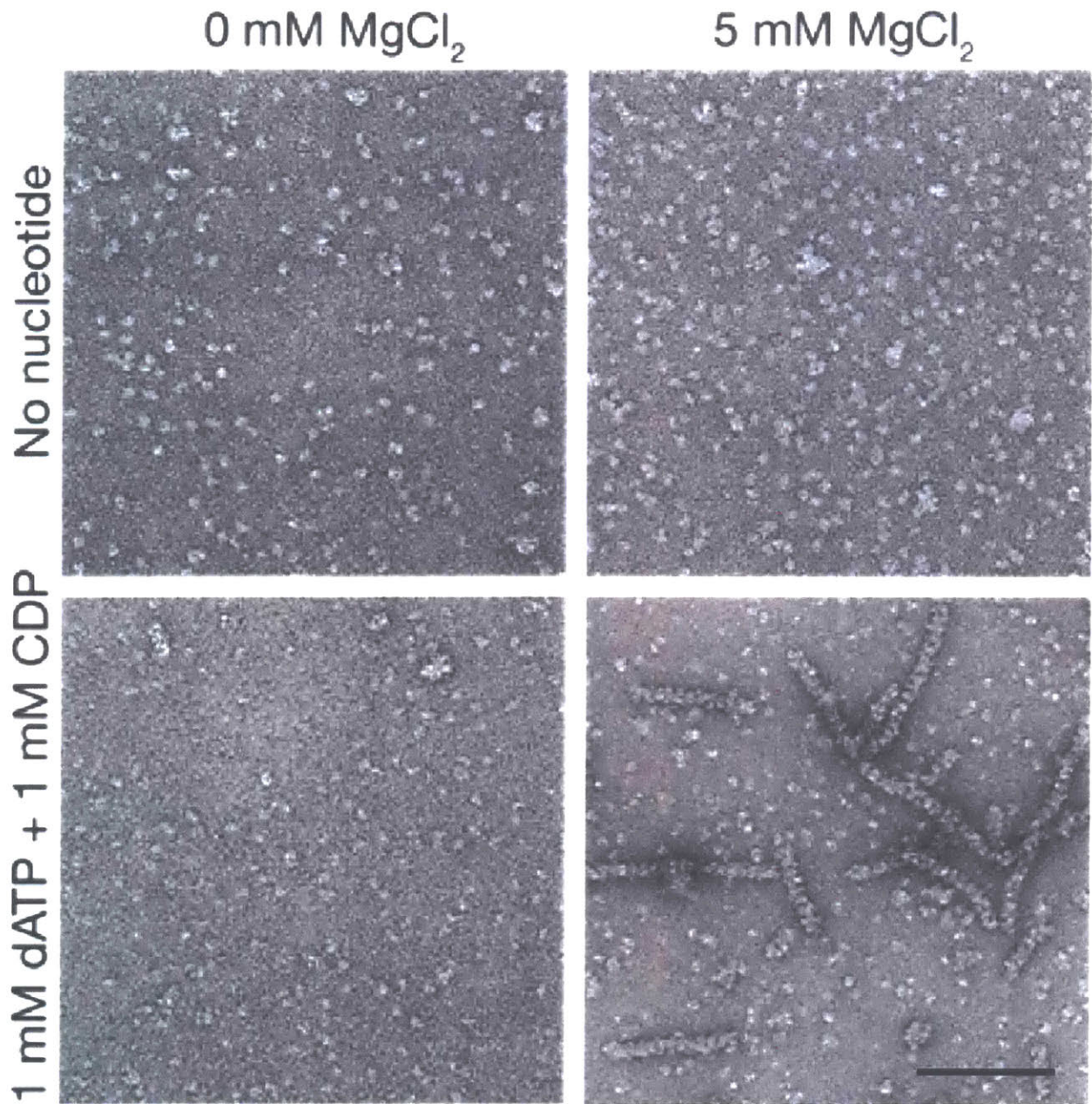


Figure 4.2: Filaments do not form in the absence of nucleotide or magnesium. $\alpha 2$ and $\beta 2$ were each present at 60 nM. Scale bar represents 100 nm.

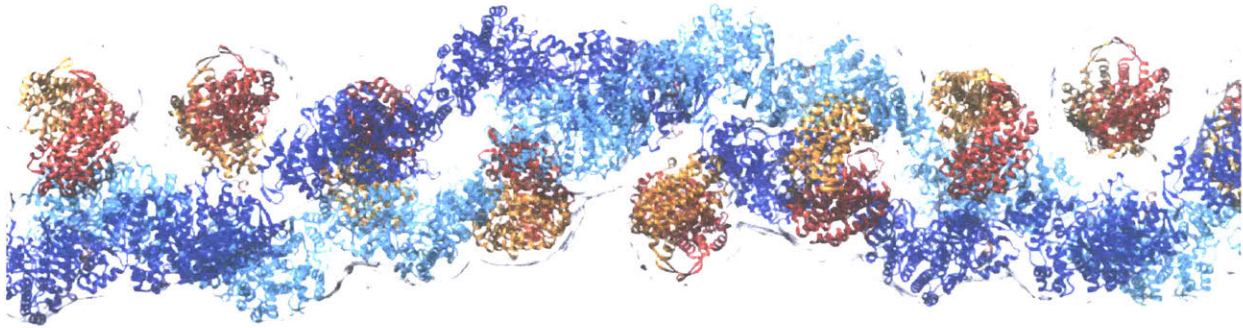


Figure 4.3: Filaments formed by T4 class Ia RNR are composed of both $\alpha 2$ and $\beta 2$. 3D reconstruction of the negative-stain EM data reveals that the filaments are composed of both subunits. The rise and pitch of successive helical units are $\sim 75 \text{ \AA}$ and $\sim 56^\circ$, respectively. $\alpha 2$ is shown in blue/cyan and $\beta 2$ in red/orange. PDB IDs for $\alpha 2$ and $\beta 2$ are 4R1R and 1RIB, respectively.

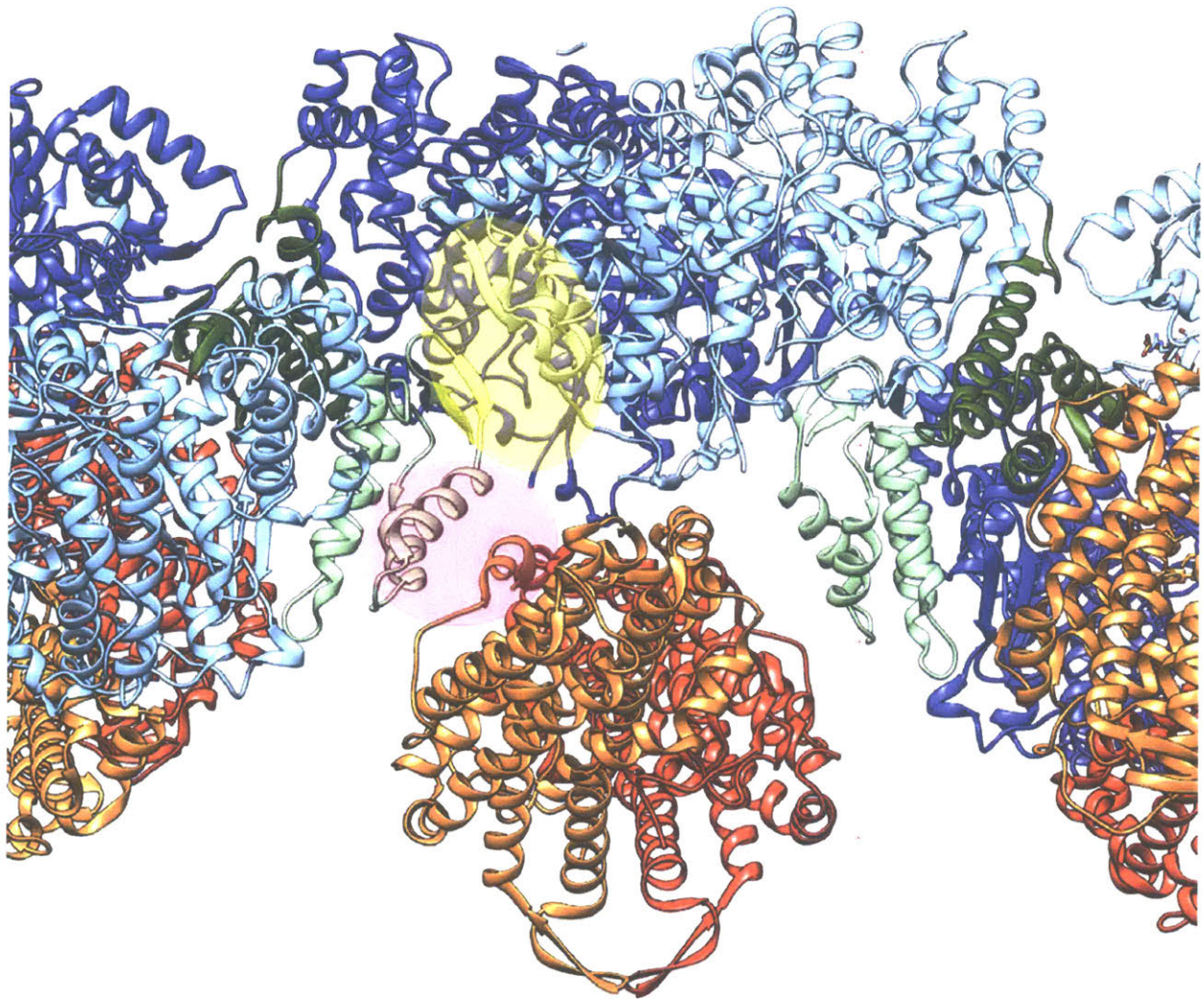


Figure 4.4: Potential interactions between helical units contributing to filament formation. Highlighted in transparent yellow: The β -hairpin of the cone-domain (shown in light-green, residues 1-16) of the previous helical unit are in proximity to a β -strand (residues 390-395) in $\alpha 2$ of the helical unit shown in the center of view. Highlighted in transparent pink: An α -helix formed by residues 332-340 of $\beta 2$ is in proximity to α -helices 1 and 2 (residues 20-48) of the preceding helical unit's cone domain. Colors are as in Figure 4.3.

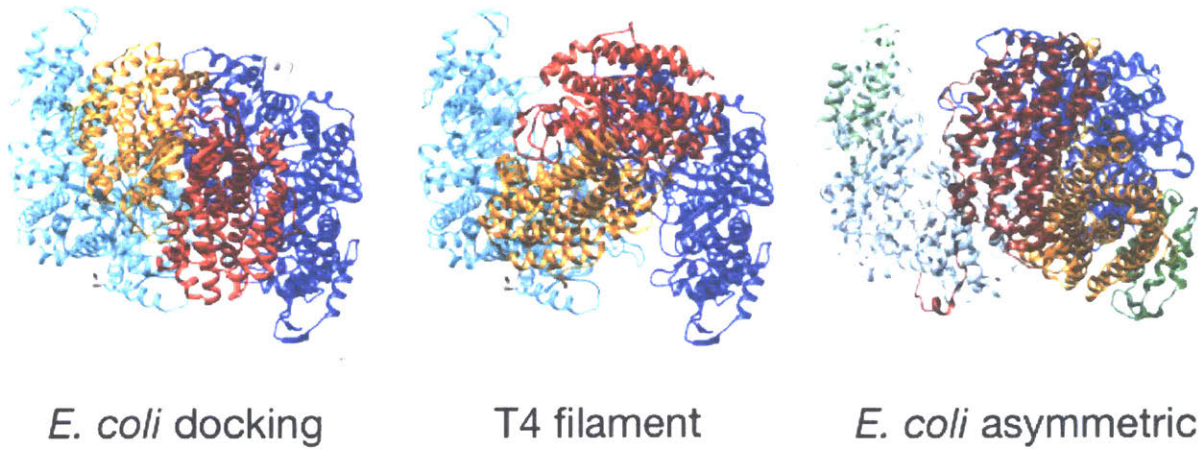


Figure 4.5: Orientation between $\alpha 2$ and $\beta 2$ in filaments is rotated from that of docking model. The relative orientation of $\beta 2$ to $\alpha 2$ in the docking model is shown on the left. In contrast, the relative orientation of $\beta 2$ to $\alpha 2$ in the T4 filament (middle), is rotated approximately 90° relative to the docking model. The interaction found in the asymmetric $\alpha 2\beta 2$ complex is shown on the far right as reference. $\alpha 2$ is shown in blue/cyan and $\beta 2$ in orange/red.

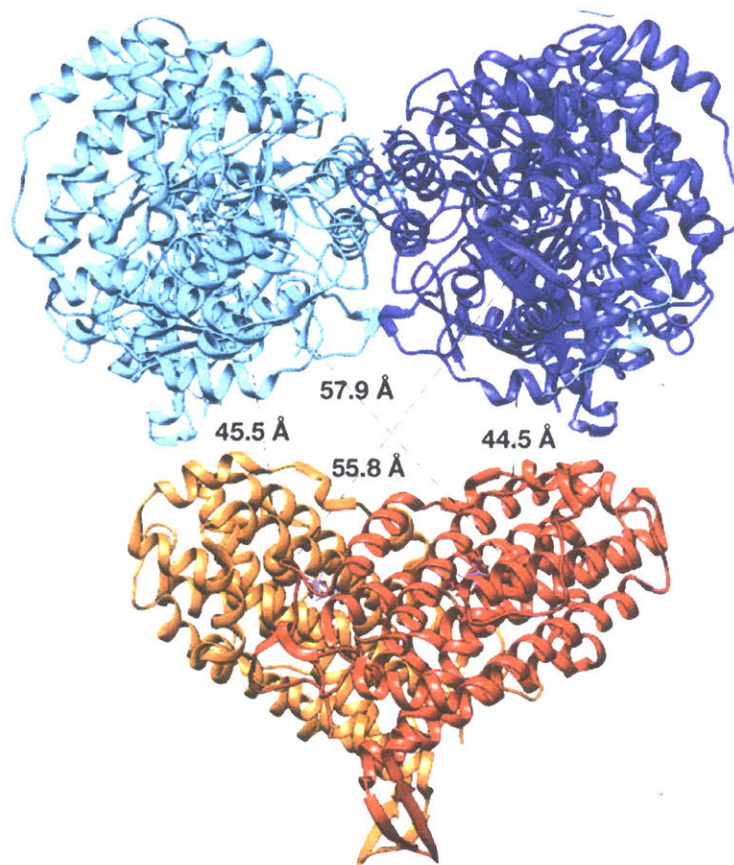
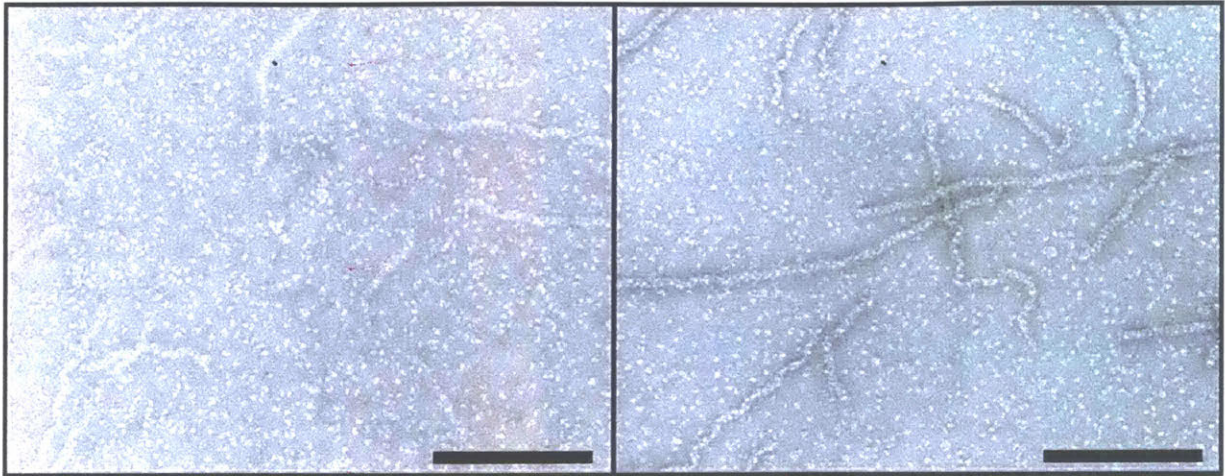
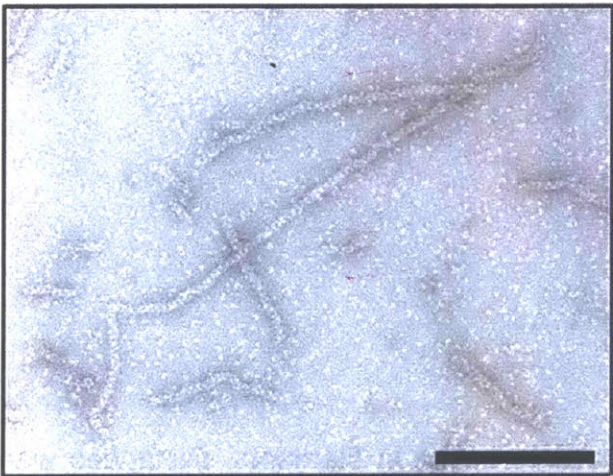


Figure 4.6: $\alpha 2$ and $\beta 2$ do not form compact interaction in filaments. Distances were measured between Y122 of each β monomer and Y730 of each α monomer. $\alpha 2$ shown in blue/cyan and $\beta 2$ in orange/red.



1 mM dATP
1 mM CDP

175 μ M dATP
1 mM CDP



3 mM ATP
1 mM CDP

Figure 4.7: Filaments form in the presence of dATP or ATP. Nucleotide concentrations are as shown. α 2 and β 2 are each present at 60 nM. Scale bars represent 100 nm. Differences in particle contrast can be attributed to thinner or thicker stain in the imaged field of view.

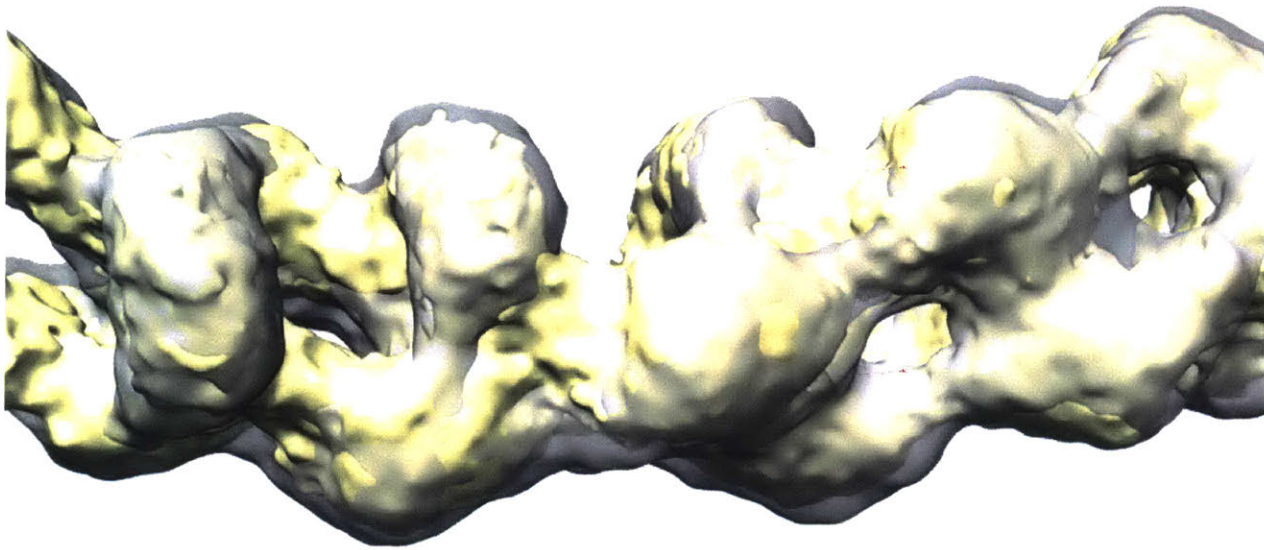


Figure 4.8: Filaments formed in presence of ATP align well with those formed in presence of dATP. A 3D reconstruction was generated from the filaments that were formed in the presence of 3 mM ATP, with the EM density shown in yellow. This density aligns well with the EM density previously generated from the filaments formed in the presence of dATP, shown in transparent grey.

Chapter 5

Closing thoughts and future directions

5.A: Closing thoughts and future directions

Nearly twenty-five years since the first crystal structures of α_2 and β_2 were solved and the “docking model” proposed^{1,2}, we have finally been able to obtain a high-resolution structure of the active $\alpha_2\beta_2$ complex of *E. coli* class Ia ribonucleotide reductase (RNR), long considered to be the structural “holy grail” in the field. There were key factors in our understanding of RNR, together with technological advancements that finally made this achievement possible.

Site-specifically incorporating unnatural amino acids (NH_2 -, NO_2 -, F_n -Ys) along the proton-coupled electron transfer pathway (Y122, Y356 in β and Y730, Y731 in α) uncoupled the radical transfer process from the conformational gating that makes studying chemical rates in class Ia RNR so challenging, allowed for visualization of pathway radical at various positions, and provided further evidence of half-sites reactivity in *E. coli* RNR³⁻⁸. In addition to the insight into the biochemical properties of RNR these constructs afforded, it was perhaps an unexpected phenomenon that arose as a result of the substitutions that generated excitement from a structural studies perspective. It was observed that trapping or stalling pathway radical was associated with an increase in $\alpha_2\beta_2$ complex lifetime⁹. However, the increased kinetic stability of the complex was still not suited for crystallographic studies as the complex would fall apart on the scale of minutes-hours versus the often days required for crystallization.

Rather, electron microscopy (EM) appeared to be the appropriate structural technique, as the protein sample could be fixed (either by negative-staining or rapid freezing) as early as a few seconds after initiating a given reaction¹⁰. However, it was not until the development of direct-electron detectors and more sophisticated processing software that allowed for the community to study such relatively small (~250 kDa for the $\alpha_2\beta_2$ complex), non-symmetric, and potentially heterogenous proteins¹¹.

Even with these technological developments, there was initial doubt as to whether we could structurally observe a “rigid” complex with the α_2 - β_2 interface fully ordered. When

we first solved the structure of WT- $\alpha 2\beta 2$ in the presence of N_3UDP to 8-Å resolution (discussed in Chapter 3), we were disheartened to observe no cryo-EM density at the $\alpha 2\text{-}\beta 2$ interface, neither in our initial reconstruction nor our follow-up analyses. We feared this indicated that save for the precise moment of radical transfer across the $\alpha 2\text{-}\beta 2$ interface, this region of the complex is structurally flexible to the point of not being able to resolve to high-resolution. This of course, turned out not to be true, and we have now been able to obtain two structures of the $\alpha 2\beta 2$ complex to 3.6-Å and 5-Å resolution, respectively, by cryo-EM that show a structurally rigid interface.

For the two $\alpha 2\beta 2$ structures discussed in this dissertation, the method of trapping the pathway radical was different in the two cases, yet both lead to complexes where the interface regions were structurally ordered. E52Q/F₃Y122- $\alpha 2\beta 2$ discussed in Chapter 2 trapped the radical at Y356 likely during back-electron transfer, and as such, we observed turnover in one active site¹². $N_3UDP\text{-}\alpha 2\beta 2$ discussed in Chapter 3 trapped the radical in the form of a unique $N\bullet$ species in the active site⁷. In both of the discussed $\alpha 2\beta 2$ structures, chemistry occurred in one active site and in the trapped complex, we observe $\beta 2$ interacting with the α monomer where a reaction had not appeared to have taken place. Obtaining a structure of the $\alpha 2\beta 2$ complex in which the radical has been trapped in the forward direction, in other words before any chemistry occurs in either active site, may provide additional insight into the conformational dynamics that occur prior to nucleotide reduction. For example, in both our $\alpha 2\beta 2$ structures, the C-terminus of only one β monomer is observed along the α monomer in which chemistry had not yet occurred. In a pre-turnover state, would we observe both C-termini of $\beta 2$ along $\alpha 2$? To this end, $NH_2Y\text{-}$ substituted $\alpha 2$ s or $\beta 2$ s may be worth another visit as a means of obtaining a structure of a complex trapped during forward radical transfer. These constructs have been structurally explored previously using negative-stain EM, that lead to a 32-Å resolution structure of the $\alpha 2\beta 2$ complex⁹. However, given the previously measured $t_{1/2}$ of the $NH_2Y\bullet$ being ~ 2.7 minutes at 25°C¹³, it may lead to a more heterogeneous sample population than the E52Q/F₃Y- $\alpha 2\beta 2$ discussed in Chapter 2. This difficulty could potentially be overcome by collecting a larger data set and

attempting to classify out existing heterogeneity. An alternative strategy could be to use F₃Y122, shown to generate Y356• at 20-30 s⁻¹ ⁶, with a phenylalanine (F) block at Y731 α or Y730 α to prevent radical transfer to the active site C439.

Additionally, much is still structurally unknown regarding the C-terminus of α 2, of note due to its role in re-reducing the active site disulfide that forms as a result of turnover¹⁴. In both discussed structures of α 2 β 2, we observe additional α C-terminal residues out to residue 742 (of 761) that seem to be forming previously unknown interactions with β 2. Yet we still lack information regarding the remaining residues, including the position of the redox active pair of cysteines (C754 and C759). In our structural discussions of N₃UDP- α 2 β 2, we posited that the extra cryo-EM density observed along the conedomain of one of the α monomers may correspond to the flexible C-terminus of α . Perhaps obtaining an α 2 β 2 structure with 18 residues at the α 2 C-terminus (residues 743-761) truncated will reveal whether the observed extra density was an artifact or a true structural feature.

Further, our structures unequivocally show that re-reduction of the active site cysteines by the α C-terminus cannot occur prior to dissociation of β from that specific active site. However, in the asymmetric complex, one active site is exposed and it is unclear whether re-reduction of the exposed active site disulfide can occur prior to complete dissociation of β 2 from α 2. It is also possible this scenario would not occur in the WT enzyme where two turnover occur rapidly¹⁵ (18 ± 4 s⁻¹ under pre-steady state vs 5-10 s⁻¹ observed under steady state). In any case, whether the exposed active site in the α 2 β 2 complex is accessible to re-reduction by the C-terminus can perhaps be tested by utilizing a construct of α 2 that has one of the C-terminal cysteines mutated to a serine to prevent complete disulfide exchange in hopes of trapping the tail in the active site. Obtaining structures of this α 2 variant with both WT- β 2 and E52Q/F₃Y- β 2, only the latter of which should kinetically trap an α 2 β 2 complex, may shed light on whether the presence of β 2 sterically occludes the α 2 C-terminus from re-reducing the open active site after turnover. This goal also depends on whether we could obtain a structure of

just α_2 (~170 kDa) to sufficient resolution to observe a peptide bound in the active site. The reaction between the C-terminal cysteine and the active site cysteines is also potentially reversible, which may further complicate matters.

Given how conserved the active site architecture, mechanism of reduction, and rules of specificity are across all RNRs, there is a remarkable diversity of quaternary structures that govern activity/inactivity¹⁶⁻²⁰. Moving forward, we will have the opportunity to structurally study a much broader range of RNRs, from transient complexes like $\alpha_2\beta_2$ to those that form oligomers not particularly amenable to crystallization like the fibril-forming T4 phage RNR discussed in Chapter 4. The strength of structural biology is being able to provide informative snapshots of enzymes in action. In conjunction with knowledge gained through crystallographic studies, EM broadens the types of structures we can go after, from free subunits to both inactive and active states, and this in turn can serve to deepen our understanding of RNR mechanism and regulation. It is truly an exciting time in structural biology.

5.B References

- 1 Nordlund, P., Sjöberg, B. M. & Eklund, H. Three-dimensional structure of the free radical protein of ribonucleotide reductase. *Nature* **345**, 593-598, doi:10.1038/345593a0 (1990).
- 2 Uhlin, U. & Eklund, H. Structure of ribonucleotide reductase protein R1. *Nature* **370**, 533-539, doi:10.1038/370533a0 (1994).
- 3 Yokoyama, K., Smith, A. A., Corzilius, B., Griffin, R. G. & Stubbe, J. Equilibration of tyrosyl radicals (Y356*, Y731*, Y730*) in the radical propagation pathway of the Escherichia coli class Ia ribonucleotide reductase. *J Am Chem Soc* **133**, 18420-18432, doi:10.1021/ja207455k (2011).
- 4 Yokoyama, K., Uhlin, U. & Stubbe, J. Site-specific incorporation of 3-nitrotyrosine as a probe of pKa perturbation of redox-active tyrosines in ribonucleotide reductase. *J Am Chem Soc* **132**, 8385-8397, doi:10.1021/ja101097p (2010).
- 5 Seyedsayamdost, M. R. & Stubbe, J. Site-specific replacement of Y356 with 3,4-dihydroxyphenylalanine in the beta2 subunit of E. coli ribonucleotide reductase. *J Am Chem Soc* **128**, 2522-2523, doi:10.1021/ja057776q (2006).
- 6 Ravichandran, K. R., Minnihan, E. C., Wei, Y., Nocera, D. G. & Stubbe, J. Reverse Electron Transfer Completes the Catalytic Cycle in a 2,3,5-Trifluorotyrosine-Substituted Ribonucleotide Reductase. *J Am Chem Soc* **137**, 14387-14395, doi:10.1021/jacs.5b09189 (2015).
- 7 Fritscher, J. *et al.* Structure of the nitrogen-centered radical formed during inactivation of E. coli ribonucleotide reductase by 2'-azido-2'-deoxyuridine-5'-diphosphate: trapping of the 3'-ketonucleotide. *J Am Chem Soc* **127**, 7729-7738, doi:10.1021/ja043111x (2005).
- 8 Salowe, S. *et al.* Alternative model for mechanism-based inhibition of Escherichia coli ribonucleotide reductase by 2'-azido-2'-deoxyuridine 5'-diphosphate. *Biochemistry* **32**, 12749-12760, doi:10.1021/bi00210a026 (1993).
- 9 Minnihan, E. C. *et al.* Generation of a stable, aminotyrosyl radical-induced alpha2beta2 complex of Escherichia coli class Ia ribonucleotide reductase. *Proc Natl Acad Sci U S A* **110**, 3835-3840, doi:10.1073/pnas.1220691110 (2013).
- 10 Thompson, R. F., Walker, M., Siebert, C. A., Muench, S. P. & Ranson, N. A. An introduction to sample preparation and imaging by cryo-electron microscopy for structural biology. *Methods* **100**, 3-15, doi:10.1016/j.ymeth.2016.02.017 (2016).
- 11 Bai, X. C., McMullan, G. & Scheres, S. H. How cryo-EM is revolutionizing structural biology. *Trends Biochem Sci* **40**, 49-57, doi:10.1016/j.tibs.2014.10.005 (2015).
- 12 Lin, Q. *et al.* Glutamate 52-beta at the alpha/beta subunit interface of Escherichia coli class Ia ribonucleotide reductase is essential for conformational gating of radical transfer. *J Biol Chem* **292**, 9229-9239, doi:10.1074/jbc.M117.783092 (2017).
- 13 Seyedsayamdost, M. *Investigations of the mechanism of radical propagation in E. coli ribonucleotide reductase by site-specific incorporation of unnatural amino acids.*, Massachusetts Institute of Technology, (2007).

- 14 Mao, S. S. *et al.* A model for the role of multiple cysteine residues involved in ribonucleotide reduction: amazing and still confusing. *Biochemistry* **31**, 9733-9743, doi:10.1021/bi00155a029 (1992).
- 15 Ge, J., Yu, G., Ator, M. A. & Stubbe, J. Pre-steady-state and steady-state kinetic analysis of E. coli class I ribonucleotide reductase. *Biochemistry* **42**, 10071-10083, doi:10.1021/bi034374r (2003).
- 16 Zimanyi, C. M. *et al.* Tangled up in knots: structures of inactivated forms of E. coli class Ia ribonucleotide reductase. *Structure* **20**, 1374-1383, doi:10.1016/j.str.2012.05.009 (2012).
- 17 Ando, N. *et al.* Structural interconversions modulate activity of Escherichia coli ribonucleotide reductase. *Proc Natl Acad Sci U S A* **108**, 21046-21051, doi:10.1073/pnas.1112715108 (2011).
- 18 Brignole, E. J. *et al.* 3.3-A resolution cryo-EM structure of human ribonucleotide reductase with substrate and allosteric regulators bound. *Elife* **7**, doi:10.7554/eLife.31502 (2018).
- 19 Fairman, J. W. *et al.* Structural basis for allosteric regulation of human ribonucleotide reductase by nucleotide-induced oligomerization. *Nat Struct Mol Biol* **18**, 316-322, doi:10.1038/nsmb.2007 (2011).
- 20 Thomas, W. C. *et al.* Convergent allostery in ribonucleotide reductase. *Nat Commun* **10**, 2653, doi:10.1038/s41467-019-10568-4 (2019).

Appendices

Appendix A: Strategies for optimizing cryo-EM samples

Broadly, when transitioning from negative-stain to cryo-EM, several variables may need to be optimized and are discussed below. A recent report summarized many of the issues when dealing with cryo-EM sample preparations¹. The current discussion focuses on sample preparation considerations within the scope of the current setup available at MIT.

Plungers

The two most common commercially available cryo-plungers currently available are the Gatan Cryoplunge 3 (Cp3) and Thermo Fisher Vitrobot Mk IV. In both instruments, blot-time, blot-pressure, and the type of blotting paper used can be readily controlled. The advantages of the Vitrobot include a temperature and humidity controlled blotting chamber and the ability to plunge 16 samples before having to replace the blotting paper vs 4 for the Cp3. Advantages of the Cp3 are that the temperature of the ethane cup is electronically controlled, and because fewer of the moving parts are mechanically controlled by the instrument, the plunging process can be faster. The Cp3 allows for single-sided blotting, whereas the Vitrobot does not. The Cp3 also has a smaller footprint but because a pressurized piston controls the plunging mechanism, the Cp3 requires connection to a nitrogen gas source. In our hands, the Vitrobot has lead to more consistent sample preparations.

Grid types

There are currently two widely available commercial grids for cryo-EM, C-flat and Quantifoil. C-flats historically had issues that lead to the carbon on grid-squares being more likely to crack, but the quality appears to be improving. Copper-mesh grids are the most widely used, but other metal frames such as those made of nickel and gold are available as additional optimization variables.

Two grid variables to consider are mesh size and hole size/separation. The mesh size is defined as the number of squares per inch, therefore a lower mesh size corresponds to larger squares and thus more holes per square. For single-particle samples, 200 and 300 mesh are commonly used. In terms of hole-size 1.2/1.3, 2/2, and 2/1 grids are common, with the first and second number corresponding to the hole diameter and hole separation, respectively, in μm . Current data collection strategies on the Titan Krios allow for imaging more than once per hole, for which the 2 μm hole diameters are ideal (UMASS Worcester suggests the 2/1 grids).

Optimizing for good ice thickness

Several variable factors can influence the ice thickness and quality of the cryo-grid. These include blot time, blot force, volume of sample applied, glow discharge settings, humidity, temperature, as well as the type of grid.

For initial screening, applying 3.0 μL sample and using a neutral (defined below) blot force with a blot time of 5 seconds should be used as a starting point. Sample volumes of 2.4-3.2 μL have been used successfully in the past. The blot time corresponds to the time the blotting arms spend in contact with the sample-applied grid.

The blot force of the Vitrobot needs to be calibrated before each use to account for subtle shifts in the blotting arms between sessions. Calibrations should be performed without filter paper on the blotting arms. There is a light-source within the blotting chamber of the Vitrobot, and when calibrating, a neutral blotting force corresponds to the blotting force at which no light starts to pass through the shadow of the two blotting arms coming together. On a well-maintained instrument, this neutral blotting force will correspond to a blot force setting between -1 and 1. Settings of 95% humidity (will usually register as 100%) and 10°C (+4-+60°C range) have yielded positive results.

The Cp3 uses pressurized pistons for the blotting arms (versus mechanical arms for the Vitrobot) so the blotting “force” is somewhat arbitrary. Instead, the initial positioning of

the blotting arms can be brought closer or farther from the grid being plunged. The effects of varying this distance have not been explored thoroughly. The temperature of the Cp3 is equilibrated to ambient temperature and the humidity is adjusted by the use of a damp sponge inside the blotting chamber.

The first screening session of a new sample will give an idea of the quality of the ice based on the initial parameters. When imaged, areas of thicker ice will appear darker than areas with thinner ice. Some particles behave better in thicker ice and some in thinner ice. If the ice seems too thin, a lower blot pressure and/or shorter blot time may be necessary, and vice versa. Salt content can also affect blotting, so if one's sample contains high-salt, a longer initial blot time/pressure may be necessary. The blot time and force are the easiest variables to adjust, so should try to be optimized first. The difference between increasing blot time and blot force relative to each other has not been thoroughly explored.

Glow discharging, the process of temporarily making the grids hydrophilic, can also have an effect on ice thickness. Typical parameters for glow discharging are -15 mA for 60 seconds. If the solution is not wicking properly onto the grid when applied, which could lead to uneven ice, a lower current or longer time may be necessary.

The grid variables can also affect ice thickness. Larger squares and holes may require shorter blot times to get comparable ice thickness to a grid with smaller squares and/or holes. Larger holes can also lead to ice thickness gradients within the hole, where the ice near the edge of the hole is thicker than in the middle. A longer glow discharge or at a lower current may yield more even ice distribution.

Almost always, there is a wide range of ice thickness across the entire grid (i.e. some squares have thick ice, some have thin ice, and others look good). This is often not an issue when it comes to data collection as you typically only image a small fraction of the squares per grid for a complete dataset.

Protein concentration

Typically, a good starting point for protein concentration is ~10-20x used for negative-stain (for negative-stain, concentrations of 17-20 ng/ μ L generally yield good particle distribution, with proteins that form higher-order oligomers requiring slightly higher concentrations). The goal is to maximize the number of particles per field of view while avoiding overcrowding that can lead to issues downstream during particle picking and extraction.

Troubleshooting

Unfortunately, there is no magic condition that leads to optimal sample quality for all proteins. If the issue appears to be complex dissociation or aggregation, it may be caused by the harsh environment at the air-water interface and adding surfactants may help². A recent report on a more robust procedure to generate graphene-oxide grids³ may be worth exploring as well in this regard. In the case of projects from our lab, varying salt concentrations (the addition of KCl and NaAcetate have yielded positive results previously towards alleviating aggregation for human and *E. coli* class Ia ribonucleotide reductase samples, respectively).

Additional notes and considerations

Ice and ethane contamination are two non-trivial issues when it comes to sample quality. Unfortunately, the plungers are currently not located in humidity-controlled environments, thus seasonal fluctuations in ambient humidity cannot be avoided. However, precautions can be taken to avoid other sources of contamination⁴. The ethane holder for the Vitrobot is not temperature-controlled. It is therefore important to make sure the ethane temperature is sufficiently below the vitrification temperature of water (-137°C) to avoid formation of crystalline ice. A good visual cue is to cool the surrounding of the cup with liquid nitrogen until a thin layer of solid ethane begins to form around the inside of the cup. The ethane may continue to freeze, which will

prevent plunging if it solidifies beyond a certain point, and will then need to be thawed back to the appropriate state. The temperature of the Cp3 ethane is typically electronically set to between -170°C and -175°C . Transferring the frozen grids from the ethane cup into the storage button stored under liquid nitrogen is also a potential source of contamination as the grid is temporarily brought above the liquid surface. Care should be taken to move quickly, stay close to the cold cup/liquid nitrogen, and to avoid breathing onto the sample.

Appendix A References

- 1 Drulyte, I. *et al.* Approaches to altering particle distributions in cryo-electron microscopy sample preparation. *Acta Crystallogr D Struct Biol* **74**, 560-571, doi:10.1107/S2059798318006496 (2018).
- 2 Glaeser, R. M. *et al.* Factors that Influence the Formation and Stability of Thin, Cryo-EM Specimens. *Biophys J* **110**, 749-755, doi:10.1016/j.bpj.2015.07.050 (2016).
- 3 Palovcak, E. *et al.* A simple and robust procedure for preparing graphene-oxide cryo-EM grids. *J Struct Biol* **204**, 80-84, doi:10.1016/j.jsb.2018.07.007 (2018).
- 4 Thompson, R. F., Walker, M., Siebert, C. A., Muench, S. P. & Ranson, N. A. An introduction to sample preparation and imaging by cryo-electron microscopy for structural biology. *Methods* **100**, 3-15, doi:10.1016/j.ymeth.2016.02.017 (2016).

Appendix B: Negative-stain EM on human class Ia RNR with N₃CDP

There is little structural information regarding the active state of human class Ia RNR. Julia Page, a former UROP in the Stubbe lab, performed preliminary negative-stain electron microscopy (EM) experiments with Dr. Ed Brignole, looking at the effect of varying concentrations of ATP and N₃CDP on the oligomeric state of human class Ia RNR in the presence of both subunits. The samples were prepared as follows.

A solution containing 2.5 μ M His-H1 (α 2 subunit), 7.5 μ M His-H2 (β 2 subunit), 1, 3, or 10 mM ATP, 5 mM DTT, 50 mM Hepes, pH 7.6, 15 mM MgCl₂, and 1 mM EDTA was incubated at 37°C for 1 min. This solution was then diluted 10-fold in assay buffer with or without N₃CDP and containing a variable concentration of ATP to yield final concentrations of 0.25 μ M His-H1, 0.75 μ M His-H2, 1, 3, or 10 mM ATP, 0 or 100 μ M N₃CDP, 5 mM DTT, 50 mM Hepes, pH 7.6, 15 mM MgCl₂, and 1 mM EDTA. These solutions were incubated at 37°C for 2 min before loading onto continuous carbon grids (5 μ L per grid) and staining with 2% uranyl acetate. Grids were imaged on the Tecnai Spirit at the Whitehead at 80 kV and 49,000x magnification.

Interestingly, in the presence of both subunits and N₃CDP, an increase in ATP concentration led to both the decrease in observed rings (presumed to be α 6 rings) and an increase in the occurrence of short filaments that appear to be predominantly 3-4 α 2 units in length (**Figure B.1**). Filament formation has previously been observed in human RNR, but just in the presence of the α 2 subunit¹.

To further investigate the composition of these short filaments, 176 micrographs were collected of the condition containing 10 mM ATP and 0.1 mM N₃CDP and the SPARX helical reconstruction software package² was used to generate a 3D reconstruction analogous to the method used to investigate the filaments of T4 class Ia RNR discussed previously. We were able to generate an initial reconstruction where we could nominally dock in both the α 2 and β 2 subunits³ (PDB: 3HNC, 2UW2) into the density of each helical unit (**Figure B.2**) in a relative orientation that resembles a tight complex.

Unfortunately, the density for neither subunit is well defined enough for us to determine how the two subunits are interacting (symmetric vs asymmetric etc). It is also difficult to say how relevant these filaments are. Although an increase in ATP concentration leads to the formation of additional filaments, 10 mM is well above the physiological concentration, and even at this high concentration of effector, we still observe a significant population of free α_2 particles (**Figure B.1**). Regardless, based on our current model, the filaments seem to represent repeating units of $\alpha_2\beta_2$ of human RNR, with the density suggesting relatively high occupancy of the β_2 subunit.

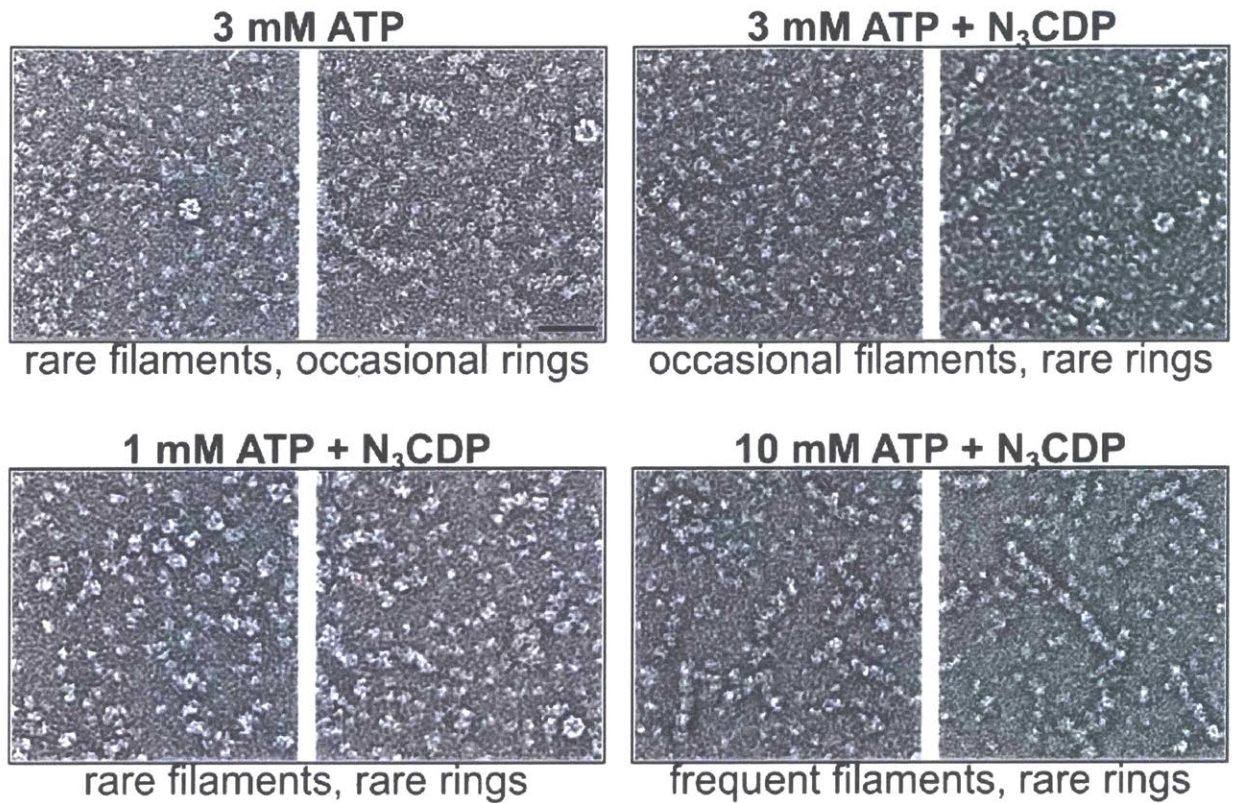


Figure B.1: Human class Ia RNR under varying concentrations of ATP (1-10 mM) and N₃CDP (0 or 100 μM). Increasing ATP concentration in the presence of N₃CDP shifts the oligomeric equilibrium towards short filaments. 250 nM α₂ and 750 nM β₂ are present in each sample. Two panels from each specimen are shown to illustrate the range of conformations seen in each condition. Scale bar represents 40 nm.

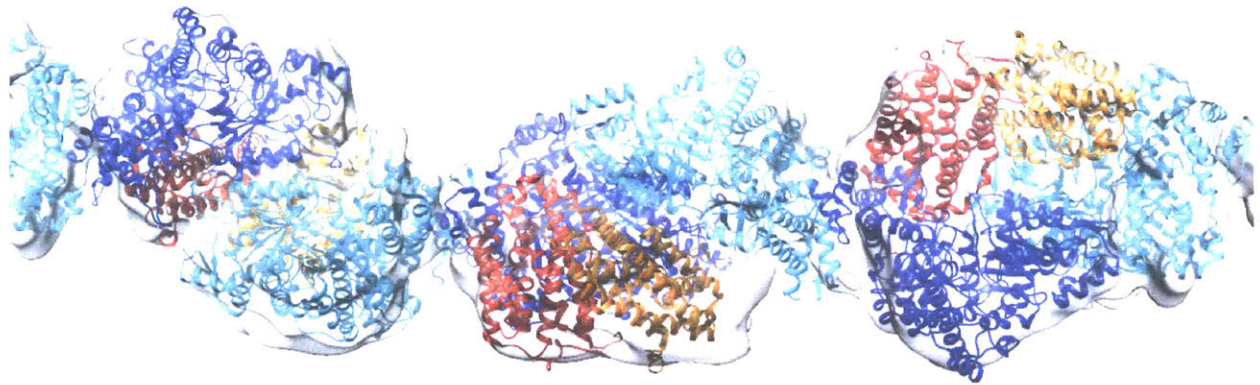


Figure B.2: 3D reconstruction of human class Ia RNR filaments generated in the presence of 10 mM ATP and 1 mM N_3 CDP. α_2 and β_2 were present at 250 nM and 750 nM, respectively. Crystal structures of human class Ia RNR subunits (PDB: 3HNC, 2UW2) are modeled into the 3D reconstruction. β_2 is clearly present in the density and there are roughly three $\alpha_2\beta_2$ units per helical turn. α_2 and β_2 are shown in blue/cyan and orange/red, respectively.

Appendix B References

- 1 Ando, N. *et al.* Allosteric Inhibition of Human Ribonucleotide Reductase by dATP Entails the Stabilization of a Hexamer. *Biochemistry* **55**, 373-381, doi:10.1021/acs.biochem.5b01207 (2016).
- 2 Behrmann, E. *et al.* Real-space processing of helical filaments in SPARX. *J Struct Biol* **177**, 302-313, doi:10.1016/j.jsb.2011.12.020 (2012).
- 3 Fairman, J. W. *et al.* Structural basis for allosteric regulation of human ribonucleotide reductase by nucleotide-induced oligomerization. *Nat Struct Mol Biol* **18**, 316-322, doi:10.1038/nsmb.2007 (2011).

Appendix C: Activity assays of *E. coli* class Ia RNR

The results from the following discussion were published as part of Zimanyi, C.M., Chen, P.Y.T., Kang, G., Funk, M., Drennan, C.L. Molecular basis for allosteric specificity regulation in class Ia ribonucleotide reductase from *Escherichia coli*. eLife 2016;5:e07141.

Structural evidence had suggested that Q294 and R298, both located on loop 2 in $\alpha 2$ play key roles in stabilizing substrate binding in the active site. With dATP bound in the specificity site, Q294 was proposed to form a hydrogen bond with CDP and UDP, but does not affect ADP and GDP binding in the presence of dGTP and TTP, respectively. R298 was proposed to form a conserved interaction of the β -phosphate of all four substrates¹.

In support of these structural claims, activity assays in the presence of each substrate/effector pair (dATP+CDP/UDP, dGTP+ADP, TTP+GDP) were performed for wildtype(WT)- $\alpha 2$, Q294A- $\alpha 2$, and R298- $\alpha 2$. Assays were performed using the continuous, coupled, spectrophotometric assay monitoring consumption of NADPH via the thioredoxin (TR)/thioredoxin reductase (TRR) system² and were carried out on a Cary Bio300 spectrometer (Agilent). Each condition was performed in triplicate. Data analysis was performed using the Cary WinUV Kinetics program (Agilent) and Microsoft Excel. Substrate and effector concentrations were as follows: 1 mM CDP and 3 mM ATP (control for presence of activity), 1 mM CDP and 175 μ M dATP (control for inactivation by dATP), 1 mM ADP and 120 μ M dGTP, 1 mM GDP and 250 μ M TTP, and 1 mM CDP/UDP and 1 μ M dATP. Substrate, effector, TR (30 μ M), TRR (0.5 μ M), NADPH (200 μ M) were premixed, and the reaction was initiated by the addition of $\alpha 2$ (0.1 μ M) and $\beta 2$ (1 μ M) to a total reaction volume of 120 μ L. The decrease in NADPH absorbance at 340 nm was monitored over 1 minute and basal level of NADPH oxidation was monitored over 30 sec prior to reaction initiation.

Consistent with the structural model, the Q294A mutant negatively affected CDP and UDP reduction in the presence of low concentrations of dATP (presumably only bound in the specificity site, and not the activity site), whereas it had minimal or no effect on GDP and ADP reduction in the presence of their respective effectors. In contrast, the R298A mutant nearly abolished all activity for all four substrate/effector pairs. Notably, the lack of ATP in our reaction conditions with WT- α 2, UDP/CDP, and low dATP (1 μ M) had no negative impact on overall activity relative to our positive control that included CDP and 3 mM ATP.

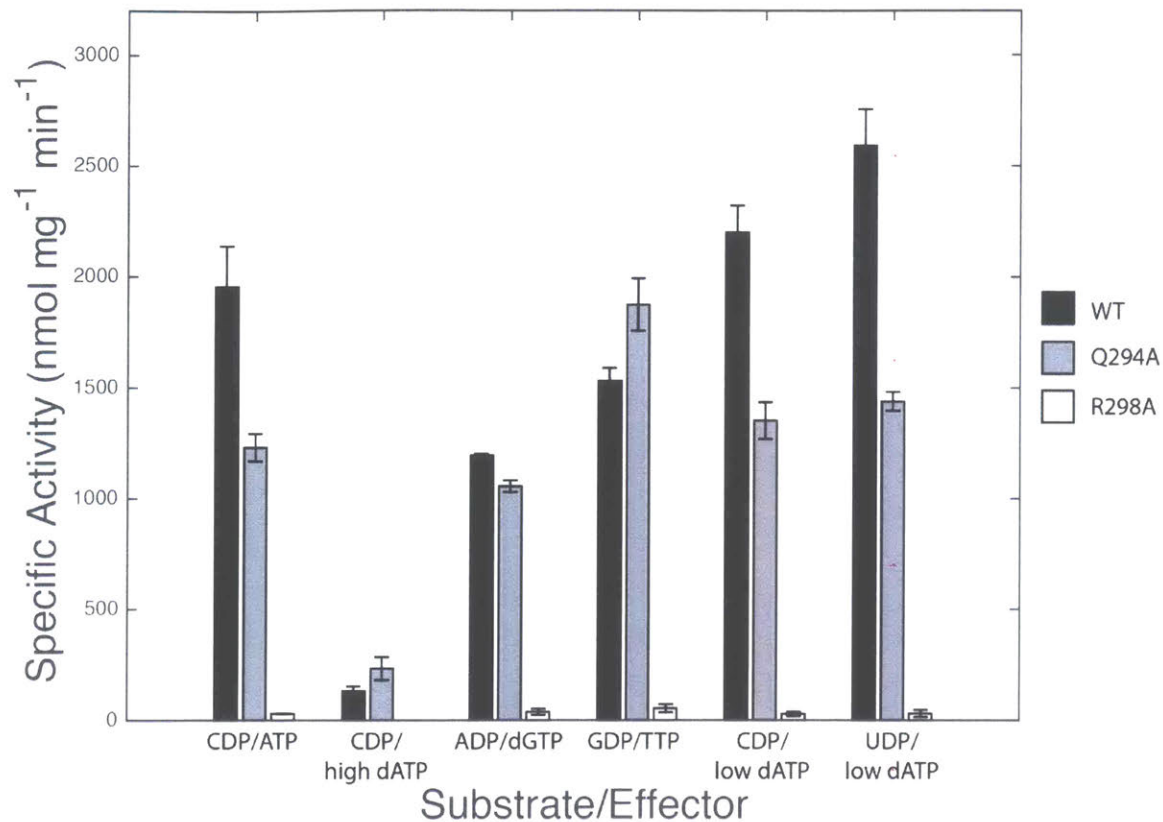


Figure C.1: Specific activity of $\alpha 2$ constructs in the presence of different substrate/effector pairs. Substrate concentrations were 1 mM and effector concentrations were as followed: 3 mM ATP, 175 μ M high dATP, 120 μ M dGTP, 250 μ M TTP, 1 μ M low dATP. CDP/ATP and CDP/high dATP were performed as positive and negative controls, respectively. Each assay condition was performed in triplicate.

Appendix C References

- 1 Zimanyi, C. M., Chen, P. Y., Kang, G., Funk, M. A. & Drennan, C. L. Molecular basis for allosteric specificity regulation in class Ia ribonucleotide reductase from *Escherichia coli*. *Elife* **5**, e07141, doi:10.7554/eLife.07141 (2016).
- 2 Ge, J., Yu, G., Ator, M. A. & Stubbe, J. Pre-steady-state and steady-state kinetic analysis of *E. coli* class I ribonucleotide reductase. *Biochemistry* **42**, 10071-10083, doi:10.1021/bi034374r (2003).

Gyunghoon (Kenny) Kang

Massachusetts Institute of Technology
Department of Chemistry
77 Massachusetts Avenue, 68-688
Cambridge, MA 02139

E-mail: gkang@mit.edu

EDUCATION

Ph.D. Candidate, Biological Chemistry, 2013 – present

- Massachusetts Institute of Technology, Cambridge, MA
- GPA 4.6

B.A., Chemistry and Chemical Biology, 2008 – 2012

- Cornell University, Ithaca, NY
- *Magna cum Laude*
- GPA 3.9

RESEARCH EXPERIENCE

Graduate Research, August 2013 – present

Massachusetts Institute of Technology, Cambridge, MA

Advisor: Prof. Catherine L. Drennan

- Using cryo-electron microscopy to study the active complex of *E. coli* ribonucleotide reductase (RNR)
- Using cryo-electron microscopy to study the helical oligomerization of T4 bacteriophage RNR
- Using negative stain electron microscopy to probe oligomeric states of RNRs from various species
- Employing photo-crosslinkers on protein residues to probe subunit-subunit interactions
- Generating protein truncation constructs to structurally probe mechanisms of enzymatic turnover using X-ray crystallography

Undergraduate Research, June 2010 – June 2012

Cornell University, Ithaca, NY

Advisor: Prof. Hening Lin

- Investigated potential multifunctional activity of a reported protein acetyltransferase from *Sulfolobus solfataricus* via Western Blot and LC-MS assays using synthetic peptide substrate analogs

MENTORING AND TEACHING EXPERIENCE

Kaufman Teaching Certificate Program, May 2017 – June 2017

Teaching+Learning Lab, Massachusetts Institute of Technology, Cambridge, MA

- Completed 8-week intensive course on developing teaching skills in designing a course and syllabus, planning a class session, interactive teaching and active learning, constructing effective problem sets and exams, and teaching inclusively

Research Mentor, September 2016 – February 2017

Massachusetts Institute of Technology, Cambridge, MA

- Guided visiting student Katharina Grunau on studies of probing RNR subunit interactions using crystallography and electron microscopy

Research Mentor, June 2015 – August 2015

Massachusetts Institute of Technology, Cambridge, MA

- Guided undergraduate student Sheena Vasquez on crystallographic studies of RNR from T4 bacteriophage

Graduate Teaching Assistant, August 2013 – May 2014

Department of Chemistry, Massachusetts Institute of Technology, Cambridge, MA

- General Chemistry: instructed a biweekly recitation section and held weekly office hours
- Chemistry lab: instructed biweekly lab classes and prepared necessary reagents and equipment

Teaching Assistant, August 2012 – June 2013

Pre-medical Program, Weill Cornell Medicine-Qatar, Doha, Qatar

- Full-time teaching assistant for organic chemistry lecture and lab

SELECTED FELLOWSHIPS AND AWARDS

- David H. Koch Graduate Fellowship award, 2017
- MIT Spot Award, given for “exceptional contributions” to the Chemistry Dept., 2016
- Phi Beta Kappa, Cornell University, Ithaca NY, 2012

PUBLICATIONS

Kang, G., Brignole, E., Taguchi, A., Stubbe, J., Drennan, C.L. “Cryo-EM structure of active class Ia ribonucleotide reductase from *Escherichia coli*.” *In preparation*.

Lin, Q., Parker, M. J., Taguchi, A. T., Ravichandran, K., Kim, A., **Kang, G.**, ... Stubbe, J. Glutamate 52- β at the α/β subunit interface of *Escherichia coli* class Ia ribonucleotide reductase is essential for conformational gating of radical transfer. *Journal of Biological Chemistry* **292**, 9229–9239 (2017).

Bridwell-Rabb, J., **Kang, G.**, J., Zhong, A., Liu, H.-w., Drennan, C.L. An HD-domain phosphohydrolase active site tailored for Oxetanocin-A biosynthesis, *Proc. Natl. Acad. Sci.* **113**, 13750-13755 (2016).

Zimanyi, C. M., Chen, P. Y. T., **Kang, G.**, Funk, M. A., & Drennan, C. L. "Molecular basis for allosteric specificity regulation in class Ia ribonucleotide reductase from *Escherichia coli*." *eLife* **5**: e07141 (2016).

Jost, M., Fernández-Zapata, J., Polanco, M.C., Ortiz-Guerrero, J.M., Chen, P.Y.T., **Kang, G.**, Padmanabhan, S., Elías-Arnanz, M. and Drennan, C.L. "Structural basis for gene regulation by a B12-dependent photoreceptor." *Nature* **526.7574**: 536-541 (2015).

PRESENTATIONS

“Using electron microscopy to probe the active state of ribonucleotide reductase”, Poster
Thermo Fisher Cryo-EM Symposium, Cambridge MA, April 2019

“Chasing the active state of ribonucleotide reductase”, Talk
Greater Boston Crystal Group, MIT, Cambridge MA, March 2019

“Visualizing the Active State of class Ia Ribonucleotide Reductase using cryo-EM”, Talk
RNR Symposium, MIT, Cambridge MA, November 2018

“Probing the Oligomeric States of Ribonucleotide Reductase using Electron Microscopy”, Poster
Center for Environmental Health Sciences, MIT, Cambridge MA, January 2017

“Chasing the Active State of class Ia Ribonucleotide Reductase”, Talk
Protein Structure Function Supergroup, MIT, Cambridge MA, December 2016

“Probing the Oligomeric States of Ribonucleotide Reductase using Electron Microscopy”, Poster
SBGrid/NE-CAT Phenix Workshop, Harvard Medical School, Boston MA, November 2016

COMMUNITY INVOLVEMENT AND PROFESSIONAL DEVELOPMENT

Chemistry Graduate Student Committee, September 2014 – present (President 2016-2017)

- In coordination with other student group leaders, designed and implemented two department-wide “quality of life” surveys
- Results from the survey were used to draft a list of recommendations that were presented to faculty, as well as the Chemistry Department Visiting Committee
- Participate in meetings with Dean of Science and Chemistry Department Chair to discuss improving department culture
- Provide mentorship and advice to incoming chemistry graduate students

Executive Board, MIT Science Policy Initiative, June 2016 – present

- Assisted in organizing S&TP Bootcamp course taught by former MIT Washington D.C. Office director Bill Bonvillian
- Advocate for science funding and education on Capitol Hill
- Assisted in acquiring funding for organization annual events
- Organize events to facilitate connections between groups in the Boston-area that are interested and engaged in science policy

Member, American Association for the Advancement of Science, 2016-present

Member, American Chemical Society, 2015-present

LABORATORY SKILLS AND TECHNIQUES

Structural biology:

- Preparing and optimizing negative stain electron microscopy (EM) grid samples for preliminary screening and low-resolution reconstruction generation
- Preparing and optimizing cryo-EM grid samples using Gatan Cp3 and Thermo Fisher Vitrobot cryo-plungers
- Screening and data collection for EM samples on Tecnai Spirit, F20, and F30

microscopes

- Generating and refining EM 3D reconstructions of single particle and helical proteins using the software packages RELION, SPHIRE, Phenix
- Structural analysis and figure generation using visualization software Chimera, PyMol, Coot
- Preparing, screening, and optimizing protein crystallization conditions

Molecular and Cell Biology:

- Cloning, site-directed mutagenesis
- Protein expression and purification

Organic Chemistry:

- Solid-phase peptide synthesis
 - High-performance liquid chromatography
-